Universidad Pública de Navarra
Nafarroako Unibertsitate Publikoa

ESCUELA TÉCNICA SUPERIOR DE INGENIERÍA AGRONÓMICA Y BIOCIENCIAS

NEKAZARITZAKO INGENIARITZAKO ETA BIOZIENTZIETAKO GOI MAILAKO ESKOLA TEKNIKOA

PS- DINSAR PROCESSING OF SENTINEL-1 IN THE HAMBACH MINE, GERMANY, AND ITS APPLICABILITY IN CIVIL INFRASTRUCTURE MONITORING.

presentado por

STEFKA MILENOVA VASILEVA

DIRECTORES:

JESÚS ÁLVAREZ MOZOS

IDURRE BARINAGARREMENTERIA ARRESE (Tracasa Global)

MASTER UNIVERSITARIO EN SISTEMAS DE INFORMACIÓN GEOGRÁFICA Y TELEDETECCIÓN
UNIBERTSITATE MASTERRA INFORMAZIO GEOGRAFIKOKO SISTEMETAN ETA TELEDETEKZIOAN

MUSIGT

Septiembre, 2023 / *2023, Iraila*

ACKNOWLEDGEMENTS

I would like to thank my supervisors, Jesús Álvarez and Idurre Barinagarrementeria, for their patience, good advice, support, and time spent guiding me and helping me during the whole process of my Master's thesis. Last but not least, I would like to thank all my friends and family who believed in me and supported me throughout this journey of learning, and to all my MUSIGT colleagues with whom I have exchanged valuable knowledge during these two years.

ABSTRACT

Civil infrastructure maintenance is paramount in rapidly developing countries like Germany, given its key role in societal well-being and economic growth. This study utilizes the Persistent Scatterers Differential Interferometric Synthetic Aperture Radar (PS-DInSAR) technique, applied to Sentinel-1 satellite imagery covering the period from January 2021 to December 2022, to implement a civil infrastructure monitoring approach. The study focuses on one of Germany's most challenging regions—The Rhenish coalfield area, and more specifically, the Hambach Mine, which stands as Europe's largest lignite open-pit mine. The Hambach Mine serves as a complex case study, highlighting the intricate interaction between rapid industrialization and environmental challenges. Through the analysis of vertical displacement of PS points and the implementation of various indicators, this research aims to gain a deeper understanding of the mechanisms of land subsidence localized in the hotspot around the mine and to enhance the monitoring of civil infrastructure within this area, with direct applications in the planning and development of civil infrastructure.

Keywords: Interferometry, PS-DinSAR, Sentinel-1, indicators, land subsidence, civil infrastructure.

RESUMEN

El mantenimiento de la infraestructura civil es primordial en países en rápido desarrollo como Alemania, dado su papel clave en el bienestar social y el crecimiento económico. Este estudio utiliza la técnica de radar de apertura sintética interferométrica diferencial de dispersión persistente (PS-DInSAR), aplicada a imágenes del satélite Sentinel-1 que cubren el período comprendido entre enero de 2021 y diciembre de 2022, para implementar un enfoque de monitoreo de infraestructura civil. El estudio se centra en una de las regiones más desafiantes de Alemania: la zona minera de Renania y, más específicamente, la mina Hambach, que es la mina a cielo abierto de lignito más grande de Europa. La mina Hambach sirve como un estudio de caso complejo, que destaca la intrincada interacción entre la rápida industrialización y los desafíos ambientales. A través del análisis del desplazamiento vertical de los puntos PS y la implementación de varios indicadores, esta investigación tiene como objetivo obtener una comprensión más profunda de los mecanismos de hundimiento del terreno localizados en el punto crítico alrededor de la mina y mejorar el monitoreo de la infraestructura civil dentro de esta área, con Aplicaciones directas en la planificación y desarrollo de infraestructuras civiles.

Palabras claves: Interferometría, PS-DInSAR, Sentinel-1, indicadores, subsidencia del terreno, infraestructura civil.

TABLE OF CONTENTS

LIST OF TABLES

LIST OF FIGURES

LIST OF ABBREVIATIONS:

ADI - Amplitude Dispersion Index
AcI – Acceleration Indicator
ASF – Alaska Satellite Facility
AI -Artificial Intelligence
AOI – Area of Interest
APS – Atmospheric Phase Removal
CRS – Coordinate Reference System
CLMS – Copernicus Land Monitoring Service
DEM - Digital Elevation Model
DinSAR – Differential Interferometry Synthetic Aperture Radar
DS- Distributed Scatterers
DSM – Digital Surface Model
DTM – Digital Terrain Model
EGMS – European Ground Motion Service
ESA – European Space Agency
EW - Extra Wide swath
GMG - Ground Motion Germany
GNSS – Global Navigation Satellite System
IW – Interferometric Wide swath
LoS – Line of Sight
M1 – Monitoring 1
MP – Measurement Point
NGL – Nevada Geodetic Laboratory
OSM – Open Street Map
PSC – Permanent Scatterer Candidate
PS – Persistent Scatterers
SAR – Synthetic Aperture Radar
SBAS – Small Baseline Subset
SB – Spatial Baseline
SM – Stripmap
SO – Specific Objectives
TB – Temporal Baseline
TC – Temporal Coherence
TI – Trend change Indicator
TOPSAR – Terrain Observation with Progressive Scans
WGS 84 - World Geodetic System 1984
WV - wave

1. Introduction

1.1. Background

Anthropogenic actions, especially mining operations, have a strong impact on the Earth's landscape, leading to severe geohazard events, such as land subsidence, landslides, and slope instability. Steep and exceptionally elevated slopes are frequent scenery in open-pit mining sites, making them vulnerable to slope failures. Such failures not only present significant risks to workers' lives but also can lead to considerable economic consequences (Tang et al., 2020; Tzampoglou & Loupasakis, 2023).

Even after a mine ceases operation, these issues can persist due to erosion and compaction processes, particularly within flat-tailed dump areas.
Monitoring and preventing these phenomena can be challenging. Traditional surveying techniques are commonly used for monitoring deformations in mining areas, offering high accuracy and direct observations. However, they have limitations in hazardous zones and cannot be deployed in extensive areas, since they are time-consuming and expensive. The dynamic nature of open-pit mines further complicates precise measurement within or near the pit and does not provide detailed time series data on vertical displacement (Herrera et al., 2010).

In contrast, space geodetic techniques are particularly interesting for measuring in detail the evolution and the ground displacements within mining zones. Interferometric Synthetic Aperture Radar (InSAR) with persistent scatterer analysis has emerged as a cost-effective solution for continuous and precise monitoring of ground displacements, experiencing significant advancements in recent years (Gojković et al., 2023).

The present study is centred in the Rhenish coalfield area, particularly in Germany's largest open-pit mine – Hambach, located in the North Westphalia region. Resource extraction within the Rhenish lignite region has a profound and enduring impact on the surrounding landscape. Given the geological impracticality of underground mining due to unconsolidated rock layers, open-cast methods have been the preferred approach. These open-cast mining sites are strategically positioned within rural areas adjacent to towns, villages, and essential infrastructure, thereby presenting a formidable challenge in terms of restoring the landscape sustainably.
The initiation of mining operations in the 20th century led to the relocation of affected local communities. These extensive mining projects brought a massive deforestation of the Hambach Forest, the region's largest expanse of woodland. Prior to the beginning of mining activities, the Hambach Forest covered an impressive 5,500 hectares. Unfortunately, contemporary estimations suggest that a mere 1,100 hectares of the forest remain, with these remaining woodlands facing imminent danger as a result of ongoing mining operations.(Dickmann, 2011, Tang et al., 2020, Gerwin et al., 2023).

1.2. Remote sensing and SAR interferometry

Synthetic Aperture Radar (SAR) is a remote sensing technique that uses active instruments to transmit microwave pulses towards the Earth's surface and then capture the echoes or backscattered radiation reaching back to the sensor (Massonnet & Feigl,

1998,Rosen et al., 2000, Hanssen, 2001 and Colesanti & Wasowski, 2006). The data acquired by SAR sensors is subsequently structured into a two-dimensional image, where the dimensions correspond to both the Line of Sight (LoS) between the sensor and the target (referred to as slant range) and the platform's flight trajectory (known as azimuth).

Moreover, being an active system, SAR sensors do not rely on solar radiation for functioning, and they can operate independently of cloud cover or weather conditions, which makes SAR a reliable tool, and important for many geodesic and remote sensing applications.

SAR interferometry (InSAR) is a remote sensing technique that exploits the phase information in SAR measurements to obtain high-detail topographic information of the Earth's surface. With its origins tracing back to 1974, InSAR had its initial breakthrough as a technique primarily aimed at enhancing the accuracy of topographic maps (in particular Digital Elevation Models, DEMs). However, its practical applications extended beyond this initial purpose as demonstrated by (Massonnet et al., (1993) who revealed InSAR's additional capability to identify ground surface deformation phenomena, achieved through the extraction of the topographical signal from SAR interferograms.
InSAR has emerged as a significant leap forward in the field of remote sensing, facilitating the precise mapping and real-time monitoring of potentially catastrophic events, such as subsidence, earthquakes or landslides. (Calcaterra et al., 2008, Ng et al., 2017 Shirani & Pasandi, 2019 and others). This technological progress owes its significance to its notable features, including high-resolution imagery, frequent data acquisition from a variety of platforms, and the capability to compute ground displacements with accuracy reaching below a centimetre across extensive areas. The core principle underlying radar interferometry involves the utilization of remote sensing and geodetic systems to derive precise elevation data and surface variations by analyzing the phase discrepancy between two radar images acquired over the same geographical area.

Notably, the Differential InSAR (DInSAR) technique, which involves the multitemporal comparison of phase measurements in SAR time series, has proven to be highly valuable in assessing ground deformations and more specifically in the context of open pit mines.(Pawluszek-Filipiak & Borkowski, 2020,Hartwig et al., 2021, Gojković et al., 2023). In contrast to traditional approaches employed in the monitoring of landslides, DInSAR presents a distinct benefit by rapidly gathering data related to surface deformations across extensive and vulnerable regions, rendering expedited insight at reduced costs. In this context, DInSAR comes out as the foremost method for the detection and comprehensive analysis of ground displacement phenomena within the domain of remote sensing and geodetic investigations and studies.

In fact, numerous researchers have proven the effectiveness of the DInSAR technique in examining landslides and open-pit mine failures(Fruneau & Sarti, 2000,Sousa et al., 2010, Herrera et al., 2010,Hongdong et al., 2011,Dick et al., 2015, Gheorghe & Armaş, 2016, Mirmazloumi et al., 2022,Zhang et al., 2023).

The Persistent Scatterer (PS) technique is a DinSAR technique that was first introduced by Ferretti et al. (2001a) and further investigated byColesanti (2003) and Colesanti & Wasowski (2006). PS was proposed as a solution to the challenges of InSAR that can be impacted by temporal, atmospheric or geometrical decorrelation of the multitemporal SAR signal, which brings errors into surface monitoring applications. This technique depends on phase data obtained from individual isolated entities known as persistent scatterers (PSs). These scatterers are stable terrain features with a high coherence in

the multitemporal data acquisition, normally represented by buildings, roads, and other urban infrastructure elements. By focusing on these stable points, the approach enables the correction of atmospheric artefacts and the precise tracking of ground deformation thus enhancing the accuracy of the obtained products. When the atmospheric artefacts are corrected and completely removed, deformation measurements with very high accuracy are obtained.

Another technique is the Small Baseline Subset (SBAS), used to monitor slow surface displacements, such as ground subsidence (Tang et al.,2020), landslides (Tong & Schmidt, 2016) and seismic activity over a wide area by selecting pairs of SAR images with small temporal baselines (Li et al., 2022). SBAS focuses on Distributed Scatterers (DS), frequently encountered in natural occurrences, they are usually characterised by lower amplitudes and phase stability (Perissin & Ferretti, 2007).

Finally, the last category of methodologies encompasses integrated approaches, as initiated by SqueeSAR®, an innovation introduced by TRE ALTAMIRA. These techniques utilize both PS and DS principles, to maximize information extraction from multi-temporal datasets. The signal from DS combines radar returns from similar pixels, leading to PSI analyses with maintained spatial resolution. However, DS-based results represent larger areas, not individual cells (Ferretti et al., 2011).

In recent years, Artificial Intelligence (AI) has played a significant role in advancing InSAR technology. Some important contributions and applications include Machine learning algorithms used, for instance, to correct phase ambiguities (Zhang & Lu, 2022) for phase unwrapping (Murdaca et al., 2022), or for big data radar processing (Zhang et al., 2023) and other diverse applications that reveal the great potential of AI applications in remote sensing(Janga et al., 2023).

1.3. Objectives

The main objective of this Master's Thesis is to assess the accuracy of the Persistent Scatterer Differential Interferometry SAR (PS-DinSAR) technique for detecting, monitoring and forecasting the behaviour of areas affected by ground subsidence or slope instability. With this aim, a case study is carried out, which takes place in the Hambach open-pit lignite mine, located in the North Rhine-Westphalia region in Western Germany. The study covers a period of two years (from January 2021 to December 2022), and the main data source for the analysis is the Sentinel-1 image record acquired in this period, in particular the 88 scenes acquired in descending track.

Hence specific objectives (SO) of this study are specified below:

-SO1: Implement a PS-DinSAR analysis on a base period of one year (2021) calibrating the obtained displacement and velocity measurements with GNSS station data.
-SO2: Evaluate the results obtained for the base period by comparing them with data already available for the study area, in particular the European Ground Motion Service (EGMS) and the German Ground Motion Service (BodenBewegungsdienst Deutschland – BBD, GMG).
-SO3: Employ the PS-DinSAR technique utilizing subsets of six Sentinel-1 acquisitions for the 2022 year to conduct monitoring of the specified AOI.
-SO4: Conduct an assessment to determine the applicability of PS-DinSAR points in the context of civil infrastructure.

-SO5: Apply the Trend Change (TC) and Acceleration Indexes (AcI) as analytical tools for assessment and analysis of ground stability within the Rhenish open-pit mining region.

The specific objectives cover different stages necessary to assess the utility of the approach from the point of view of the end user. Therefore, this Master's Thesis aims to contribute to the field of SAR-based mining monitoring and its potential for wider infrastructure applications.

2. Data Description

2.1. Study area

This study focuses on investigating vertical ground displacement and slope instability within the Rhenish Coalfield region in Germany. This region is widely recognized as one of the most challenging areas in the country (and Europe), primarily because of its significant ground movements, as indicated by the EGMS-CLMS (2023).

The study area is situated in the North Rhine-Westphalia region of Western Germany, encompassing a small portion of the Netherlands. The Rhenish lignite mining area comprises three open pit mines: North Garzweiler I/II, located near the city of Jüchen; Hambach mine, the largest in the region and the entire country, situated adjacent to the cities of Elsdorf and Berrendorf; and Inden I/II, positioned near the cities of Inden and Jülich (Fig.1).

According to the regional electricity company (Rheinisch-Westfälisches Elektrizitätswerk Aktiengesellschaft, RWE), mining operations in this area commenced in 1978 near the Hambach district of Niederzier. As of the end of 2021, the open-cast mine has reached a depth of 411 meters, covering an area of approximately 457 square kilometres.

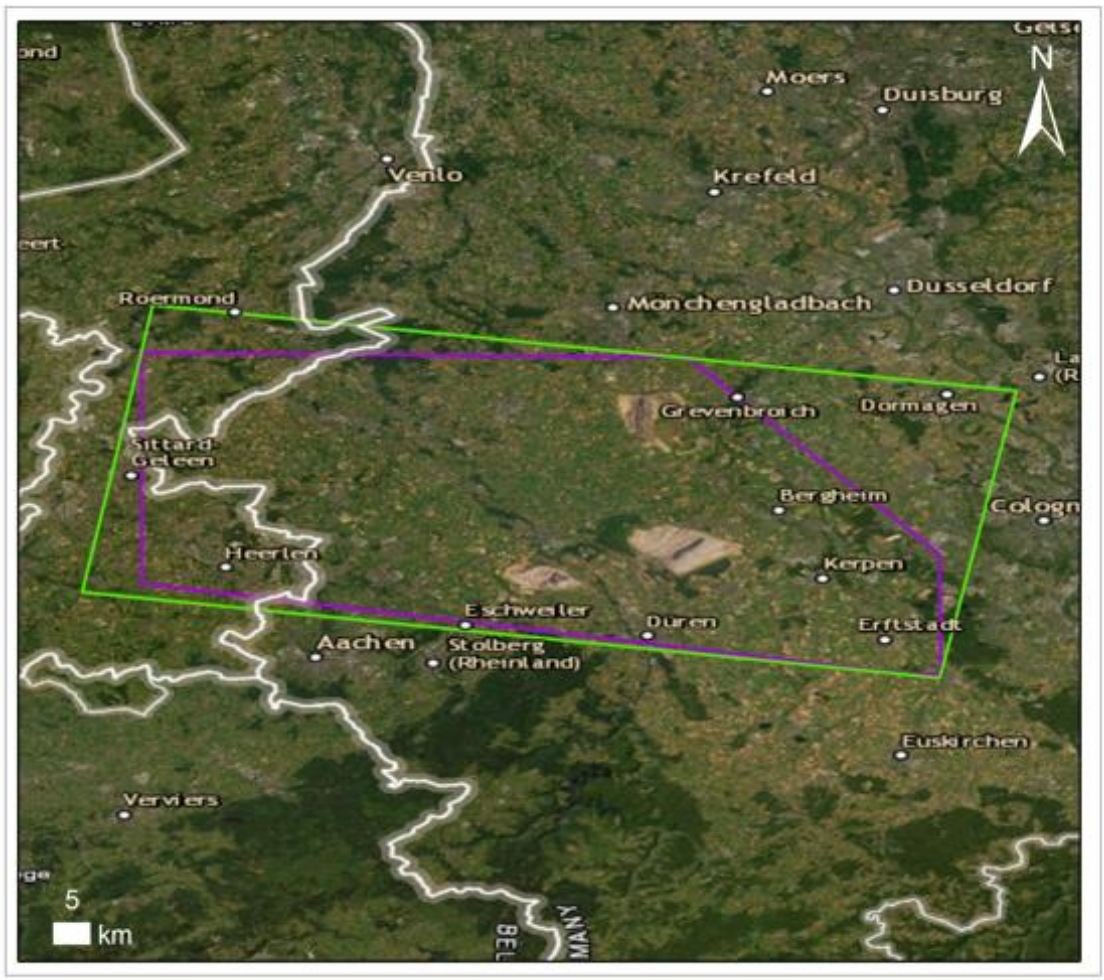

Fig.1 Detail of the study site with the North Garzweiler, Hambach opencast mines in the middle and the Inden opencast mine southwest of Hambach mine. The purple line represents the area of interest, and the green line is the footprint of the descending Sentinel-1 track.

The mines are in operation, with an annual production of around 23 million tonnes of lignite coal (Table 1).

Table 1 Chart of the Rhenish lignite mining area in Germany according to RWE (2023).

Mine	Condition	Coal output (M/t year)	Area (km^2)	Depth (m)	Operations
Hambach	In operation	23	457	411	1984-2030
Garzweiler II	In operation	30	35	210	2006 – 2038
Inden I/II	In operation	15	16.5	230	1981- 2029

A significant part of the study area is located in the Lower Rhine Basin, which was formed during the Cenozoic era (Bogena et al., 2005). Yet, the southwestern part enters the Rhenish Massif, where the geological materials originated from the Paleozoic era. The geological composition of the area reveals a diverse range of lithological formations (*European Geological Data Infrastructure (EGDI)*, 2023). The dominant lithology consists of Pleistocene and Holocene sand and silt, indicating a significant deposition of sedimentary materials during those epochs. Additionally, the area contains Miocene and Late Cretaceous clay deposits. Notably, the southern part of the area exhibits

occurrences of Pliocene chalk, Lower Pennsylvanian claystone, and shale. The region's rich lignite coal is the cause of its socio-economical interests and related issues.

2.2. Sentinel-1 imagery

The Sentinel-1 mission consists of a constellation of C-band (SAR) satellites, which is the continuation of the European Space Agency's (ESA) previous missions, namely the European Remote Sensing Satellite (ERS-1, -2) and the Environmental Satellite (ENVISAT) SAR missions. The Sentinel-1 constellation was initially planned to consist of two units, namely A and B, to ensure consistent data availability and increased temporal resolution. By operating in tandem, the two satellites can generate valuable datasets for Copernicus Services, providing accurate and up-to-date information for a wide range of environmental monitoring and Earth observation applications. (Yague-Martinez et al., 2016). Additionally, their independence from weather conditions allows them to consistently capture high-quality information regardless of atmospheric disturbances. This capability is particularly valuable for detecting and monitoring land deformations.

The initial launch of the Sentinel-1A satellite took place in April 2014, marking the beginning of the Sentinel-1 mission. Subsequently, two years later, in April 2016, the second satellite, Sentinel-1B, was successfully launched. The revisit time is 12 days for each satellite. However, when both Sentinel-1A and 1B operate together, the revisit period is reduced to 6 days (*Copernicus*, 2023). These two satellites operate within the same orbit, ensuring their comparability and synchronized observations; this enhances the precision and accuracy of the data they collect.

Unfortunately, on 23 December 2021, Sentinel-1B suffered a failure in its power supply unit, which could not be repaired by ESA engineers. Therefore, in August 2022, ESA announced the end of the Sentinel-1B mission and reinforced efforts towards the launch of Sentinel-1C between 2024 and 2026. The revisit schedule for Sentinel-1 varies, with a 6-day interval observed between 2017 and 2021, and a 12-day interval for the years 2015-2016 and 2022-2023.

Regarding operation modes, Sentinel-1 can acquire data in four exclusive modes: Stripmap (SM), Interferometric Wide swath (IW), Extra Wide swath (EW) and Wave (WV) mode**.** However, the IW mode is given priority as the primary operational mode for land observation. This innovative observation mode, assembles three swaths through the Terrain Observation with Progressive Scans SAR (TOPSAR) concept (European Space Agency, 2023), (Fig. 2), enabling the acquisition of very large scenes of 250 km swath width, with a spatial resolution of 5x20 m, which had never been possible before.

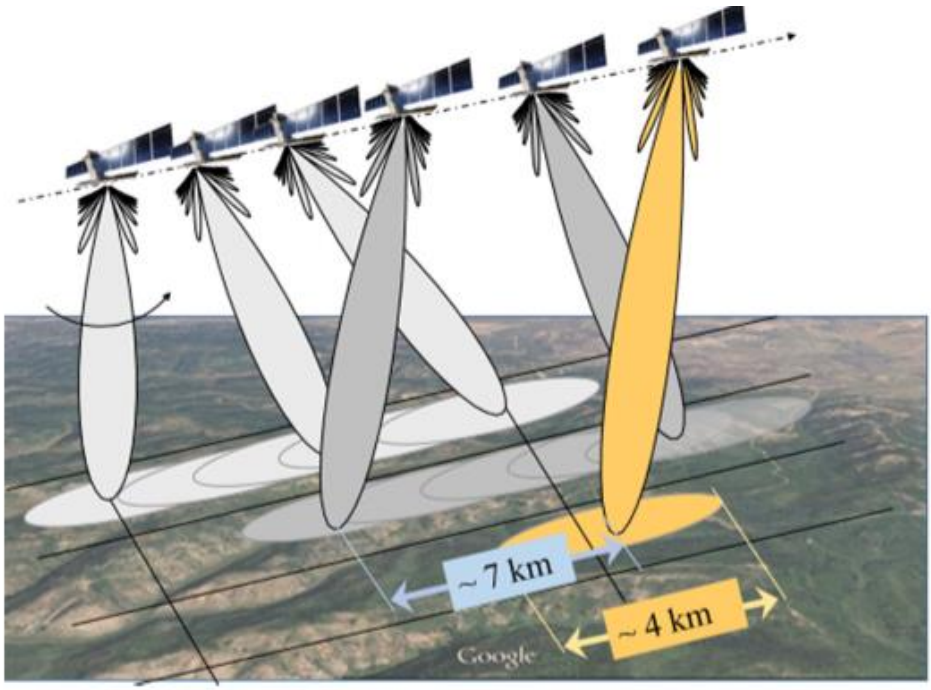

Fig.2 The TOPSAR acquisition mode of Sentinel-1 IW and the three swaths assembled (Monti-Guarnieri et al., 2017).

For this study, the data utilized was acquired in the IW mode, and downloaded as Single-Look Complex (SLC) products, since this format preserves both the amplitude and phase information, necessary for interferometric applications. Since the study period covers 2021 and 2022, data from Sentinel-1A and -1B was used for 2021 and only Sentinel-1A for 2022. The data was obtained from the Alaska Satellite Facility (ASF) repository using the aria2c download utility, which is known for its fast and efficient downloading capabilities for satellite imagery. For this study, the VV polarization channel was only used, discarding the VH that is more affected by phase instabilities.

A total of 88 Sentinel-1A SLC products were downloaded, all of them captured in descending track to ensure geometric consistency. These datasets were divided into two: the first dataset consisted of 58 images captured by Sentinel-1A and -1B from January 2021 to December 2021, and the second dataset comprised 30 images captured by Sentinel-1A from January 2022 to December 2022. Hence, the revisit time was 6 days for the first period and 12 days for the second.

2.3. Digital Elevation Model (DEM)

For interferometric analyses, achieving a precise geometrical matching between subsequent scenes is key. This is possible thanks to the stability of Sentinel-1 satellite orbits but an accurate external Digital Elevation Model (DEM) is also needed (Wang et al., 2017). A DEM is also necessary for the topographic phase removal. However, the areas of open pit mines are in constant change due to excavation, and this could lead to DEM errors (Tang et al., 2020). Therefore, when selecting a DEM for InSAR topographic analysis, two crucial factors need to be taken into account: precision and timeliness.
First, DEM precision should be assessed in terms of both accuracy and resolution. This ensures that the DEM provides reliable and detailed elevation information for accurate phase removal during interferometric processing.

Secondly, the chosen DEM needs to be up-to-date concerning the timeline of the InSAR images. Using an outdated DEM may introduce errors or inconsistencies in the phase removal process, impacting the accuracy of the final results (Lazecký et al., 2015).

The DEM used for this work is the Global and European Digital Elevation Model, (COP-DEM), a Digital Surface Model (DSM) obtained from Copernicus. It has a spatial resolution of 10 meters and covers the period between December 2010 and January 2015. The Coordinate Reference System (CRS) employed is as follows: Horizontal CRS is WGS84-G1150 (EPSG 4326), and the Vertical CRS is EGM2008 (EPSG 3855). The heights provided in this DEM are orthometric, meaning they are referenced to a geoid model that represents the mean sea level. The data is available at COP-DEM (2022). The following sheets have been downloaded: N30E40 and N31E40 to cover the whole Area of Interest (AOI) (Fig.3).

DSM provides a representation of Earth's surface, including terrain and surface features like buildings and vegetation. This makes it an essential tool for monitoring ground deformations such as subsidence, landslides, and earthquakes, particularly in urban areas.

In this study, the focus is on obtaining (PS) points, which are closely related to double bounce backscatter. This phenomenon occurs when an emitted pulse strikes a smooth surface, and the reflected pulse then hits another surface perpendicular to the first, resulting in a strong return of energy towards the sensor (Álvarez Mozos, 2023). This kind of backscattering is common in urban environments, where the DSM excels over the Digital Terrain Model (DTM) in InSAR studies. The DSM's ability to accurately capture surface elements, especially buildings, is crucial for identifying the designated PS points in urban areas. Accurate measurement of ground movement is essential in the DInSAR technique, where the DSM plays an important role in achieving this goal by illustrating changes in elevation spanning the Earth's surface.

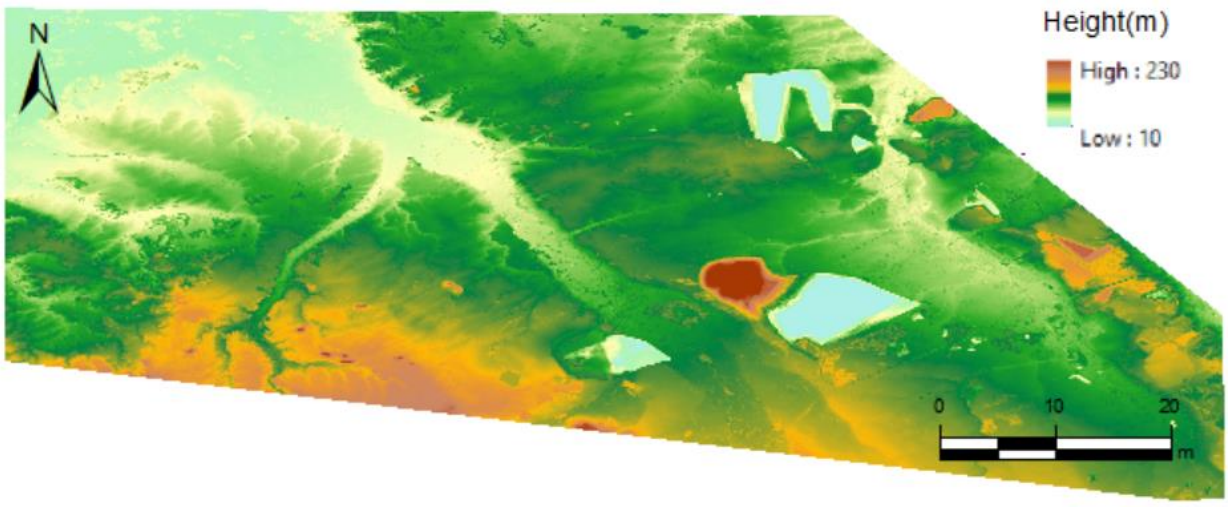

Fig.3. Digital Elevation Model (COP-DEM, 2022) of the area of interest.

2.4. Global Navigation Satellite System (GNSS)

Global Navigation Satellite Systems (GNSS) function as a geodetic infrastructure including constellations like Galileo, GPS, GLONASS and BeiDou, providing both precise measurements and geographic positioning through GNSS stations. According to the research by Farolfi et al. (2019), GNSS serves as a means to mitigate the absence of an absolute reference framework in InSAR products. In the context of interferometry, GNSS stations play an essential role due to their capability to offer continuous and precise measurements of ground displacement.

The GNSS data used in this study was obtained from the service of the Nevada Geodetic Laboratory (NGL). It offers open access to users and gathers information from a wide network of GNSS stations around the world. The reference system of the data is IGS14 and the data are published in tenv3 format (Blewitt et al., 2018), (Fig.4).

Coordinates:
Latitude: 51.035 degrees
Longitude: 6.432 degrees
Height: 156.096 meters

Time Series Data (ascii text)		
24 Hour Final Solutions		
IGS14	tenv3 or tenv	xyz
EU	tenv3	
5 Minute Final Solutions		
IGS14	kenv tar files for download	
Quality Assurance (QA) Files		
IGS14	.qa.gz file download	
5 Minute Troposphere Solutions		
Tot./Wet Zenith Delay, etc.	tar file download	
New!: Loading Predictions. See this README file for explanation.		
IGS14	tenv3 file with extra columns	
Readme Files: *tenv3 format, tenv format, xyz format, kenv format, trop format, QA file format, Loading triplet enhanced tenv3 files* (Note: When using the MIDAS software use the .tenv files linked above)		

Nearest 4 Other Stations	Distance
D627	0.00 km
TITZ	0.01 km
D615	9.33 km
GJ03	14.16 km

Fig. 4 General information of one of the GNSS stations (TIT2) from NGL used in this work.

Within the AOI, there are a total of five GNSS stations. However, it should be noted that only three of these stations covered the period of interest (January 2021 to December 2022). The third station, although located slightly outside of the AOI, may still be considered for calibration purposes due to its proximity (Fig 5).

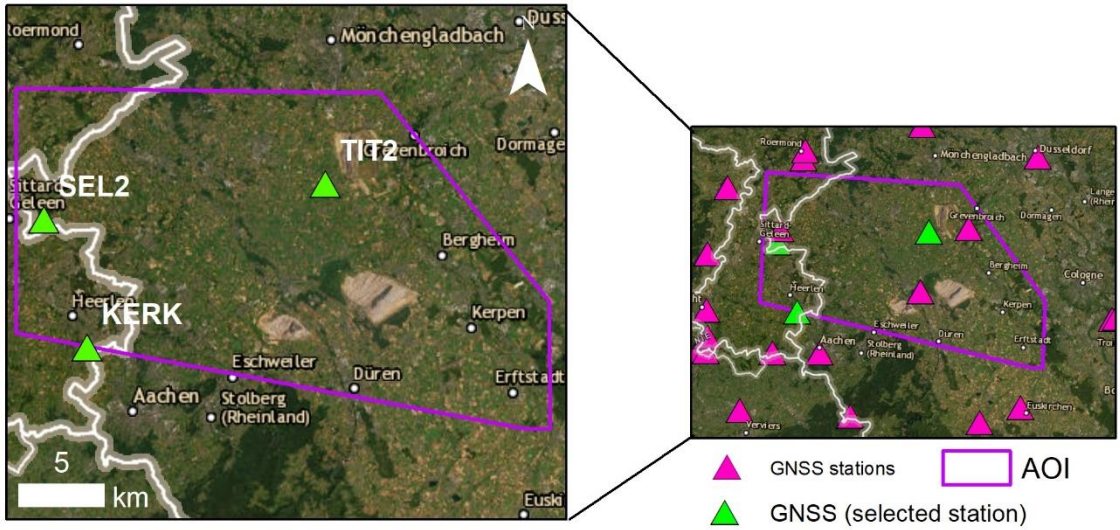

Fig. 5 GNSS stations around the area of interest (right) and the three stations chosen:- SEL2, KERK and TIT2 (left).

2.5. European Ground Motion Service (EGMS)

Employing InSAR technology, the EGMS marks a pioneering effort in continent-wide ground deformation monitoring, harnessing full-resolution processing of S-1 satellite data across the majority of Europe. This service encompasses all Copernicus-contributing countries during its initial implementation phase. Its objective is to offer quality data and free access to the largest possible number of users at the global level on land subsidence, slope instabilities, etc.

The EGMS was created to introduce an original and distinctive geospatial data layer across Europe, enhancing the Copernicus Land Monitoring Service (CLMS) portfolio (Costantini et al., 2021), (Fig.6). It was tailored for the precise measurement of ground movement at levels of detail as small as millimetres. This relates to various geological phenomena such as subsidence, landslides, tectonic activities, earthquakes, and volcanic occurrences, all of which influence the ground stability, including human-created slopes, mining zones, structures, and infrastructure. This initiative will also foster additional value through downstream applications in both public and private sectors.

Scheduled for its inaugural delivery in September 2023, the service is already running at the moment of writing this thesis. The initial baseline product employs S-1 data from 2018 to 2022. with subsequent annual updates being planned, ensuring consistency, harmonization, interoperability, and standardization of the products across national boundaries on a unified European dataset. To encourage broad utilization by the expanding Copernicus user community and the general public, the EGMS provides tools for visualization, exploration, analysis and download, while also integrating elements that encourage the adoption of best practices and active user participation.
EGMS releases data with different levels of processing:

- Calibrated product (Level 2b) This product presents displacements in the LOS direction (from both ascending and descending geometries), calibrated using a GNSS reference network and with a standardized reference frame. Thus this product variation is not suitable for the current study, as it does not include vertical displacement data.

- Ortho product (Level 3) is presented through two geospatial layers: one for vertical displacement and another for the east-west components of displacement. Both layers are aligned with the GNSS reference network within a shared reference framework and resampled to a 100 m grid.

All the products of the EGMS can be downloaded, once the AOI is determined. Furthermore, additional information about each PS point can be obtained, by selecting the point, as illustrated in Fig. 7 and Fig.8.

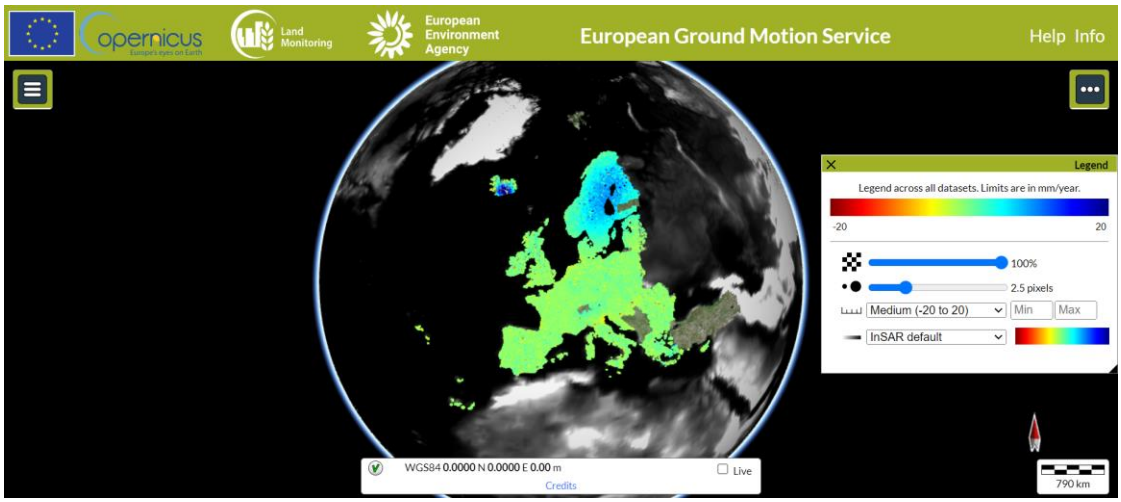

Fig.6 EGMS web explorer

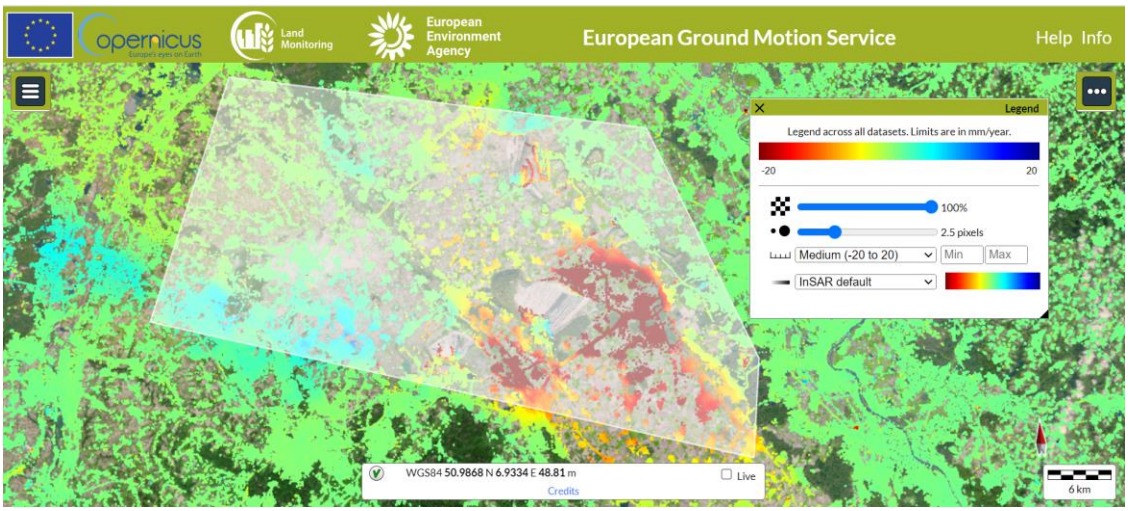

Fig. 7 The AOI over a layer of vertical displacements (Ortho product) in the EGMS explorer.

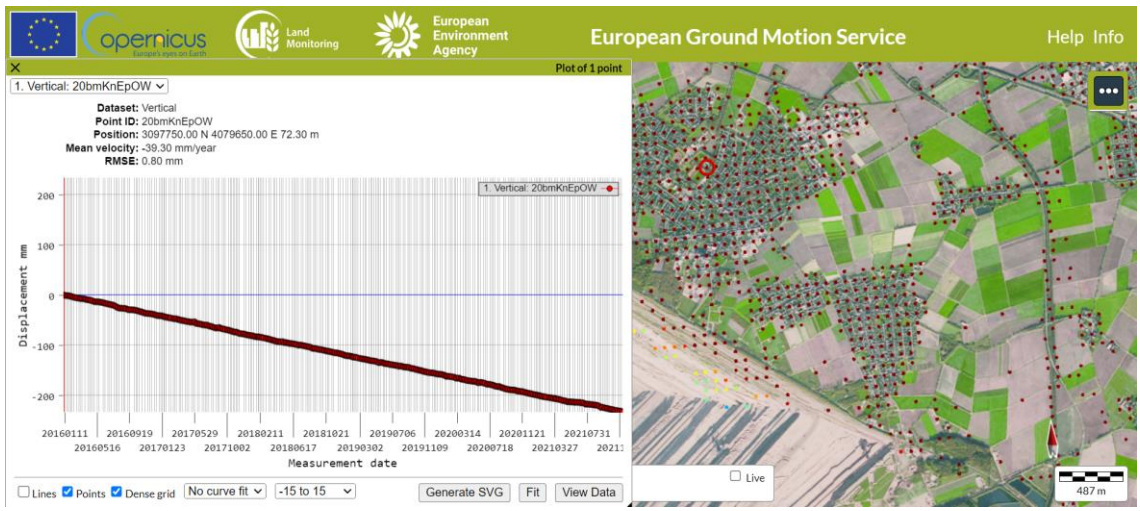

Fig. 8 EGMS Explorer in detail, and vertical displacement temporal trend for a selected point.

2.6. Ground Motion Germany (GMG)

The Ground Motion Service Germany (GMS) was established at the end of November 2019 and relies on Sentinel-1 satellite images, including both 1A and 1B sensors, that have been processed meticulously by the German Aerospace Centre (DLR). To facilitate the practical use of satellite interferometric products, the "Ground Motion Service Germany," referred to as BodenBewegungsdienst Deutschland (BBD), was developed in collaboration with various stakeholders, including the Federal Institute for Geosciences and Natural Resources (BGR), the user community, land surveying agencies, small and medium-sized enterprises, and research institutions. The data is distributed in the form of deformation maps that have been corrected using GNSS data, falling into the Level 2b category in agreement with the EGMS portfolio, however, ortho products (Level 3) are also provided. The main objective of the validation activities was to comprehensively evaluate the precision and accuracy of the deformation map generated by the BBD.

Data can be downloaded within a search window of up to 400 square kilometres, a small part of the AOI above the vertical displacement layer (Fig. 9).

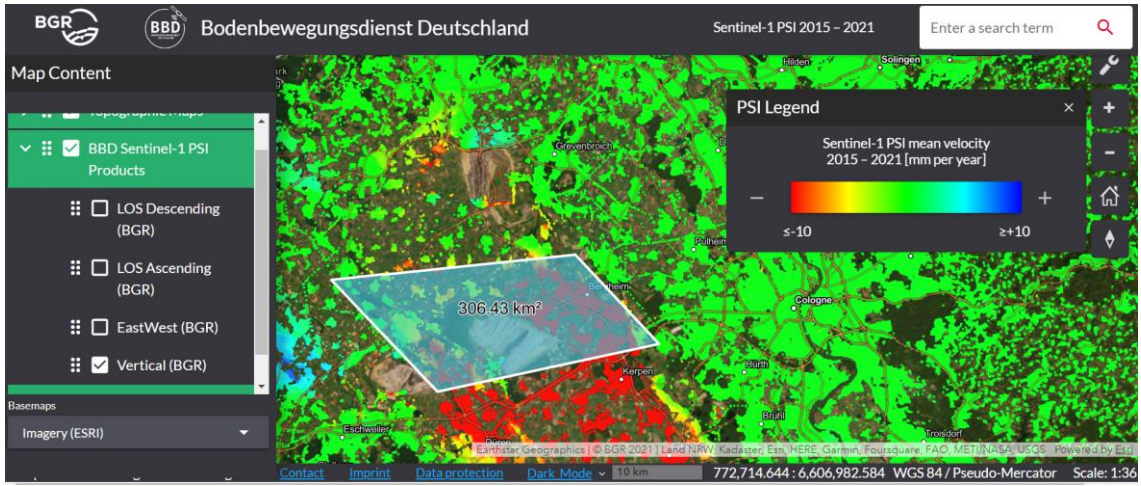

Fig.9 GMG explorer and part of the AOI over a vertical displacement velocity layer.

Similar to EGMS Explorer, GMG also has the option to choose a singular point from the PS points and get additional information about the time series (Fig.10).

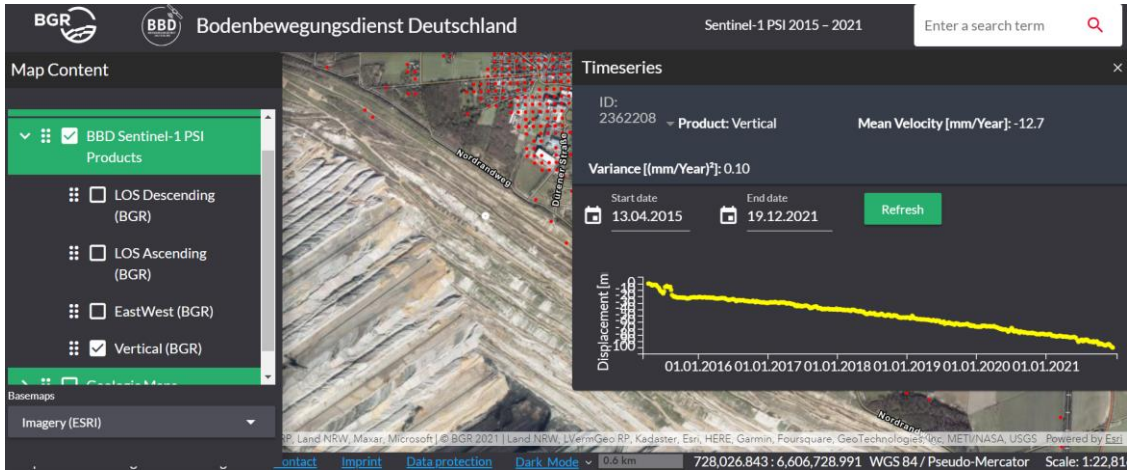

Fig. 10 Level 2b and Level 3 products from the GMG explorer and time series are presented for a singular point.

2.7. Software

ENVI is a software developed by NV5 Geospatial Solutions that is widely used for image processing, geospatial analysis, and interpretation. The software provides a modular set of tools, including SARscape, which is specifically designed for SAR interferometry applications, including PS and SBAS techniques and workflows for an easy generation of DEM products and deformation maps. Additionally, ENVI is tightly integrated with ESRI ArcGIS software, allowing for enhanced interpretation and analysis of the results. The version of the software used for the study was 5.6.3. Other software such as ArcMap, QGIS and, Microsoft Excel were also used in this work. Some specific processing and analysis scripts were also written in Python.

3. Methodology

Before commencing the interferometric analysis, it is essential to perform an initial data preprocessing step to customize the whole process according to the precise requirements of the software and processing framework. Subsequently, the multi-temporal DInSAR PSI processing was executed. After obtaining displacement and velocity values a comparison was performed against the products of the EGMS and GMG. Then a monitoring case study was executed with the S-1 imagery of 2022, utilizing the Edit Connection Graph Tool in ENVI SARscape and further analysis was conducted using Python, focusing on some indicators: Trend Change Indicator (TI) and Acceleration Indicator (AcI). Finally land use spatial integration mapping was obtained through the Open Street Maps (OSM) layer for the territory of Germany (Fig.11).

3.1. PS – DinSAR multi–stack process

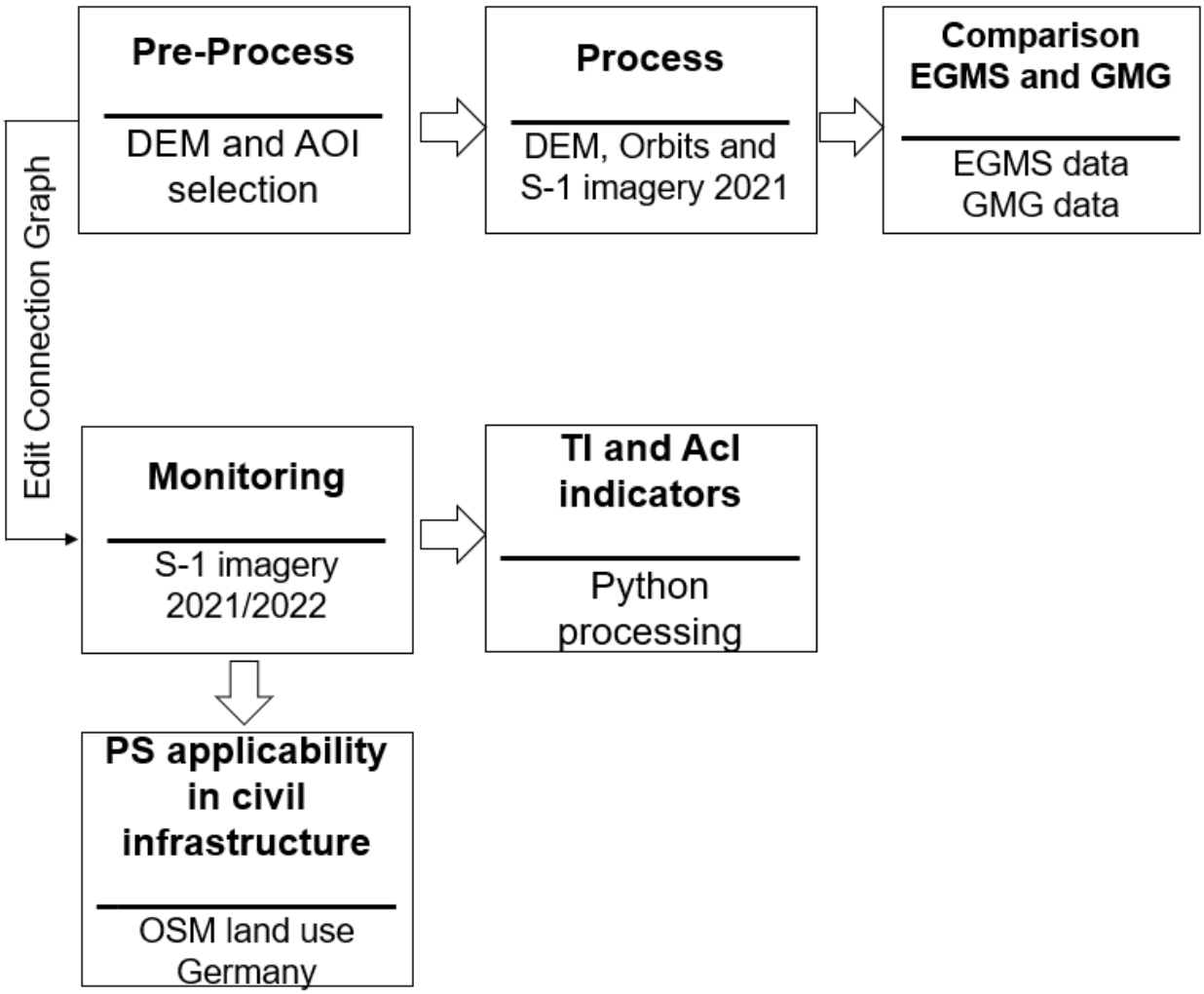

Fig. 11 General flowchart of the analysis.

3.1.1. Pre – Process

This stage involved several essential activities: configuration of ENVI preferences and establishing SARscape default parameters in alignment with the specific data characteristics. And also: initial DEM preparation, the acquisition of precise orbits, and the downloading of the image data.

To facilitate subsequent analyses, the DEM was integrated into the ENVI software through the utilization of the SARscape tool. During this conversion process, the height information of the DEM was transformed from its native geoid state (EGM 2008) to the ellipsoidal reference (WGS 1984).

Regarding the preprocessing methodologies, a total of seven iterations of imagery importation were executed. Initially, the imagery for the year 2021 was imported. Subsequently, for the year 2022, the data was classified into six distinct subsets, referred to as monitoring segments. Each of these segments comprised five individual images.

3.1.2. Process

ENVI SARscape 5.6.3. utilizes a multi-stage preprocessing method, employing a step-by-step modelling approach, with the main goal of obtaining improved coherence, velocity, and elevation values (Fig.12). Further information about the parameters of the process (7.1.).

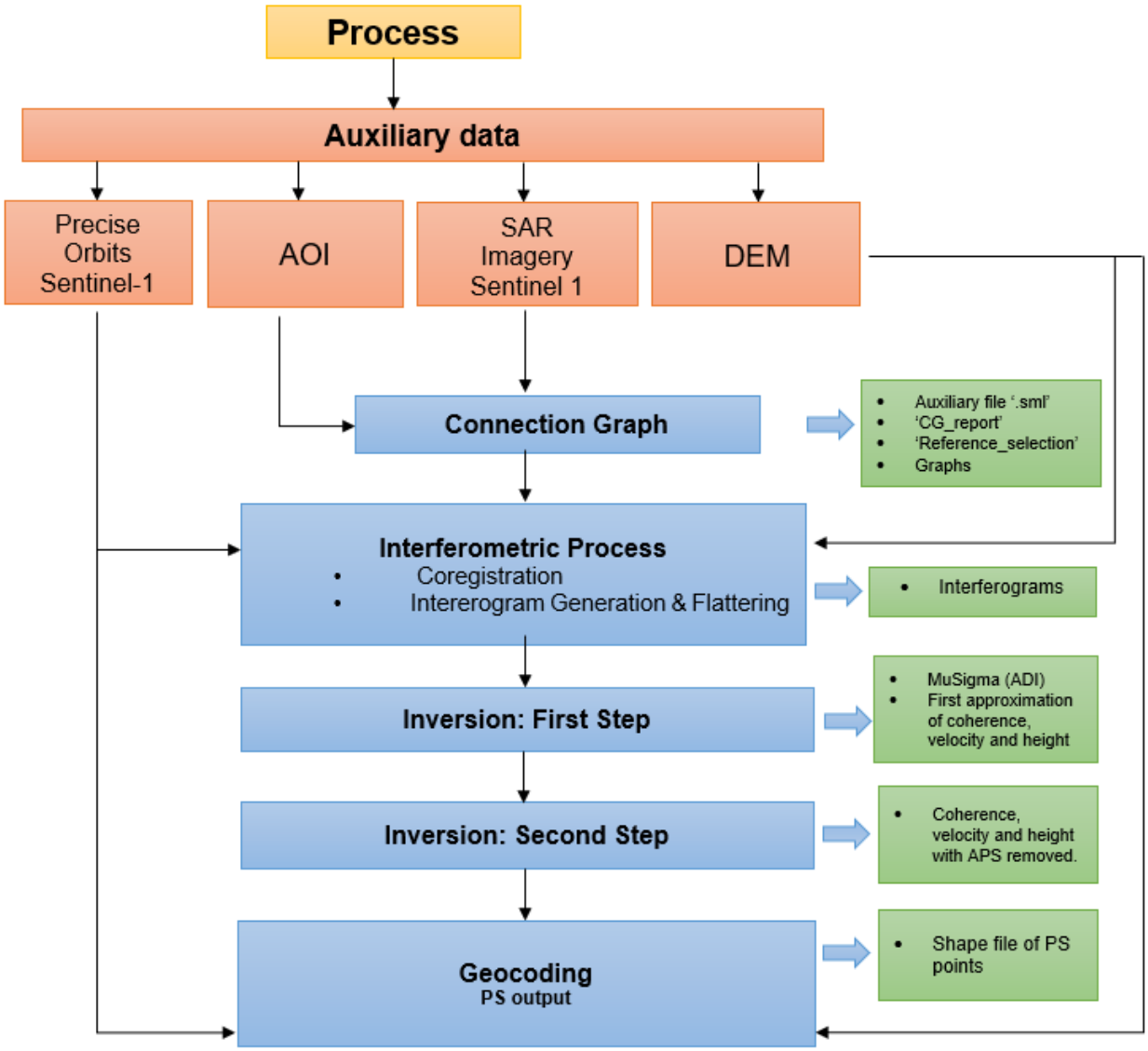

Fig.12 Flowchart of the PSI process in ENVI SARscape 5.6.3. Orange represents methods, red auxiliary data, blue process and green outputs.

According to Wassie et al. (2022), advanced DinSAR techniques focus on acquiring a time series of ground deformations, evaluating the state of specific objects on the Earth's surface in relation to spatial and temporal references. By utilizing multiple SAR interferograms, the analysis aims to estimate how the deformation evolves over time. Additionally, the technique requires selecting pixels that demonstrate coherence in both space and time, where precise identification of by ground deformations processes can be obtained.

As stated by Ferretti et al.,(2000, 2001), the technique under discussion is primarily centred around the identification of PS, points that exhibit coherence over extended time intervals. These PS are commonly observed in urban environments including structures such as buildings, bridges, and roads.

A minimum of 20 images have to be imported to initiate the PS processing in SARscape.The imagery, used as input data must be obtained from the same sensor, with the same observation geometry and polarization.

The process consists of five mandatory steps.

1-Connection Graph

All images are imported to establish a grid of 'slaves' alongside a master image, which serves as a foundation for generating diverse interferograms. The master image plays a role as a benchmark against which the other slave images are aligned.
The parameters used in this process are as follows:

The temporal baseline (TB) represents the time gap between the acquisition of the master and the slave images. Opting for a shorter temporal baseline can enhance interferometric coherence, in order to limit the noise effect, known as the decorrelation phenomenon (Roy et al., 2022, Mora et al., 2002). Therefore, a central image in the period of analysis is normally selected as the master.

The spatial baseline (SB) is also an important parameter in SAR interferometric processing. It is represented by the vector connecting the sensor position at the moment of each image acquisition. This vector can be decomposed into a parallel and perpendicular baseline component (Xue et al., 2020). It is convenient for the SB to be small, otherwise, this will affect the quality of the interferograms and the accuracy of the measured displacement. Additionally, a SB prevents errors due to changes in the Earth's surface. The narrow Sentinel-1 orbital tube makes the SB very small, between ±100m, contributing towards a consistent and precise displacement measuring ability (Geudtner et al., 2014, Escayo et al., 2022).

Selecting a master image centred in the SB with respect to slaves helps mitigate the impact of geometric and topographic distortions, especially in regions with pronounced topography. The master image can be chosen either manually or automatically, following the above-mentioned criteria of minimizing both TB and SB. In this study, the automatic approach was employed, and the master image was automatically selected precisely at the midpoint of the TB and SB space, which was July 22, 2021 (Fig.13).

The final output of this processing step consists of an auxiliary file to be imported at each subsequent stage, two plots illustrating time-position and time-baseline relationships (Fig. 13) and a multilooked intensity master image (Fig. 14).

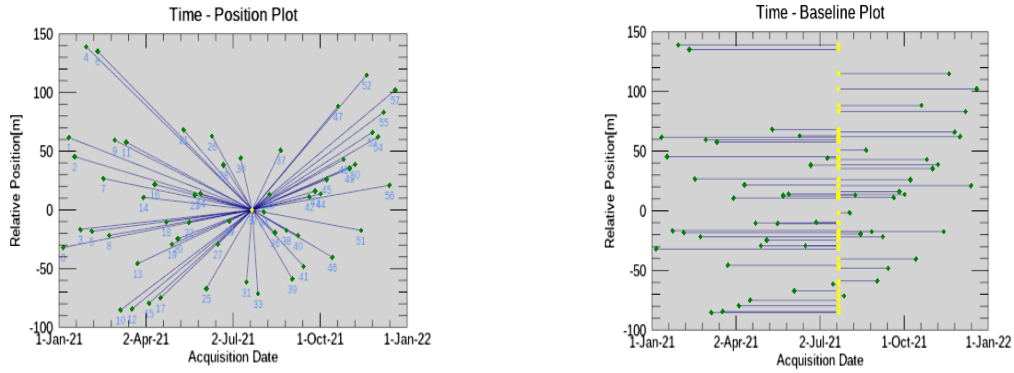

Fig. 13 Plots generated by the Connection graph tool showing the spatial and temporal baseline of the selected master image.

The intensity products are observed in the slant range, as the correction of the observation geometry has not been applied at this point. (Fig.14)

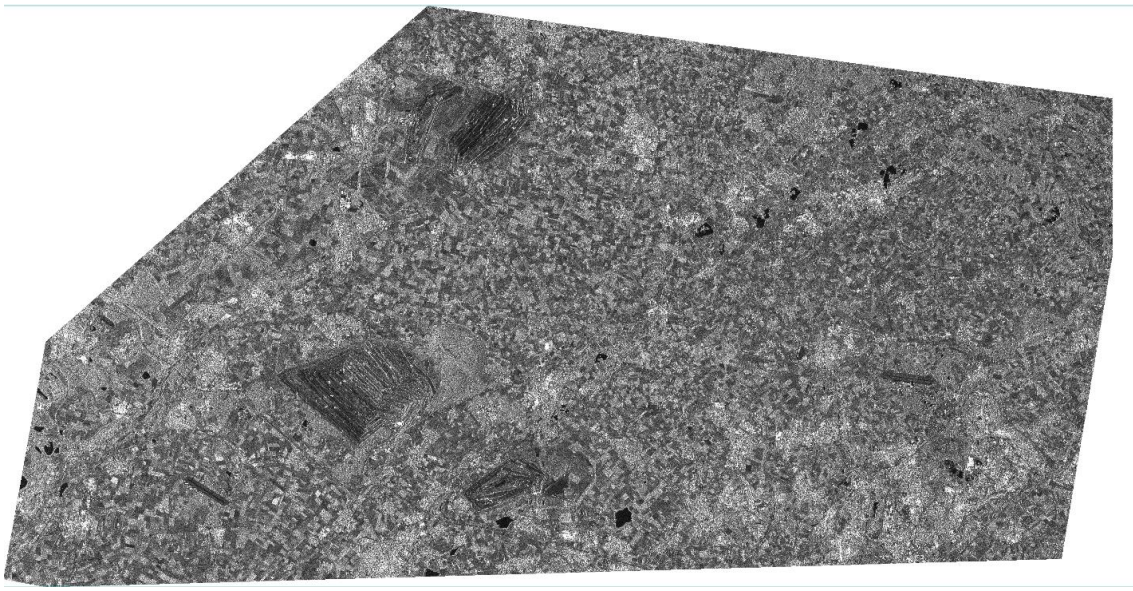

Fig. 14 Multilooked intensity master image July 22, 2021, in slant range geometry.

Interferometric Process

During the Interferometric Process, the following operations are executed automatically: Coregistration, Interferogram Generation, Flattening, and Generic Atmospheric Correction Online Service (GACOS) filter. In Coregistration, slave images are aligned with the master image. Interferograms are then generated in the Interferogram Generation phase, producing $n-1$ interferograms for n images (slaves and master), that is, 57 interferograms. In the next phase, a Digital Elevation Model (DEM) is used to remove the topographic phase, a crucial step for the accurate interpretation and measurement of ground deformation analysis. The outputs generated at this stage are

an intensity average image, a set of interferograms, and a reprojected DEM in slant range geometry. Finally, the GACOS filter (Yu et al., 2018) was implemented to correct for the influence of atmospheric components (in particular water vapour) on the interferogram phase data. The GACOs filter is freely available at (http ://www.gacos.net/).

As an example (Fig.15), the intensity of the master (2021/07/22) and a slave image (2021/09/02) is shown, along with the flattened interferogram obtained between these two scenes.

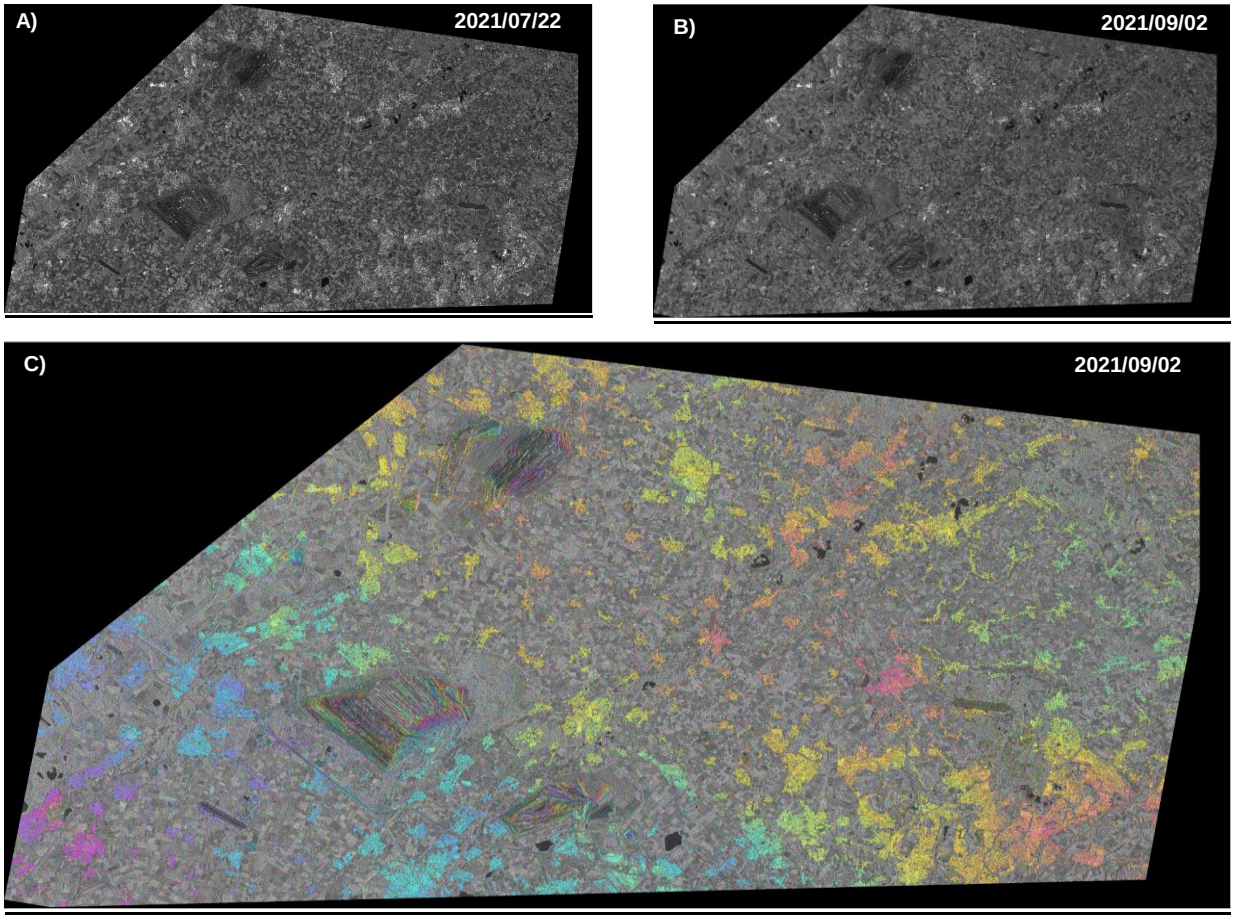

Fig.15 Interferogram generation between the master image 2021/07/22 and a slave 2021/09/02.

First Inversion

The First Inversion stage focuses on identifying PS points, which are based on the Amplitude Dispersion Index (ADI). ADI is determined as the ratio between the standard deviation σA and the mean value of the image intensities within a specified time interval (Kotulak et al., 2022).

$$ADI = \frac{\sigma A}{mA}$$

SARscape uses a second term to refer to this concept: the MuSigma parameter that, in fact, is calculated as the inverse of ADI (the ratio between the mean intensity and its standard deviation). Therefore, low ADI values (high MuSigma) correspond to stable terrain elements (low standard deviation) with a strong backscatter response (high mean intensity), which typically correspond to urban areas or man-made objects. In contrast, high ADI values (low MuSigma) represent elements with high backscatter variability typical of rural areas and vegetation, where the interferometric phase cannot be used. Typically, PS points can be evaluated as suitable for PS analysis when its ADI is lower than 0.25, indicating stable backscatter characteristics.

In this study, the MuSigma threshold was established, selecting pixels > 3.2 as Persistent Scatterer Candidates (PSC) and discarding the rest. This threshold was set during the Geocoding stage. The MuSigma was computed automatically on radiometrically calibrated images.

Additionally, refinement and re-flattening were applied to all interferograms utilizing the DEM along with low-pass-filtering techniques. The final products include a preliminary estimation of the mean displacement velocity (mm/year) of the PS points, and height values (elevation changes in meters), made with respect to the original DEM, coherence values (multitemporal coherence) and MuSigma values.

Figure 16 and Fig.17 A) presents the preliminary estimation of mean velocity, with values ranging from 100 to -100 mm/year and a mean value of -9.22 mm/year. In Figure 16 and Fig.17 B), corresponding to the correction (in meters) concerning the input DEM, values range from 70 to -70 m, with a mean value of -10.88 m. After atmospheric correction, the final velocity and height products are shown in Figures 16 and 17 C). The velocity displacement values remain within the range of 100 to -100 mm/year, with a mean value of -11.61 mm/year. Figure 16 and 17 D) displays the height product with values ranging from 87 to -52 m and a mean value of -4.02 m.

In general, the results from the second inversion exhibit higher values of velocity and height. Notably, in both cases, a more uniform and less noisy distribution of these values across the entire spatial context is achieved after the second inversion.

Velocity first 2021

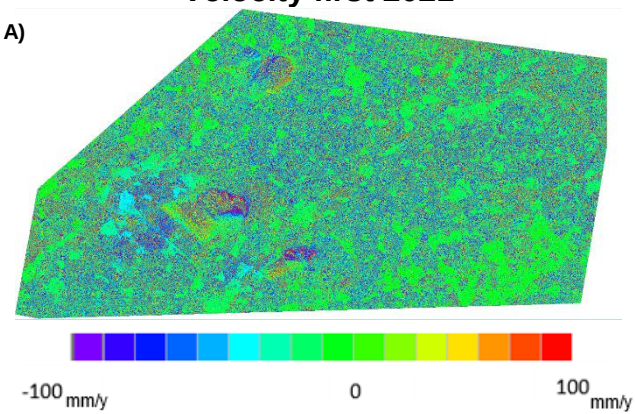

Height first 2021

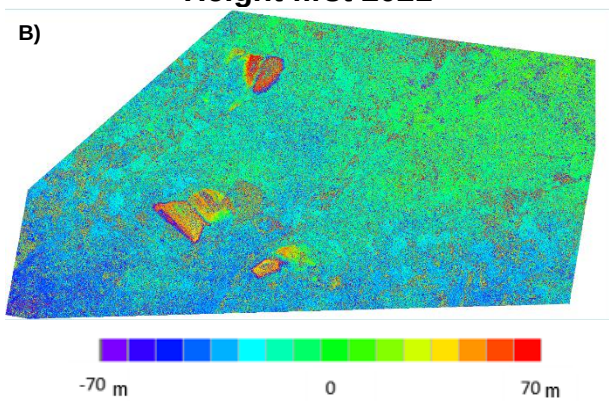

Velocity second 2021

Height second 2021

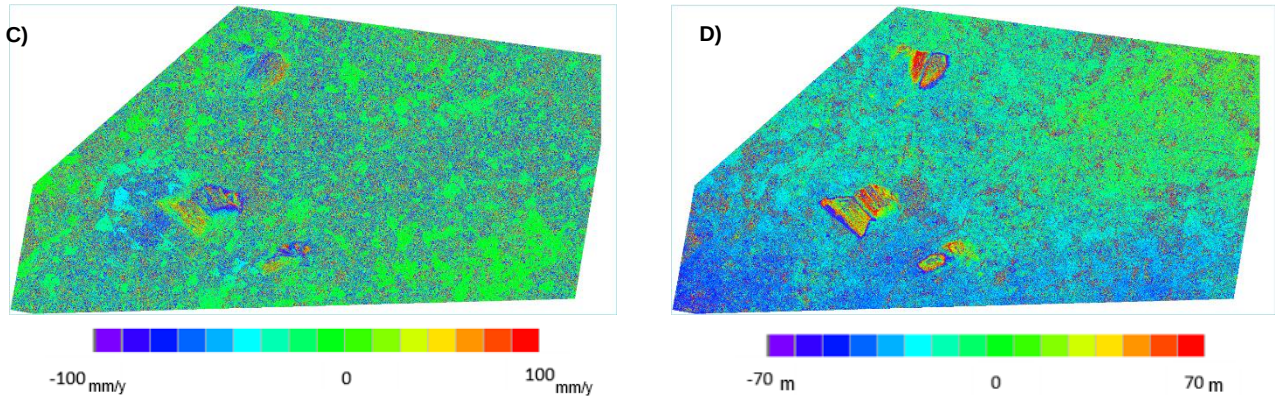

Fig 16. Final products of First and Second Inversions. A and B represent displacement velocity in mm/year and residual height from the First Inversion without atmosphere correction and C and D represent the final velocity displacement in mm/year and the height after atmospheric correction.

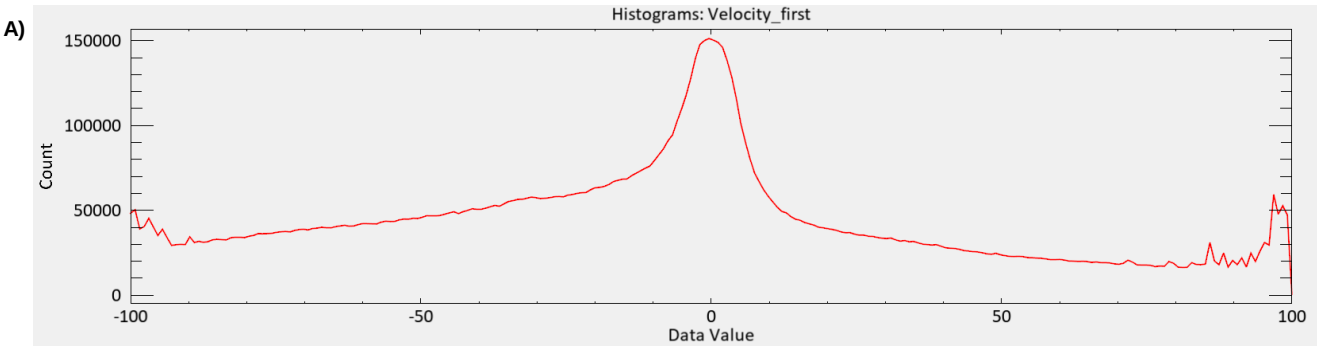

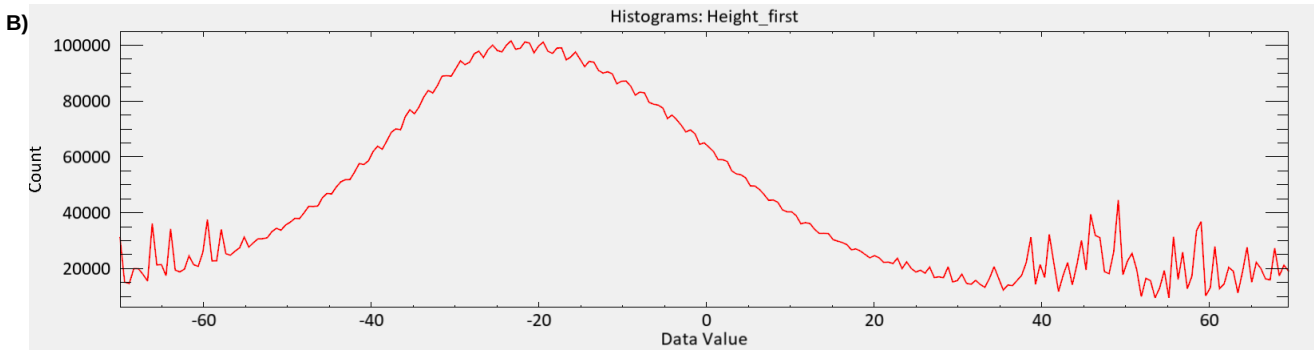

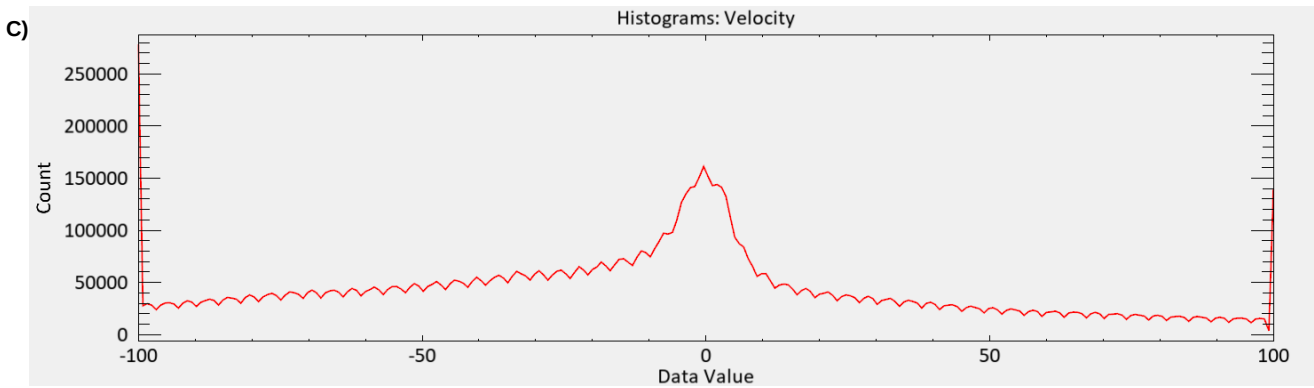

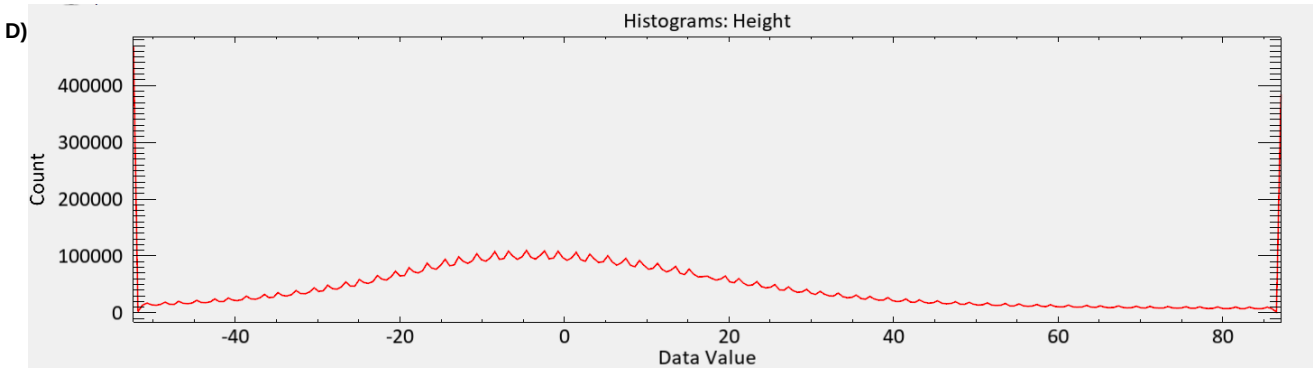

Fig. 17. Histograms for both Inversions' final products. A and B histograms correspond to the velocity and height from the First Inversion, and C and D represent histograms corresponding to the velocity and height of the Second Inversion, after atmospheric removal.

Second Inversion

In the Second Inversion step, atmospheric phase screen (APS) filtering was implemented on the products generated in the previous step. APS was removed from the interferograms to obtain the final displacement velocity model. The atmospheric correction is applied using two filtering approaches.

- Atmosphere Low Pass filter which takes into consideration the spatial arrangement of atmospheric fluctuations. It involves using a square window, where the smaller the window, the stronger will be the filter effect.
- Atmosphere Hi Pass filter refers to the temporal distribution of atmospheric variations. In this case, larger windows are more appropriate for correcting effects that exhibit limited changes over time.

The temporal coherence (TC) threshold is applied in order to use high-coherence pixels. Coherence values range from 0 to 1, where 0 indicates no correlation and 1 indicates perfect correlation. It filters out pixels with coherence values below the specified threshold, in this case (0.75). The final products from this stage are the same as the ones in the First Inversion, but this time with the atmospheric correction applied.

Geocoding

The last step of the Process is Geocoding, where data in slant range geometry are converted into ground range coordinates, creating georeferenced measurement points (MP). These MP are then classified as PS points when the following thresholds are satisfied: TC >0.75 and MuSigma >3.2. For these PS points, values of mean velocity for the whole period and the height displacement day by day are given.

During the Geocoding phase of the PS-DinSAR multi-stack process, MuSigma and Coherence thresholds are crucial for maintaining the reliability and accuracy of the final results. These parameters are employed to identify and preserve the most stable areas within the dataset (Fig.18). Detailed information about the parameters used in the Process (7.1).

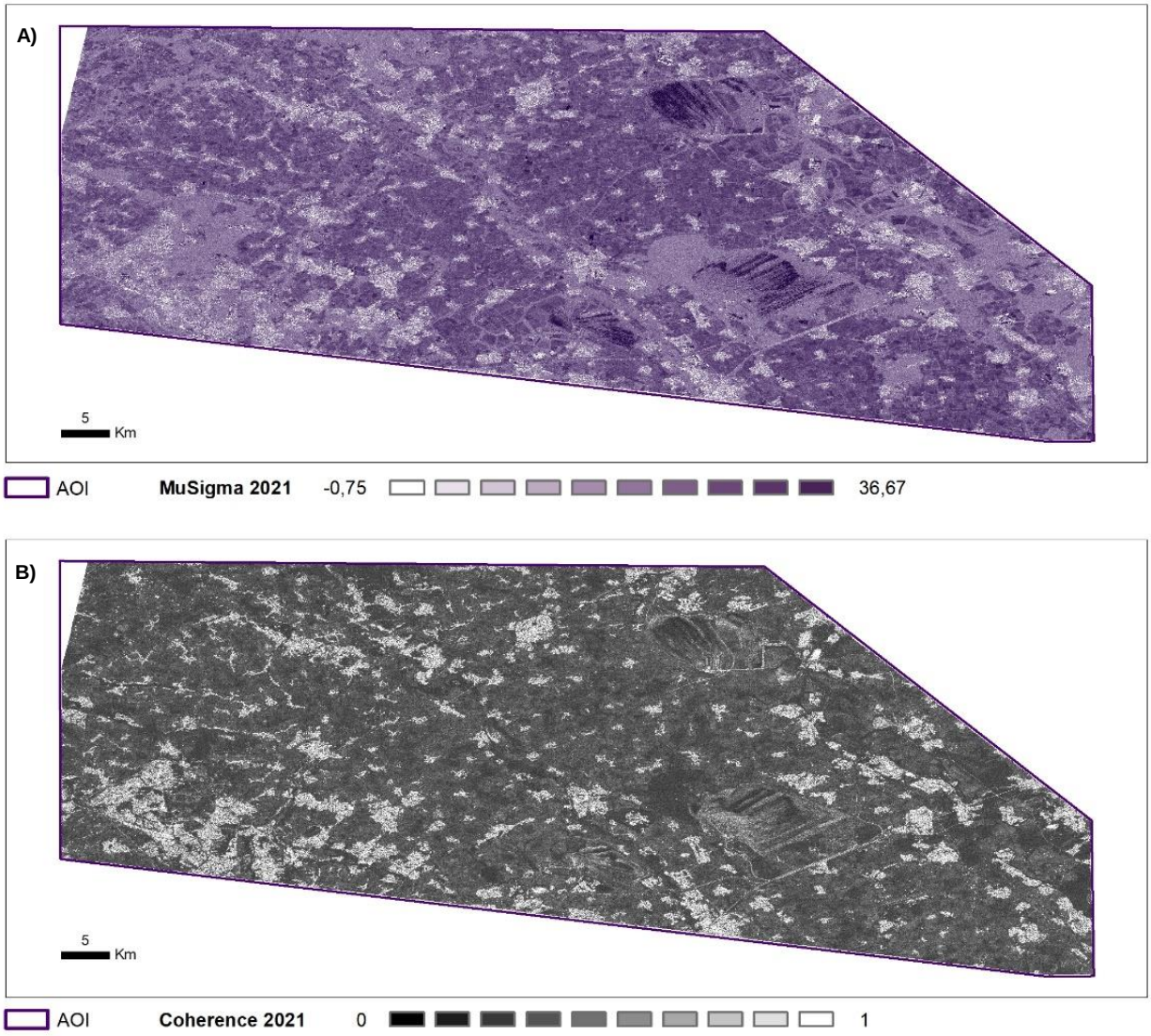

Fig.18 A) MuSigma and B) Coherence products obtained after the interferometric process for the year 2021.

3.2. Calibration

PS-DinSAR procedures detect the relative displacement between PS points and some stable points in the AOI used as a reference. Obtaining good reference points is not always possible, therefore, calibrating the obtained PS point set with respect to an external dataset of nearby GNSS stations is an interesting alternative (Casagli, 2019).
In this study, three GNSS stations were selected for calibration. After downloading their vertical position and velocity data for the year 2021, the data observed for each station was compared with that of the closest PS point. Then linear regression approaches were applied based on all three GNSS stations or one by one. The calibration procedure was restricted to the 2021 dataset due to the unavailability of data within EGMS and GMG for the following year, 2022.

3.3. Comparison between PS DinSAR results with EGMS and GMG

To compare the results obtained in this study (PS DinSAR multi-stack process) with those from EGMS and GMG, several steps were taken. Initially, Ortho products were exclusively downloaded for the year 2021 from EGMS and GMG because, as of 2022, they were not available. Subsequently, two new point layers were generated (EGMS and GMG) and compared with the 2021 PS point dataset obtained in this study.

It must be taken into account that both EGMS and GMG are distributed as grid point files, with a grid spacing of 500 x 500 meters. Therefore, the PS points obtained in this study were evenly distributed within this grid, calculating for each grid cell the average of the closest PS points. This redistribution process focused solely on the territory of Germany, omitting the AOI portion of the Netherlands for comparison with the GMG. Then, this comparison was made on a categorical basis, defining specific classes and velocity ranges (Table 2).

The final step involved creating confusion matrices to facilitate the comparison of EGMS and GMG products with the results of this analysis, using standard performance metrics.

Table 2 Classification of the velocity values inside of the grid.

Class	Velocity values
1	< -75
2	From -75 to -45
3	From -45 to -10
4	From -10 to 10
5	From 10 to 45
6	From 45 to 75
7	>75
9	No data

3.4. Monitoring 2022

After implementing the PS process for the base year 2021, a monitoring scenario was implemented, which consisted of re-processing the complete Sentinel-1 image stack plus a new subset of 5 new acquisitions. This monitoring process was repeated 6 times, considering a total of 30 images that covered a new one-year period (from January 2022 to December 2022). Therefore, each iteration represented a monitoring period of 2 months.

For each iteration, the Edit Connection Graph tool in SARscape was employed, which helped to modify the already existing Connection Graph by adding five more images. The remaining of the interferometric process followed the same steps mentioned above. In fact, all parameters that were initially implemented and subsequently fine-tuned in the prior phase were systematically replicated within each monitoring iteration. For this, the

auxiliary file was automatically updated after the execution of each monitoring period. The last monitoring period contained the final results of both years 2021 and 2022. This result is a 'super' shapefile that presents the updated PS points for the whole period and is analysed in the results section.

3.5. Trend Change (TI) and Acceleration Indicators (AcI)

Vertical displacement trends can vary in time, anticipating failure or collapse events that can have potentially disastrous consequences(Grebby et al., 2021). The detection of changes in the vertical displacement time series can be used to forecast these events. In particular, changes in the displacement trend can be approached as well as acceleration processes.

With this aim, the methodology proposed by the companyDARES, (2022) was implemented. First, the trend change indicator (TI) was calculated, this indicator evaluated change points along the time series highlighting the points were a change was observed and the new displacement trend had a slope increment with the previous one of >15º. Next, the acceleration indicator (AcI) was implemented, by fitting a second-order regression to the temporal trend and selecting points where the acceleration coefficient exceeded 70 cm/year (~2 mm/day). These two indicators were implemented in Python, utilizing libraries such as geopandas, numpy, and pandas (further information in 7.3). Subsequently, results were analyzed and interpreted in Excel and ArcMap.

3.5.1. Trend Change Index Mapping

The Trend Indicator (TI) was computed as follows: Initially, seven temporal ranges were defined, each spanning a two-month interval and consisting of five images. The first temporal range comprises only December 2021, serving as a connection point to the subsequent ranges, named M1 (Monitoring 1) through M6 (Monitoring 6). For each of these ranges a linear regression was fitted, and the slope, R-squared (R^2) value, and absolute slope angle were calculated. Then, the slope change between two consecutive ranges was determined, and the result was converted into degrees. Finally, two conditions were established: one for $R^2 > 0.8$ and another for the slope difference > 15°. The identification of areas experiencing changes in velocity, whether it's an increase or decrease, relies on two criteria: the R^2 values for both regressions must be higher than 0.8, and the angular difference between the two regression lines should be greater than 15 degrees. The PS points were classified into was classified into seven ranges, according to the conditions of the TI (Table 3).

Table 3 Range classification of the PS points according to TI.

Class	Conditions R^2(>0.8) and Slope (>15°) from M1 to M6	Number of PS points	Range classification of PS points
0	No conditions were met	186.678	Stable
1	1	40.851	Very Low
2	2	7.385	Low
3	3	2.714	Moderate
4	4	1.126	High
5	5	330	Very High
6	All conditions in all ranges were met	47	Extreme
TOTAL PS points: 239.131			

3.5.2. Acceleration Index Mapping

The AcI was divided into two periods Period 1 encompassed 2021 year, and Period 2 2022 year. The primary focus of the calculations was on Period 2, which was further divided into 6 individual ranges, as in the TI indicator (from M1 to M6). This indicator employed a second-order regression, applied over the last ranges of the time series. To ensure accurate estimations, a minimum of four data samples is typically required. However, in this study, five samples were incorporated for a more robust analysis.
The final identification of AcI was linked to the goodness of fit of the second-order polynomial regression, typically $R^2 > 0.8$, and to an estimated acceleration coefficient of > 2mm/day. The acceleration coefficient was determined by subtracting the final displacement value from the first within each range and then dividing their time difference.

3.6. PS applicability in civil infrastructure monitoring

Open Street Map (OSM) serves as an open, cost-free geographic database that undergoes ongoing updates and is carefully maintained by a community of dedicated volunteers through collaborative initiatives. To further monitor the AOI and to evaluate the applicability of the implemented PSinSAR approach for civil infrastructure three OSM layers were downloaded from https://www.openstreetmap.org/. These layers corresponded to the autonomous communities of Limburg in the Netherlands, Dusseldorf and Koeln, situated in Germany

The layer of Dusseldorf and its corresponding shape files (Fig.19).

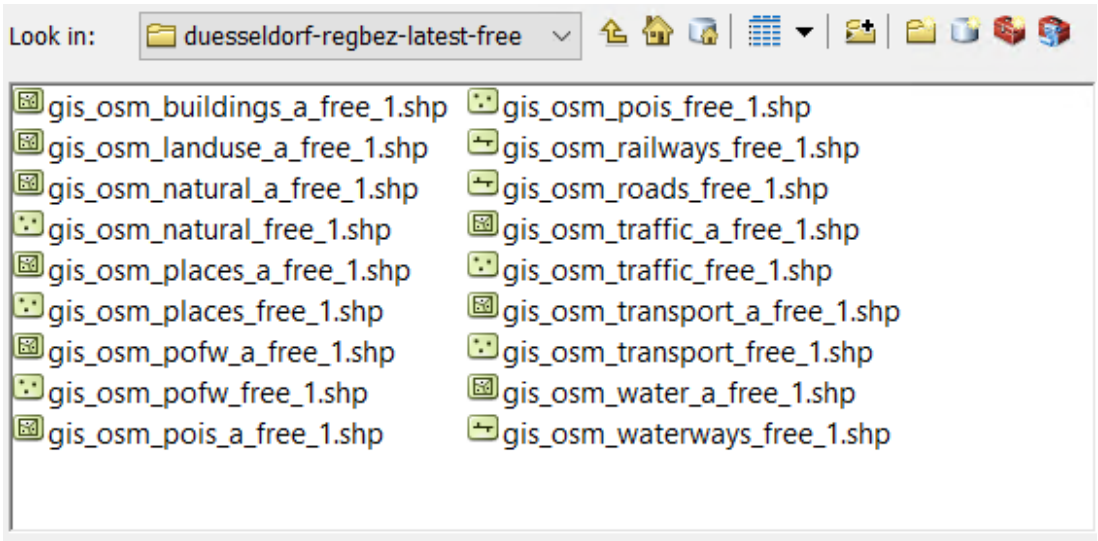

Fig. 19 OSM layer of the AOI.

The three layers were merged to obtain a single continuous OSM layer and different classes were assigned for the different civil infrastructures (Table 4).

Table 4 Classifications of the OSM layer

gis_osm_buildings_a_free_1.shp	
Buildings	Class = 1
gis_osm_pofw_a_free_1	
Churchs	Class = 1
gis_osm_traffic_a_free_1	
Car parking	Class = 2
gis_osm_pois _a_free_1	
Arts_centre, bakery, bank, bar, beauty_shop, beverages, bicycle_rental, bicycle_shop, bookshop, butcher, cafe, car_dealership, car_sharing, car_wash, castle, chalet, chemist, cinema, clinic, clothes, community_centre, computer_shop, convenience, courthouse, dentist, department_store, doctors, fast_food, fire_station, florist, food_court, furniture_shop, greengrocer, guesthouse, hairdresser, hostel, hotel, jeweller, laundry, library, mall, mobile_phone_shop, motel, museum, nightclub, nursing_home, optician, outdoor_shop, pharmacy, police, post_office, prison, pub, public_building, restaurant, shoe_shop, sports_centre, sports_shop, stationery, supermarket, theatre, toilet, tourist_info, town_hall, toy_shop, travel_agent, veterinary	Class = 1
car_rental, pitch, track	Class = 2
Archaeological, artwork, attraction, bench, biergarten, camera_surveillance, college, comms_tower, doityourself, fountain, garden_centre, graveyard, hospital, kindergarten, kiosk, market_place, memorial, monument, observation_tower, playground, recycling, recycling_clothes, recycling_glass, recycling_metal, recycling_paper, ruins, school, shelter, stadium, theme_park, tower, university, viewpoint, wastewater_plant, water_mill, water_tower, water_well, water_works, wayside_cross, wayside_shrine, windmill, zoo	Class = 3
camp_site, caravan_site, dog_park, golf_course, park, picnic_site	Class = 4
water, swimming_pool	Class = 5
gis_osm_transport_a_free_1	
airfield, airport	Class = 6
apron	Class = 7
bus_station	Class = 8
helipad	Class = 9
taxi	Class = 10
Gis_osm_Landuse_a_free_1	
allotments	Class = 101
commercial	Class = 103
farmland	Class = 104
farmyard	Class = 105
forest	Class = 106
grass	Class = 107
heath	Class = 108
industrial	Class = 109
meadow	Class = 110
military	Class = 111
nature_reserve	Class = 112
orchard	Class = 113
park	Class = 114
quarry	Class = 115
recreation_ground	Class = 116
residential	Class = 117
retail	Class = 118
scrub	Class = 119
vineyard	Class = 120
gis_osm_roads _a_free_1	
Railway	Class = 50
Trunk	Class = 51

Motorway	Class = 52
Primary	Class = 53
Secondary	Class = 54
Tertiary	Class = 55
Residential Road	Class = 56
Living Street	Class = 57
Service	Class = 58
Track	Class = 59
Rest	
Surrounding traffic network	Class = 121
Surrounding urban areas	Class = 122

The majority of PS points are concentrated within specific zones, including buildings (3.9%), residential areas (9.1%), residential roads (1.1%), and industrial areas (1.1%). Nevertheless, these areas represent a relatively small portion of the entire area of interest (AOI). The AOI is primarily dominated by extensive farmlands (49%), with forested areas accounting for 9.4%, residential regions at 9.1%, and quarries covering 5.1% of the land. The OSM classification also highlights open-pit mines in red, and this classification is crucial for interpreting PS points, especially those located in particularly sensitive areas (Fig.20), (Table 5).

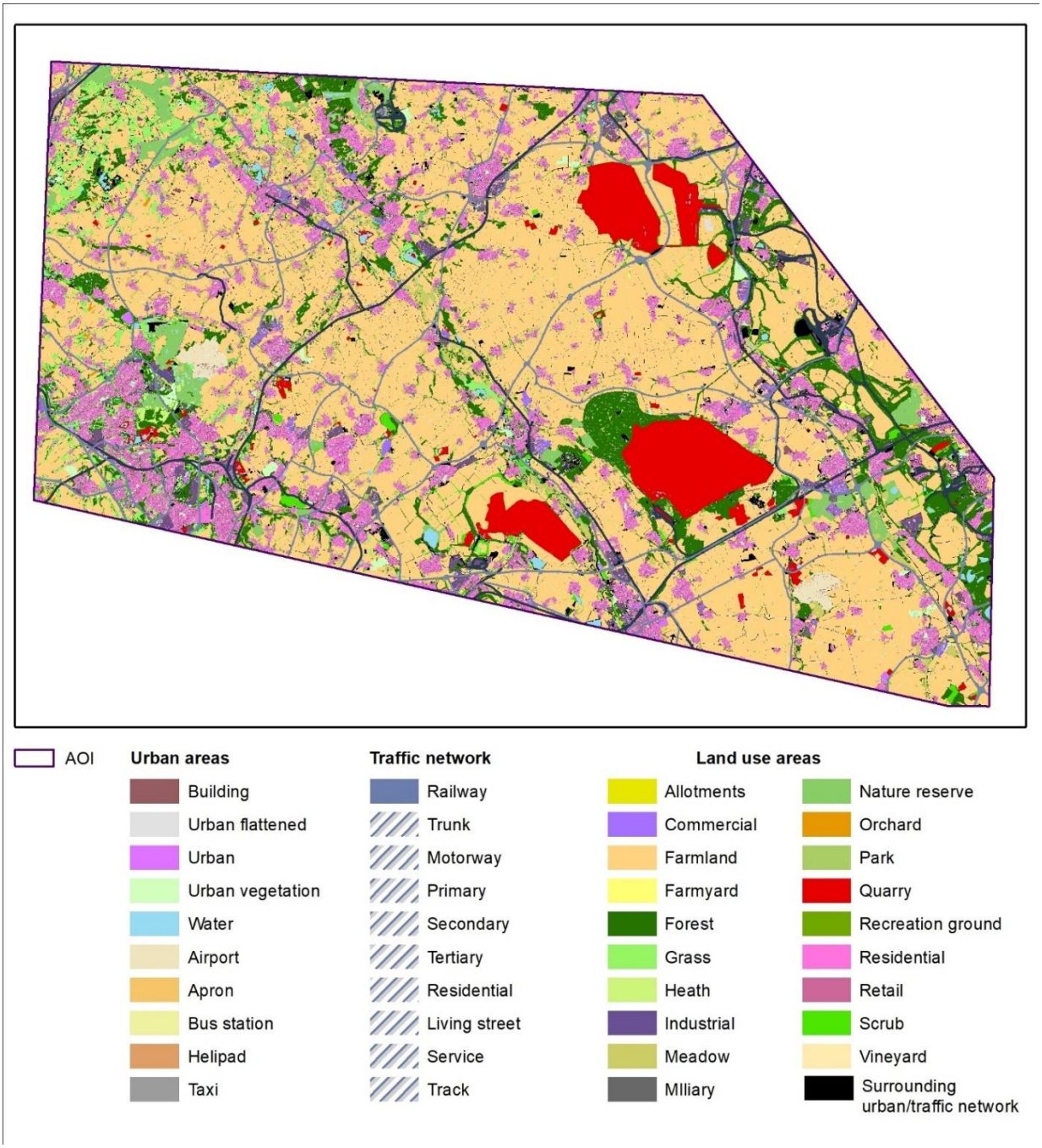

Fig. 20 Land use map for the AOI obtained from OSM data

Table 5 Distribution of PS points according to OSM Land Use

CLASS	Description	Area (km²)	%	Nº PS points		CLASS	Description	Area (km²)	%	Nº PS points
1	Building	84.87	3.9	87512		101	Allotments	1.20	0.1	24
2	Urban flattened	12.16	0.6	2386		103	Commercial	12.11	0.6	4508

3	Urban	14.02	0.6	2953		104	Farmland	1056.97	49.0	1588
4	Urban vegetation	11.80	0.5	312		105	Farmyard	8.14	0.4	1198
5	Water	19.27	0.9	181		106	Forest	202.49	9.4	828
6	Airport	10.99	0.5	600		107	Grass	65.22	3.0	1053
7	Apron	0.05	0.0	72		108	Heath	2.61	0.1	5
8	Bus station	0.01	0.0	10		109	Industrial	24.54	1.1	10019
9	Helipad	0.00	0.0	0		110	Meadow	87.52	4.1	727
10	Taxi	0.00	0.0	0		111	MIliary	1.23	0.1	233
50	Railway	3.28	0.2	1222		112	Nature reserve	41.42	1.9	89
51	Trunk	1.77	0.1	220		113	Orchard	3.24	0.2	19
52	Motorway	6.73	0.3	786		114	Park	0.05	0.0	8
53	Primary	4.24	0.2	481		115	Quarry	110.10	5.1	1501
54	Secondary	9.35	0.4	1977		116	Recreation ground	0.72	0.0	40
55	Tertiary	9.56	0.4	2646		117	Residential	197.42	9.1	90410
56	Residential Road	24.53	1.1	13751		118	Retail	1.23	0.1	788
57	Living street	2.85	0.1	2047		119	Scrub	21.31	1.0	164
58	Service	11.01	0.5	4508		120	Vineyard	0.17	0.0	1
59	Track	31.81	1.5	349		121	Surrounding traffic network	25.164	1.2	1579
						122	Surrounding urban areas	37.746	1.7	2336
							TOTAL	**2158.91**	**100**	**239131**

4. Results

4.1. PS-DinSAR

The ultimate output of PS-DinSAR multi-stack processing consists of a set of PS points along with ground displacement velocities in mm/year. In this case, a clear concentric pattern characterized by negative values was observed in the southern and southeastern regions of the Hambach mine (Fig. 21). This trend was particularly marked in the nearby urban areas, with some points achieving alarming subsidence rates higher than -95 mm/year. Instead, a moderate subsidence (-55/-45 mm/year) was observed in the eastern part of the AOI.

The southwestern and northeastern parts of the scene presented slightly positive values (5/25mm/year) and possible soil heave or uplift processes. The extreme (maximum) values observed for 2021 are 136 mm/year on the positive side, indicating strong soil heave phenomena and, on the negative side, a subsidence value of -137 mm/year. The average velocity value across the entire scene registers at -2.73 mm/year (Fig. 21), yet this average value is meaningless.

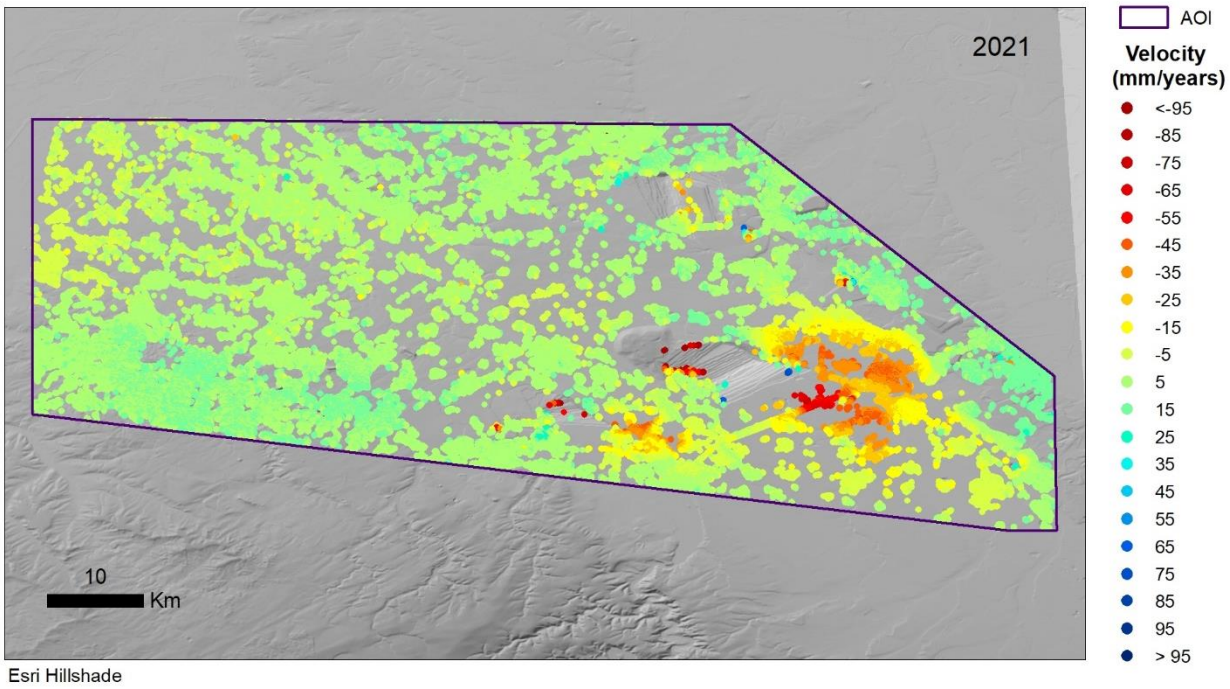

Fig. 21 PS point set obtained after the PS-DinSAR muti-stack process for 2021. Colours represent vertical velocity in mm/year.

The histogram displayed in Figure 22 exhibits a bimodal distribution with two distinct peaks. The initial peak covers displacement data falling within the range of 49 to 39 mm/year, while the second and larger peak encompasses data within the 36-34 mm/year to 10-12 mm/year range.

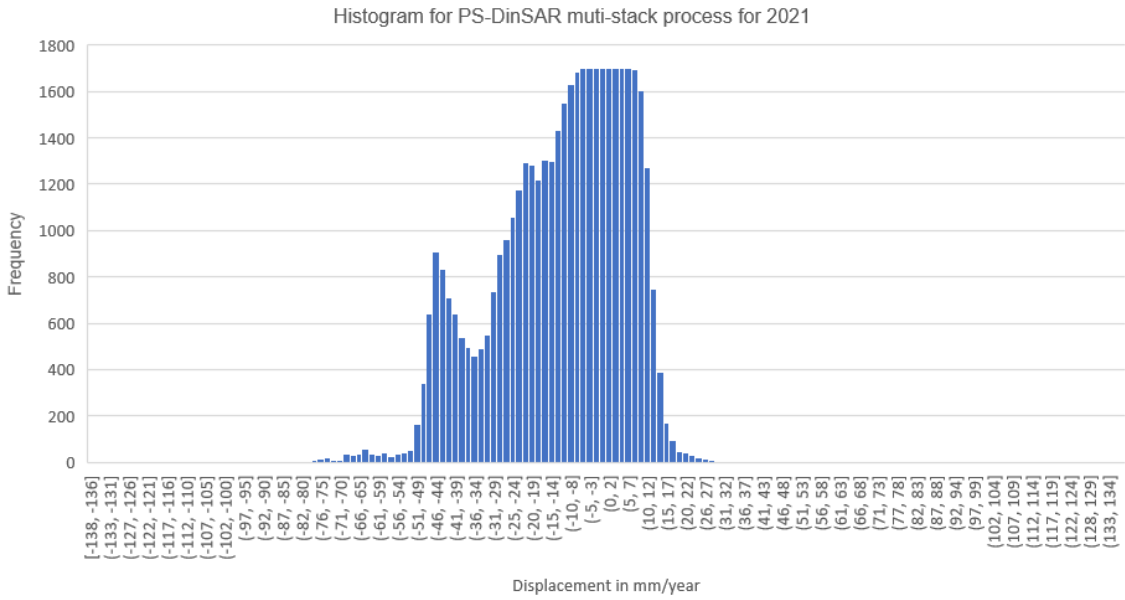

Fig.22 Histogram for PS-DinSAR multi-stack process for 2021

4.2. Calibration

The calibration based on the available GNSS stations provided poor results independently of the calibration data used as a reference. Fig. 23 A reveals that when using all three GNSS stations, the entire AOI changed dramatically its subsidence pattern, taking very stable values. Fig. 23 B shows the results obtained when using only SEL2 and TIT2 stations but with similar results. Fig. 23 C also shows poor results based on SEL2 and KERK stations. On the contrary, Fig. 23 D, based on TIT2 and KERK stations, shows an exaggerated subsidence pattern with strong deformations in areas with no prior subsidence history. Finally, using only one station, SEL2, the best calibration results were obtained (Fig. 23 E), but still, results seem to worsen those obtained without calibration. Although this represents a single GNSS point and might be deemed insufficient for calibration, a more comprehensive assessment of this station has been undertaken. When comparing the velocity values of this station to those of point PS, this is done at intervals of 6 days to align with the availability of Sentinel-1 imagery. Regrettably, the velocity correlation between these two points does not meet the required standards, and consequently, it is excluded from the calibration process at this juncture (Fig 23F).

All these calibration attempts were made by fitting a linear regression between the mean velocity values obtained for 2021 in the GNSS stations and the closest PS point. More detailed information, in 7.3.

In summary, none of the GNSS stations demonstrated the desired accuracy required for the calibration of PS points, resulting in an unsuccessful calibration process.

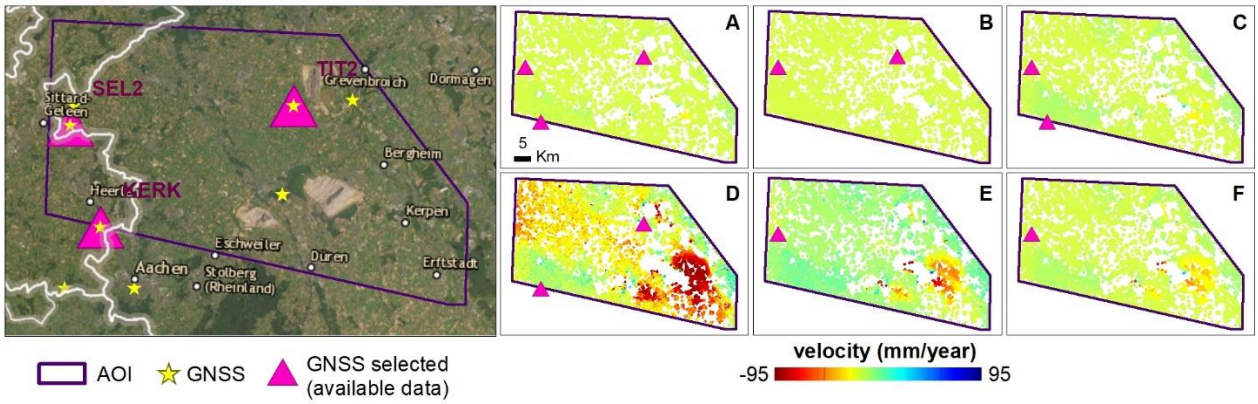

Fig. 23 Vertical velocities of PS points after the calibration performed by different GNSS stations (purple triangles). Green represents stable points, yellow-red subsidence and blue soil heave.

As explained, SEL2 was the GNSS station providing the more precise calibration results. However, taking a closer look at the velocity dataset of this GNSS station and its closest PS point (Fig 24), a notable discrepancy was observed, especially a strong multitemporal variability. Therefore, calibration was deemed unsuccessful and the remaining of the analysis was made with uncalibrated PS deformation data obtained in the previous step.

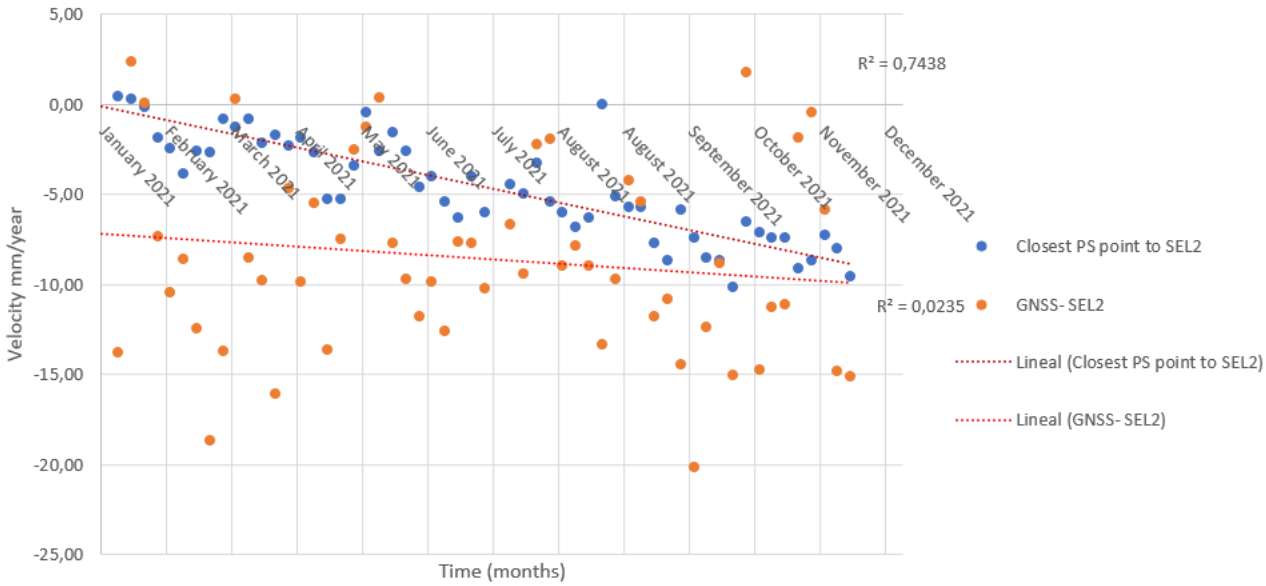

Fig. 24 Multitemporal representation of vertical velocity observed at SEL2 GNSS station and its closest PS point.

4.3. Comparison with EGMS and GMG

The comparison of the vertical deformations obtained in this study with the EGMS and GMG products demonstrated a reasonable coincidence. Figure 25 A presents the data in its original form, illustrating variations in PS density across the 500x500m grid cells.

In contrast, Figure 25 B illustrates the redistribution of PS points in the grid explained in section 3.3.

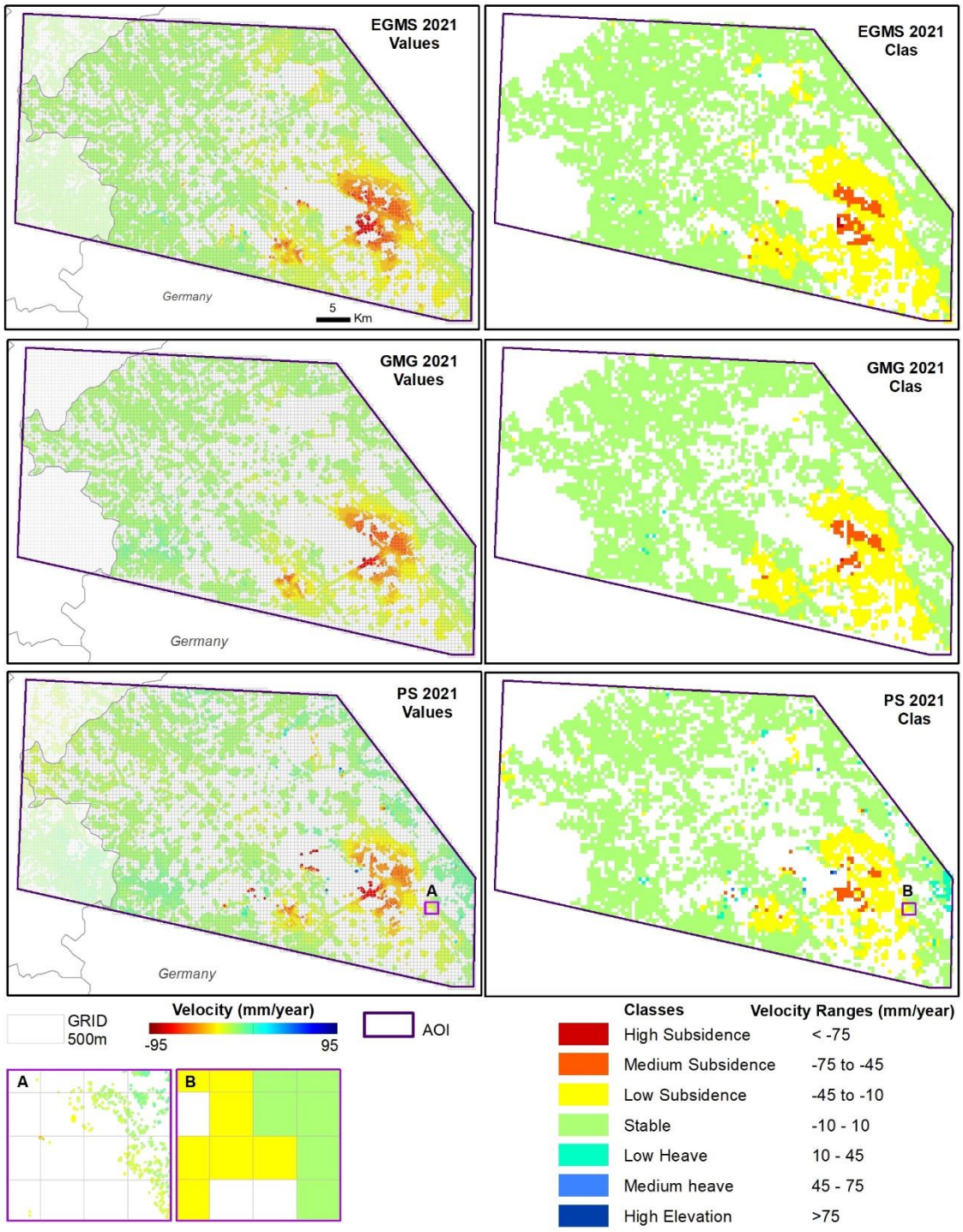

Fig. 25 PS velocity classification of the subset of the 2021 year against EGMS and GMG.

In the analysis, the model's performance in classifying the different deformation categories was evaluated using various metrics obtained from confusion matrices. First, the comparison with the EGMS showed high User's Accuracies (True Positive Rate) for

the 'Stable', 'Low subsidence' and 'Medium subsidence' classes, indicating that the model correctly identified these, and had low commission errors. Conversely, the 'Low Elevation' class recorded the lowest User's Accuracy at 3.23%, indicating the model's struggle to identify instances of this class correctly. Regarding the Producer's Accuracy (True Negative Rate), the 'Low Elevation' class achieved 100%, indicating that all EGMS instances belonging to this class were correctly identified, and hence the omission error was null for this class. The 'Stable' class also had a high Producer's Accuracy, but low and medium subsidence classes only achieved intermediate values (68% and 54%, respectively) and 'High subsidence' instances were completely missed out with a Producer's Accuracy of 0%. There were no grid cells classified as medium or high elevation either in the EGMS or in the model implemented in this study. Altogether, the Overall Accuracy with EGMS was 91%. The count of PS points differs between EGMS and GMG, with EGMS displaying a higher number (Table 6).

The comparison with GMG (Table 7) shows rather similar values compared to EGMS (Table 6). The Overall Accuracy was 92% with rather high user's accuracies for stable, low and medium subsidence classes. The producer's accuracies were high for stable and low elevation classes and intermediate for low and medium subsidence, conversely, high subsidence cells were completely missed with a 0%.

In conclusion, the overall accuracy of the model was high, indicating that most predictions aligned well with the EGMS and GMG products. This high accuracy suggests that the final product obtained was reliable for its specified purpose.

Table 6 Confusion Matrix PS 2021 subset versus EGMS

Velocity Average 2021 (mm/year)		EGMS									
		High Subsidence	*Medium Subsidence*	*Low Subsidence*	*Stable*	*Low Heave*	*Medium Heave*	*High Heave*	TOTAL	User's acc. %	Commission error %
PS	*High Subsidence*	-							-	-	-
	Medium Subsidence	1000	9750	750					11500	84,78	15,22
	Low Subsidence		8250	127000	7250				142500	89,12	10,88
	Stable			58500	812500				871000	93,28	6,72
	Low Elevation			750	14250	500			15500	3,23	96,77
	Medium Elevation						-		-	-	-
	High Elevation							-	-	-	-
	TOTAL	1000	18000	187000	834000	500	-	-	1040500		
	Producer's acc. %	-	54,17	67,91	97,42	100	-	-			
	Omission error %	100	45,83	32,09	2,58	-	-	-			

Overall accuracy %	91,28

Table 7 Confusion Matrix PS 2021 subset versus GMG

Velocity Average 2021 (mm/year)		GMG									
		High Subsidence	*Medium Subsidence*	*Low Subsidence*	*Stable*	*Low Heave*	*Medium Heave*	*High Heave*	TOTAL	User's acc. %	Commission error %
PS	*High Subsidence*	-							-	-	-
	Medium Subsidence	250	6500	2250					9000	72,22	27,78
	Low Subsidence		8500	116000	11250				135750	85,45	14,55
	Stable			37000	769250				806250	95,41	4,59
	Low Elevation			750	13750	250			14750	1,69	98,31
	Medium Elevation						0		-	-	-
	High Elevation							0	-	-	-
	TOTAL	250	15000	156000	794250	250	-	-	965750		
	Producer's acc. %	-	43,33	74,36	96,85	100	-	-			
	Omission error %	100	56,67	25,64	3,15	-	-	-			

Overall accuracy %	92,36

4.4. Monitoring 2022

Fig.26 illustrates the multitemporal evolution of the PS -DInSAR multi-stack process for the period from January 2021 to December 2022. Notable changes were systematically observed in the northeastern part of the AOI. In 2021, the region displayed moderate subsidence, with rates ranging from -15 to -5 mm/year. Over time, the area transitioned into a relatively stable region, represented by the green colour indicating deformation rates between -5 and 5 mm/year.

In the northern part of the AOI, variations in velocities were noticeable throughout the monitoring phases, particularly around the northern mines of Garzweiler I/II at the beginning of 2021. However, from January to February 2022 (M1), the region exhibited stability, and then, towards the end of 2022, higher subsidence values were again evident, ranging from -25 to -35 mm/year.

Significant changes also occurred in the southern area, where a transition from relatively stable values (ranging from -5 to 5 mm/year) to soil heave rates of 25 to 35 mm/year was observed by the end of 2022.

Altogether, the most problematic area within the entire scene was the Hambach open-pit mine and its surroundings. This area was systematically characterized by high subsidence values, ranging from -45 to -35 mm/year, and, in some cases, exceeding -95 mm/year. These high subsidence rates were primarily situated in urban areas around the mine.

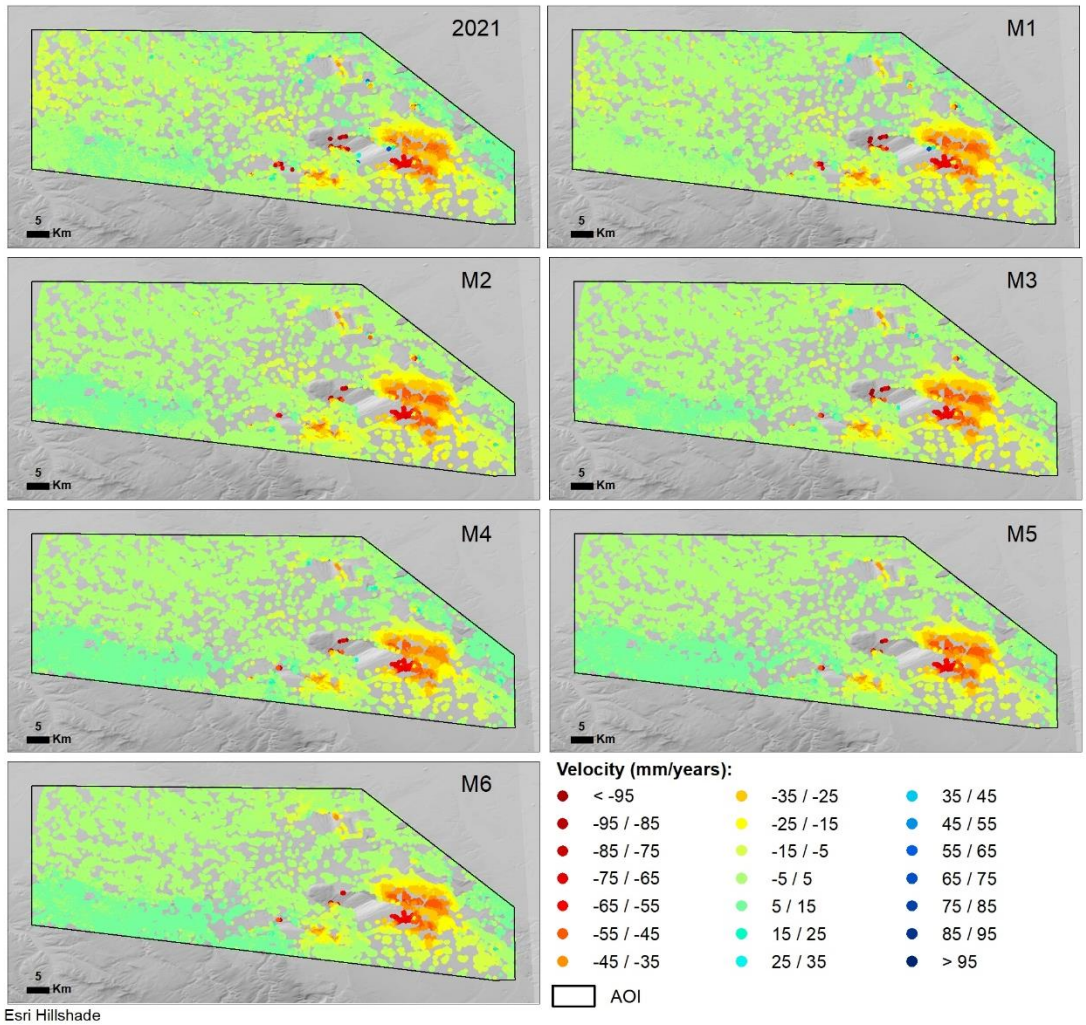

Fig. 26 Results of the base PS-DinSAR process for 2021, and the subsequent six monitoring sets for 2022.

The coherence value serves as a metric for evaluating the precision of the interferometric phase determination, where higher coherence values are indicative of increased accuracy in the interferogram generation. In any interferometric process, coherence typically improves as the analysed image is closer in time to the master image. Despite a longer time to the master image, the interferograms for 2022 exhibited a remarkable consistency. Most areas exhibited minimal changes and maintained stable coherence levels. As a result, it can be deduced that the 2022 interferograms maintained their reliability, even when considering an extended temporal baseline (Fig.27).

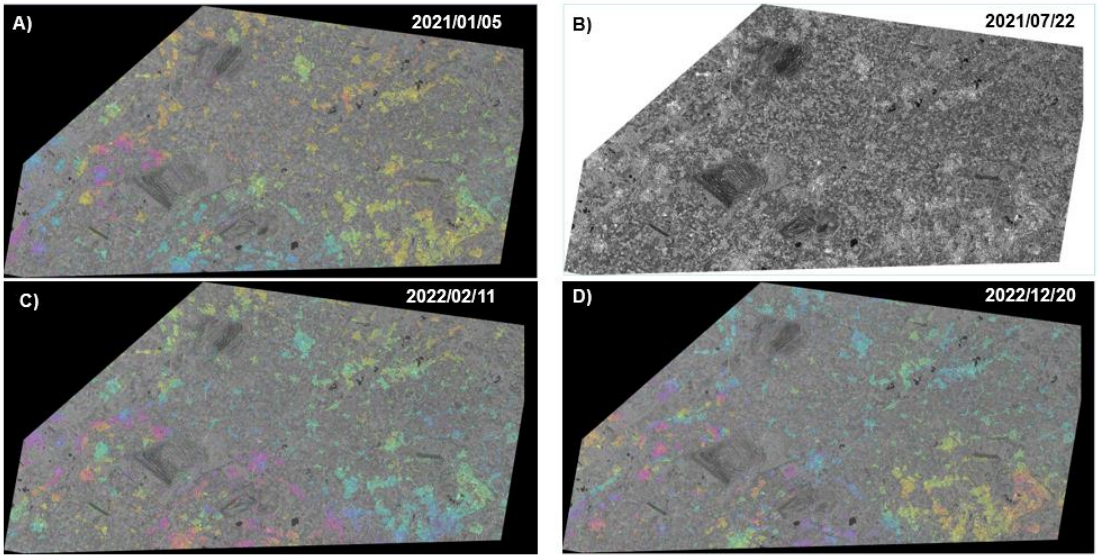

Fig.27 Temporal baseline's impact on the results' precision
A an interferogram from January 5, 2021, B an intensity image of the master from July 22, 2021, C an interferogram from February 11, 2022, and D the last interferogram of the 2022 dataset, from December 12.

The accumulated vertical displacement (in mm) with respect to the first scene revealed again the severe and rapid subsidence processes around the Hambach mine area, where a total subsidence of -250 mm was observed for December 2022 (Fig. 28).

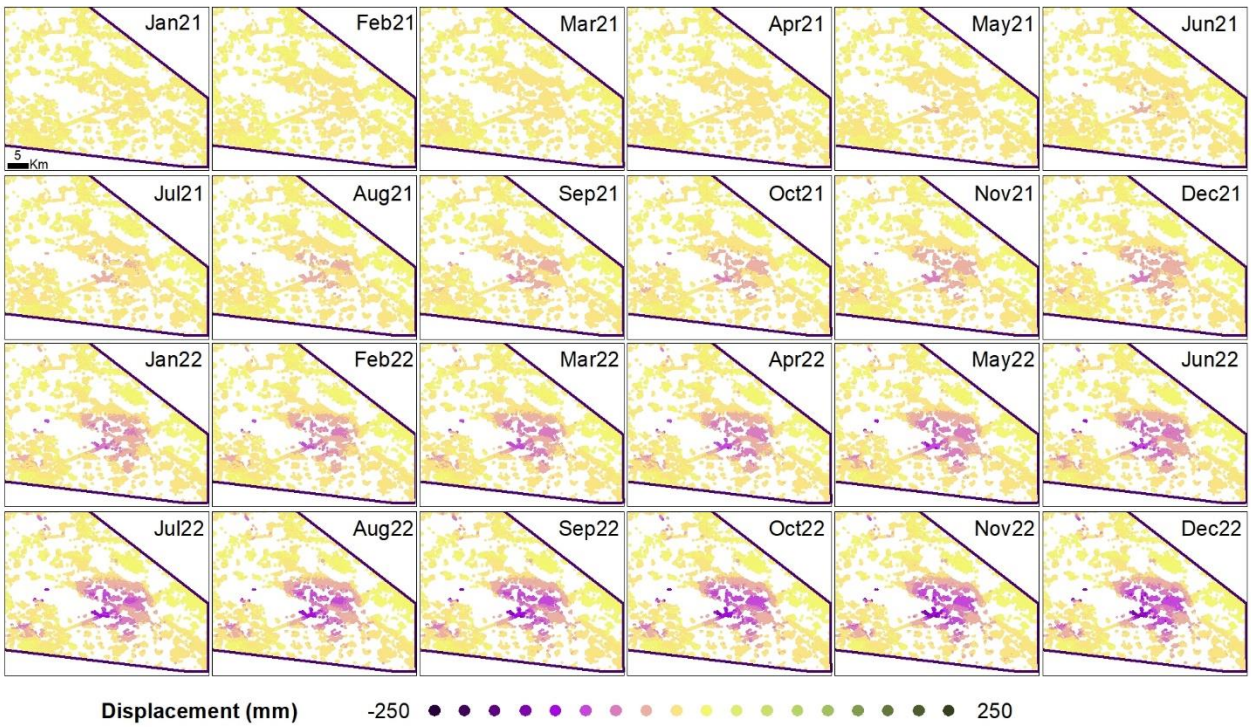

Fig. 28 Multitemporal evolution of the vertical displacement with respect to the first scene of the PS DinSAR multi-stack process.

Fig. 29 shows the deformation trend of a sample point in a subsidence area, demonstrating a strong alignment with the linear regression model, with an R^2>0.8, confirming the consistency of the subsidence process and the reliability of the results obtained through the PS InSAR process. This reliability is crucial for making accurate predictions and conducting further analyses, especially when assessing trend changes and acceleration processes in particularly sensitive areas such as infrastructures

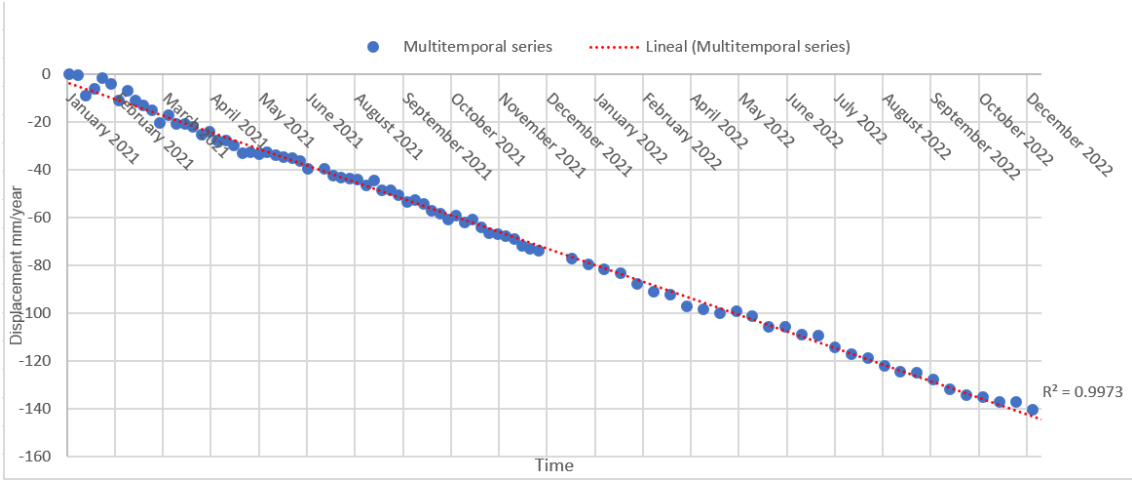

Fig. 29 Multitemporal vertical displacement results for a sample point of the PS- DinSAR process covering the period 2021-2022.

4.5. Trend Change and Acceleration indicators

Fig. 30, shows the trend change indicator, representing points with increasing velocity mainly in the southeastern part of the AOI, where the Hambach and Inden mines are located. In contrast, the rest of the scene presented a stable or very low trend variation.

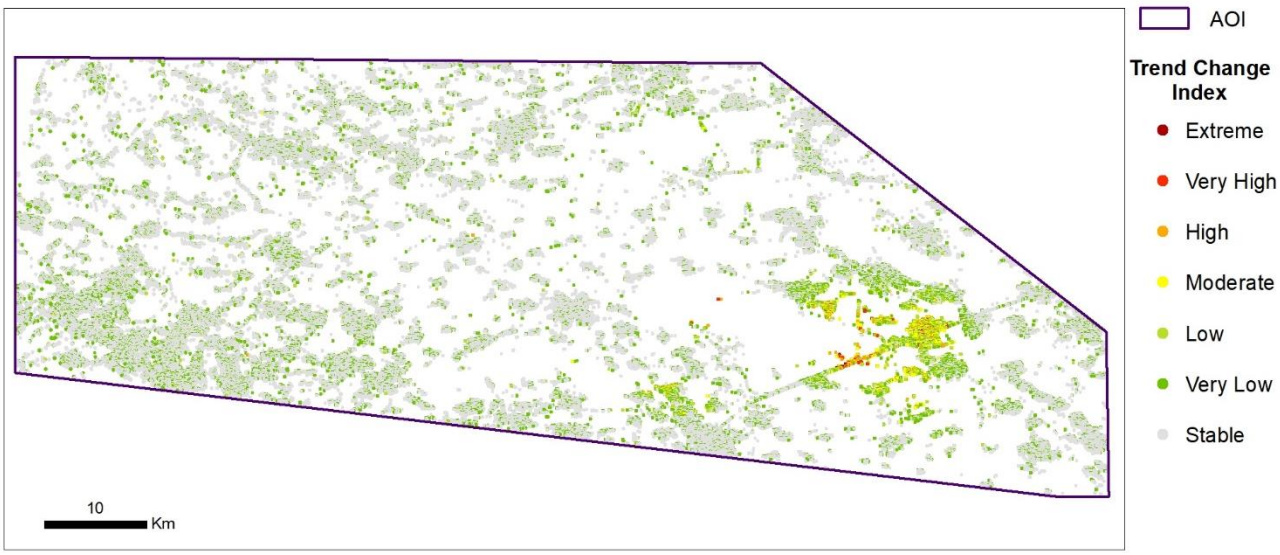

Fig. 30 Final results after the calculation of the TI

To emphasize the problematic regions within the final TI results, only class 5 (Very High) and class 6 (Extreme) points were taken into consideration for further analysis (Fig.31).

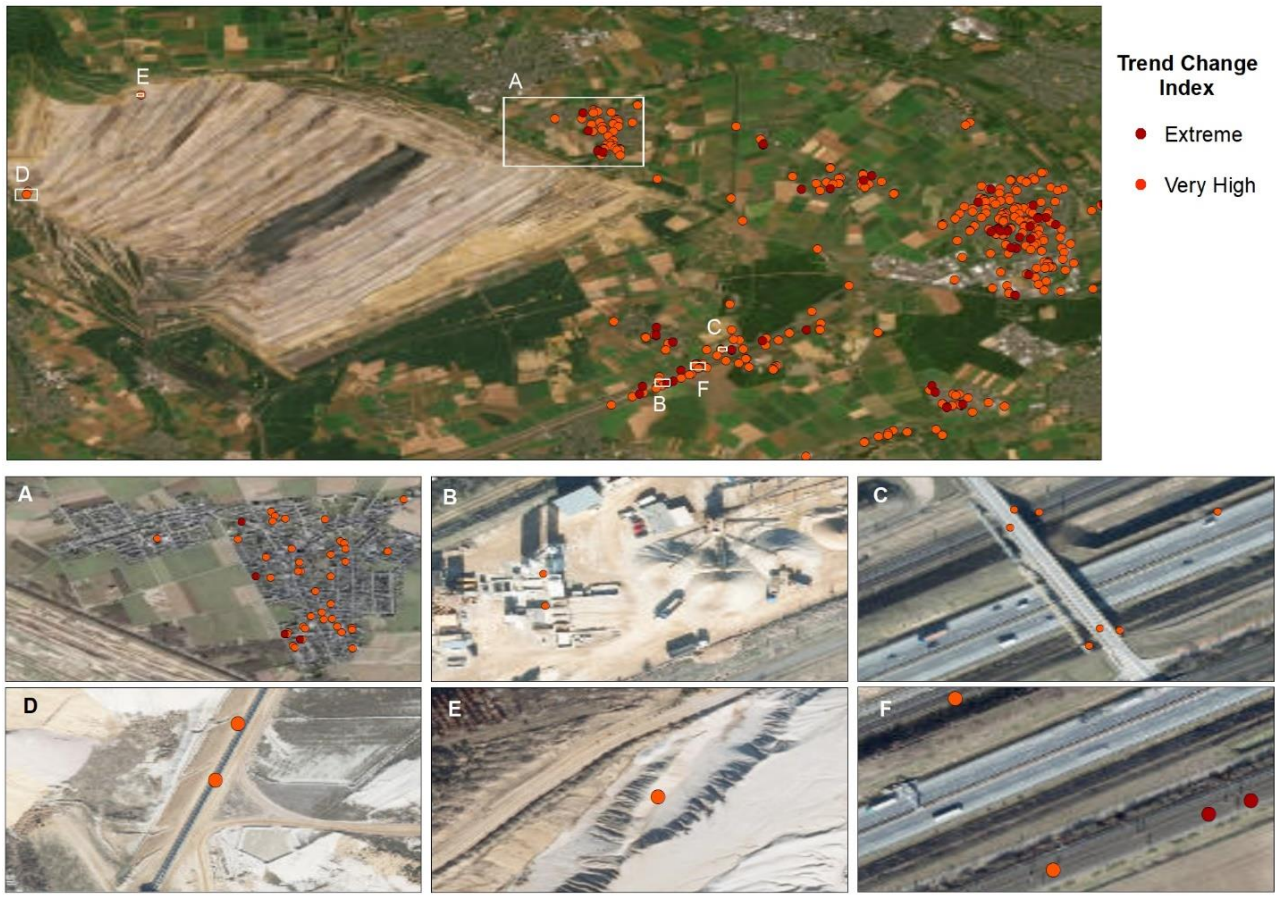

Fig. 31. Points highlighted as having extreme or very high trend changes in the Hambach mining area. A represents the towns of Giesendorf and Berrendorf, B is a mining facility around the mine, next to excavator machines, C corresponds to a bridge over the highway, D is a railway crossing the mine, E is a point in the mine slopes, and F another railway near the highway.

Fig. 32 represents the linear regressions fitted for each time range showing their R^2.

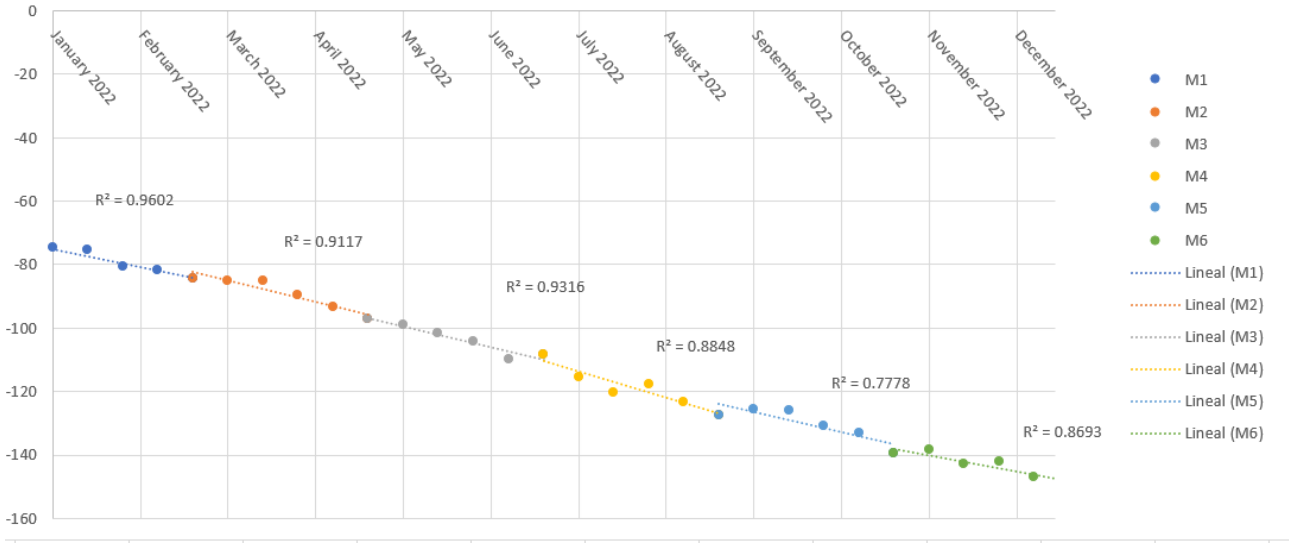

Fig.32 Displacement evolution of a singular PS point identified as a TI.

Fig.33 represents the final result of the AcI for the whole AOI, yielding only 4 points that met all the conditions.

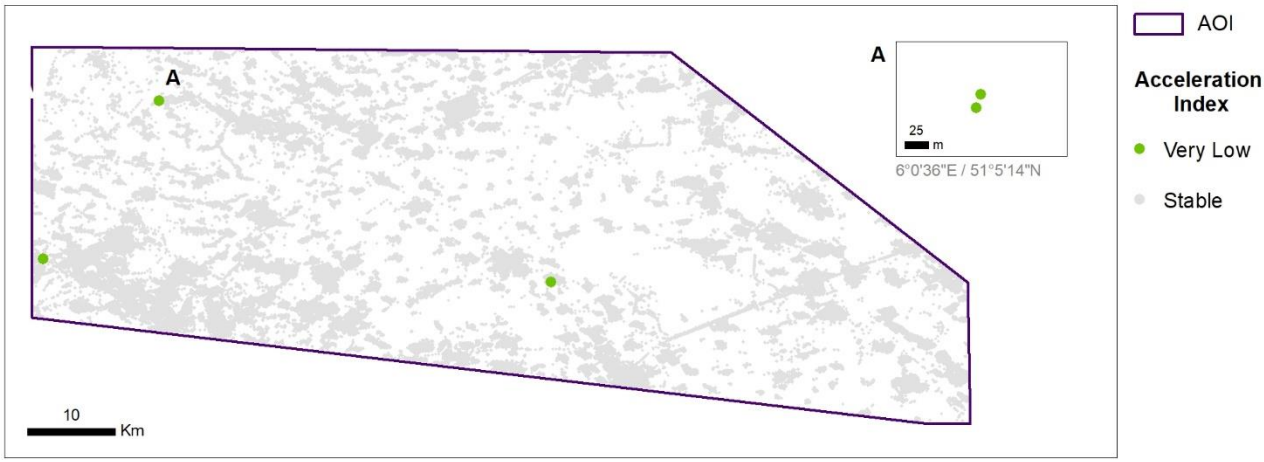

Fig. 33 Final results of the calculation of AcI

The four points identified by the AcI revealed acceleration processes in different time intervals: May-June 2022 (point B), September-October 2022 (one of the points in A) and November-December (point C and the second point in A) (Fig. 34).

Fig. 34 Acceleration Index in the AOI. Two points are situated in the town Haaren, next to the border with the Netherlands, B is the roof of a commercial centre in the Netherlands and C is situated in the town of Hambach, between the two open pit mines of Hambach and Inden.

Fig. 35 represents the increasing acceleration in the period of September- October 2022, marked in orange colour, for a singular PS point.

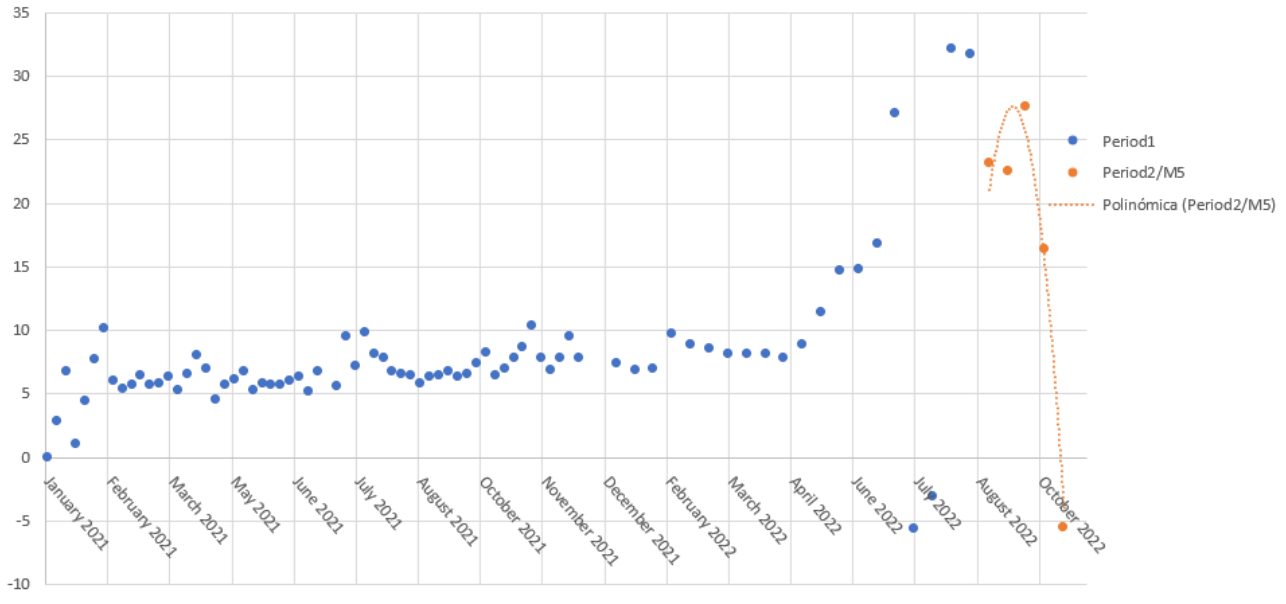

Fig. 35 Multitemporal evolution of the acceleration of a singular PS point

4.6. Civil infrastructure monitoring

The PS points exhibited their highest concentration in urban and residential settings, including buildings, service areas, residential streets, commercial and retail districts, and industrial zones. In contrast, lower PS point densities were observed in the transport network, particularly on secondary, tertiary, and railway roads, though some PS points were still identified in these areas. The hotspots are indicated in red colour in Fig. 36, reaching a maximum density of 2200, while areas devoid of PS points are represented in white.

Fig. 36. Density map of the PS points over an OSM layer.

Numerous PS points were detected over industrial areas and different objects of transport networks such as bridges, billboards along the trunk and metallic electric train poles instead of the actual roads or railways. As the study evaluated only vertical displacements, these PS points corresponded to the highest objects in the surroundings of the above-mentioned areas. Moreover, these PS points had mostly a high intensity in the Sentinel-1 images and this indicates a stable reflection of radar signals. Another reason for this high intensity might be the material of the objects where the PS points are detected, for example, smooth and metallic surfaces, tend to reflect radar waves effectively. In contrast, surfaces such as vegetation or soil, non-metallic materials, water and pavement roads presented low intensity, as is observed in the figures below (Fig. 37, Fig. 38, Fig. 39, Fig.40, Fig.41 and Fig. 42).

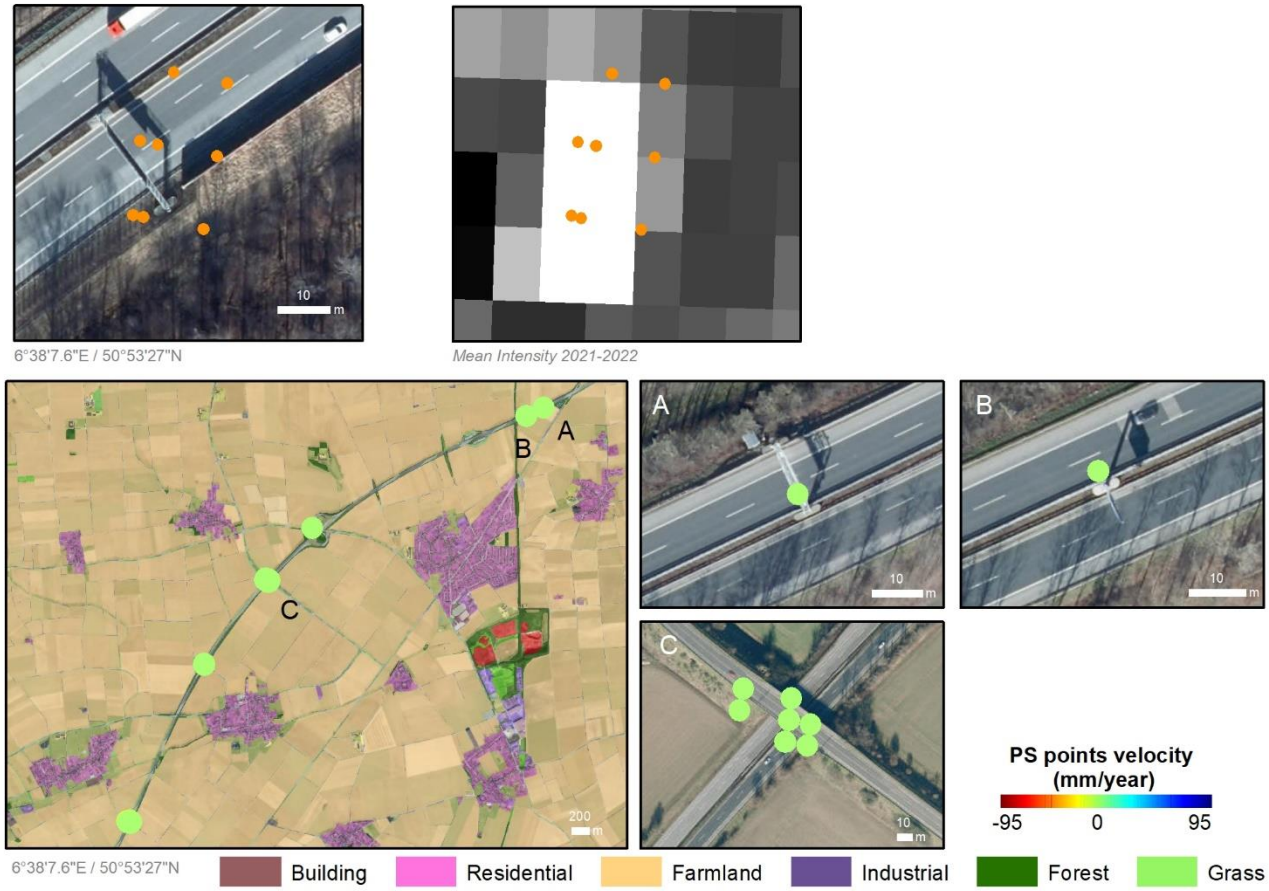

Fig. 37 PS points in elements of the transport network.

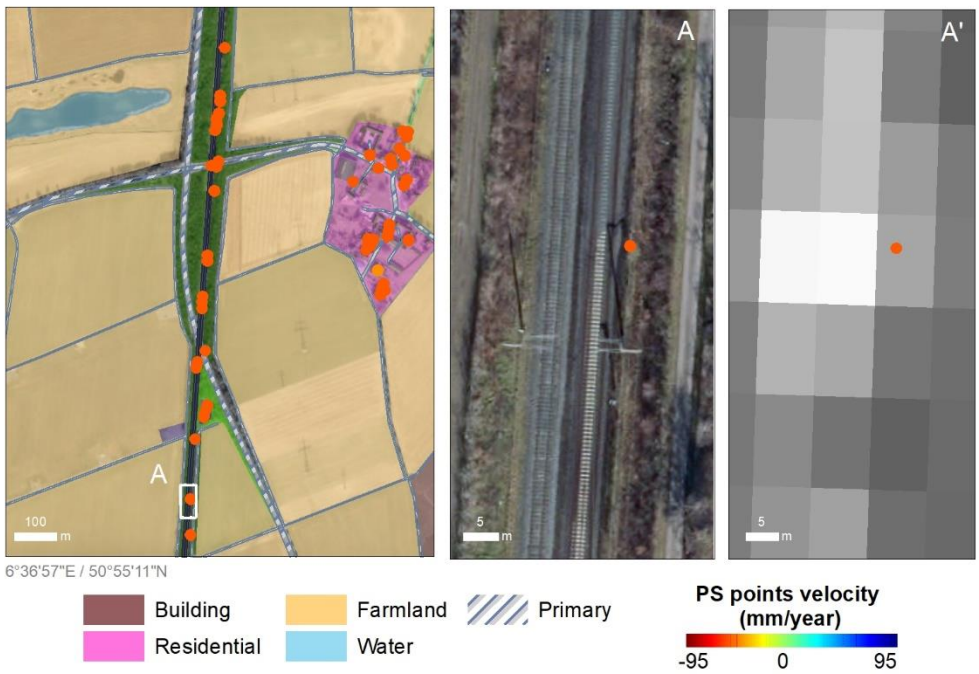

Fig.38 PS points detected in civil infrastructure over an OSM layer on the left and on the right PS points next to a railway along with its intensity image.

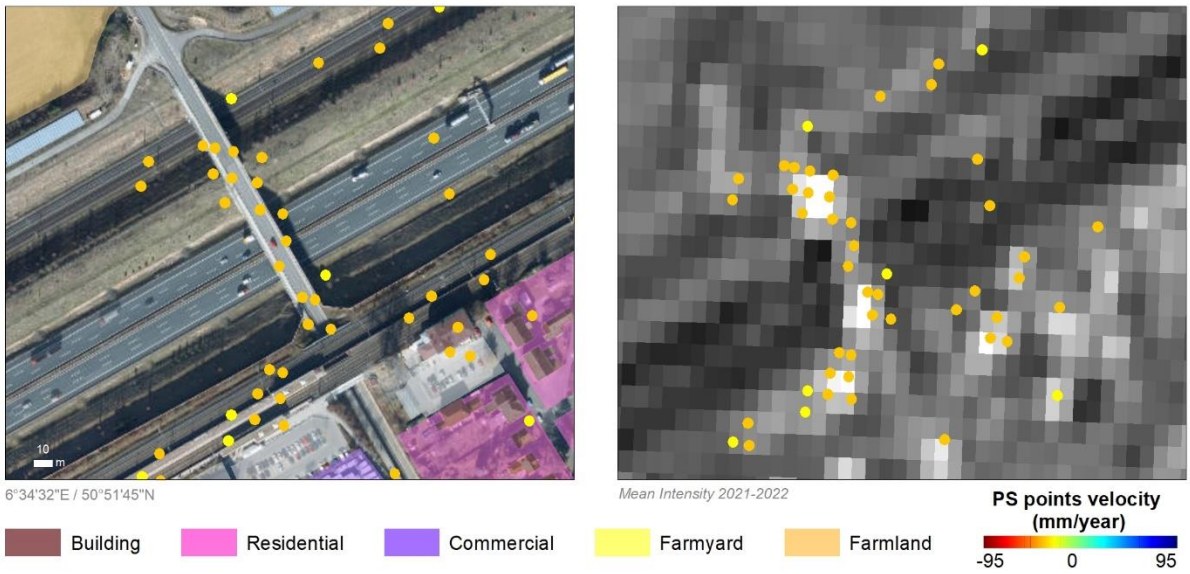

Fig. 39 PS points detected over a bridge with the OSM layer as background on the left and an intensity image on the right.

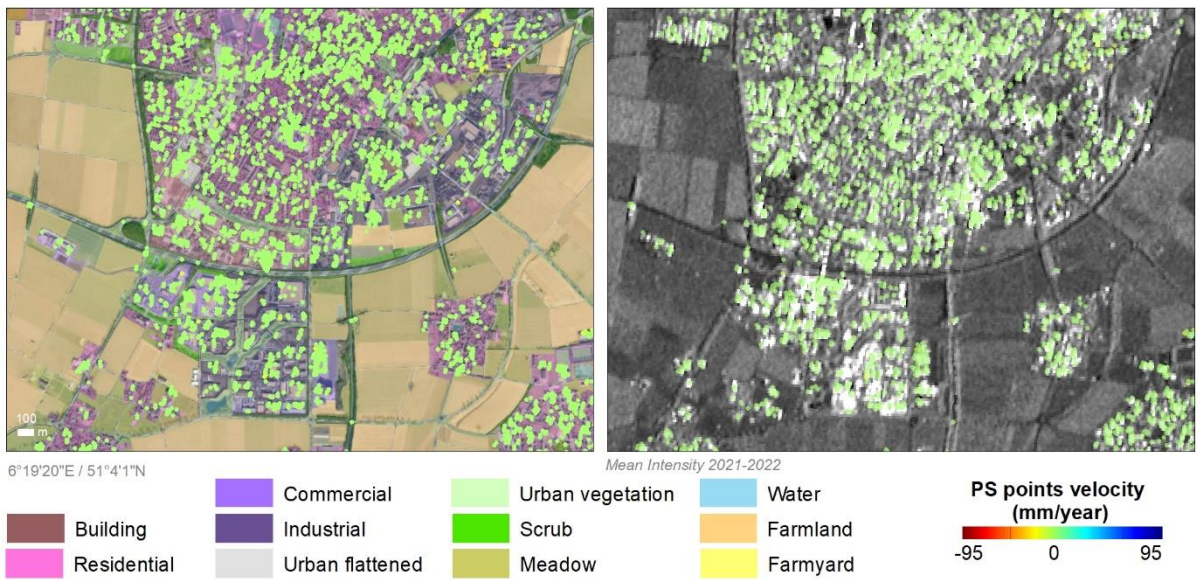

Fig. 40. PS points detected in urban areas represented over an OSM layer on the left and over an intensity image on the right.

Fig. 41. PS points detected over industrial areas represented over the OSM layer on the left and over an intensity image on the right.

Indeed, effective interferometric monitoring relies on the presence of PS points that typically occur on man-made objects. In situations where these points are scarce or non-existent, monitoring becomes challenging or even impossible. A clear example of this was observed in airports, where the density of monitoring points was relatively low (Fig. 42). However, even with a limited number of PS points, it might be possible to conduct monitoring activities, although with certain limitations.

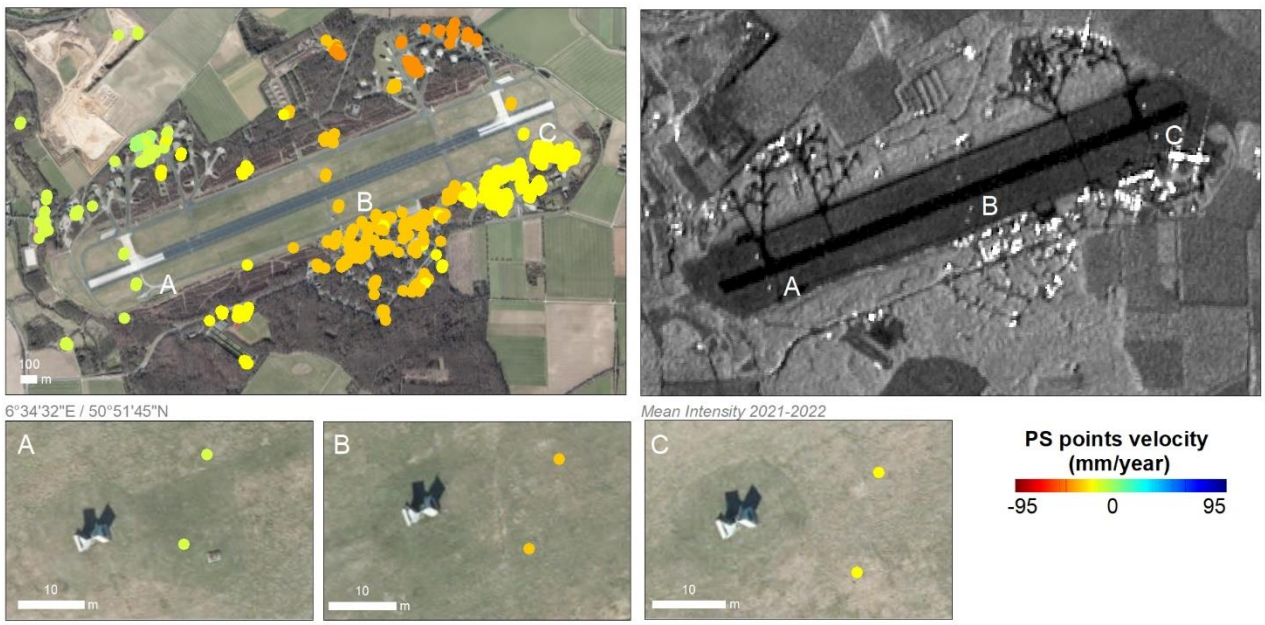

Fig. 42 Airport next to the Hambach mine on the left is represented by an orthophoto with the PS points and on the right the intensity image. A, B and C represent the PS points in the airport runway.

In general, inside the mine excavation areas, very few PS points were detected as these areas are in constant change and also represent mainly sediments and bare ground where the intensity might be low. Yet, in particular cases, PS points were found inside the Hambach open-pit mine, in particular in railways. In Fig. 43 some PS points are represented inside the mine, in objects that might be part of railways, poles or other elements like cargo trains (Fig.43).

A similar scenario was observed in the Inden mine (Fig. 43 C), where the PS points were denser in a network of metallic elements, probably some sort of construction materials inside the mine.

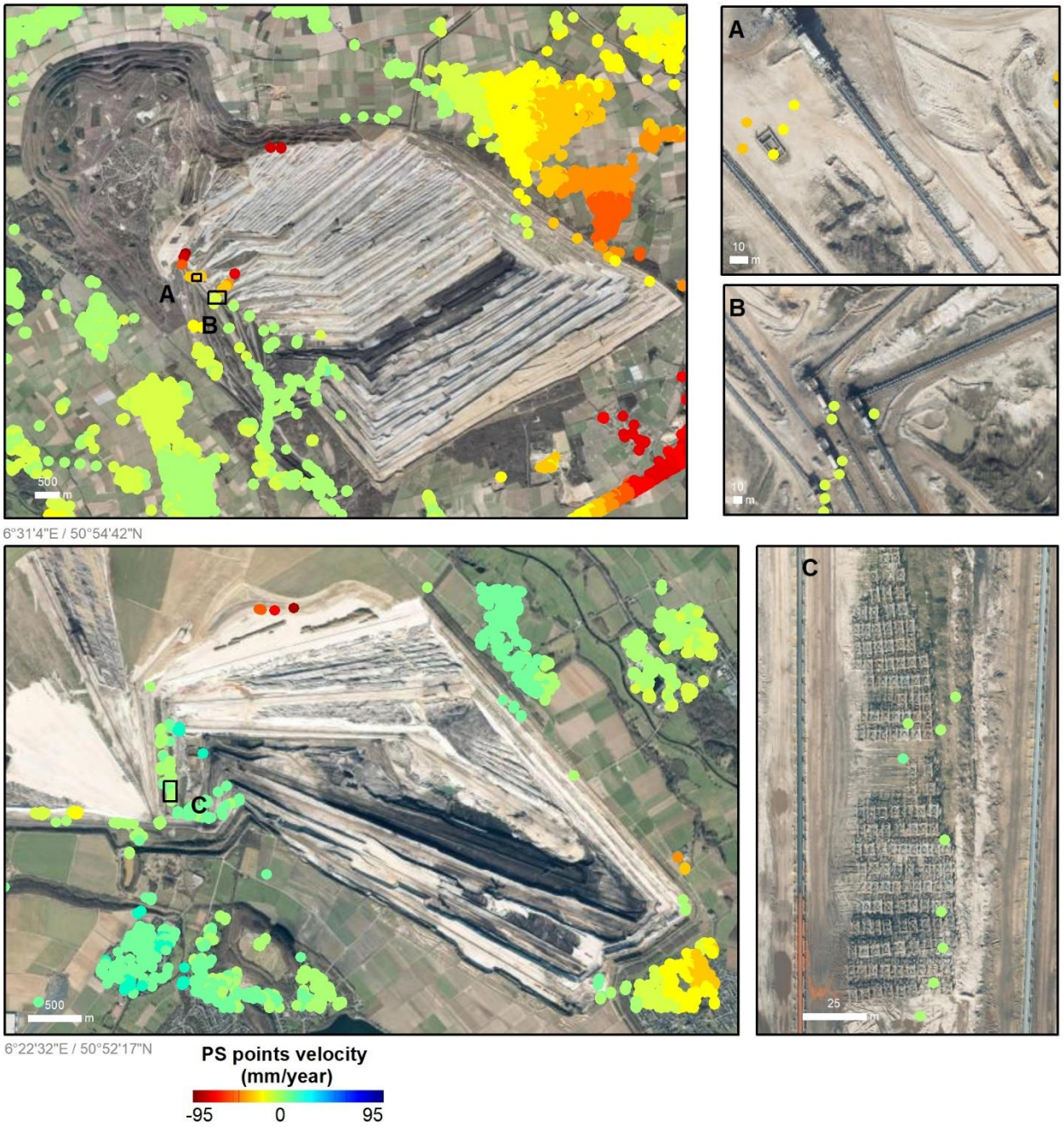

Fig.43 A and B present PS points detected in the surroundings of the open-pit mine Hambach and C represents the open-pit mine Inden and the PS points in its proximity.

There were very few PS points within sediment areas inside the mines, and the few ones discovered were located on consolidated materials originating from the mining operations (Fig.44).

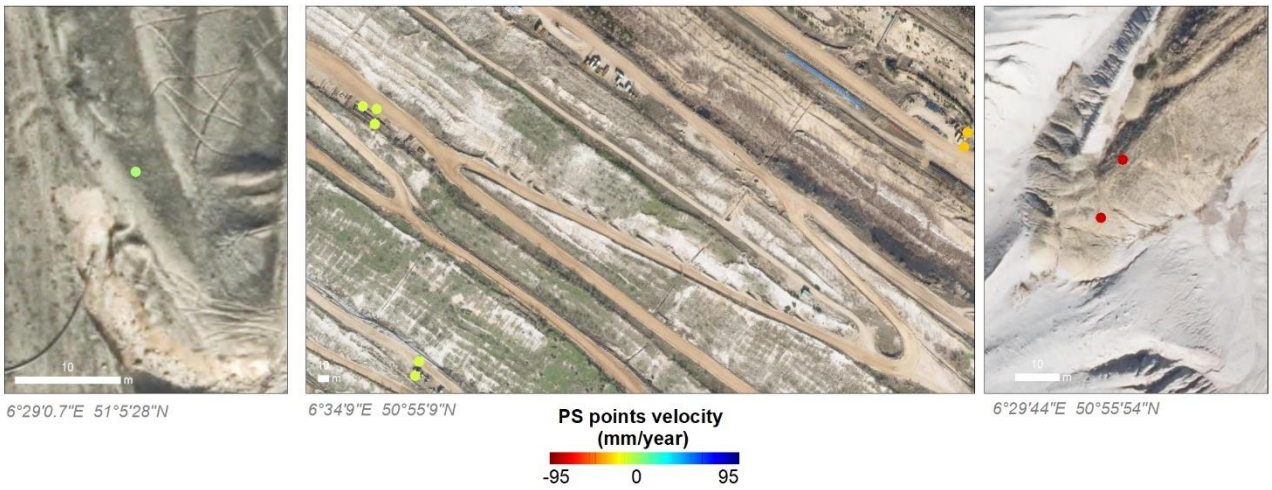

Fig.44 PS points on consolidated material inside the open-pit mine of Hambach

5. Conclusions

The multi-stack PS-DinSAR processing technique implemented in this study proved to be a valuable tool for analyzing Earth's surface deformation with remarkable millimeter-level accuracy.

By employing a multi-stack PS DinSAR procedure involving 58 S-1 images captured in 2021, each with a temporal gap of 6 days, the study facilitated an examination of ground displacements in and around the Hambach mine. Notably, the dataset for the year 2021 exhibited significant extremes, with a maximum value of 136 mm/year, corresponding to a soil heave or uplift phenomena, and a minimum value of -137 mm/year, representing subsidence. The areas where subsidence was detected in this study, generally coincided with areas where subsidence problems were already known, mostly in urban areas around the mine.

A calibration procedure was approached based on reference data from GNSS stations located within the AOI. However, the calibration results were unsatisfactory, indicating either a poor data quality of the available GNSS stations or an already accurate PS DinSAR process that was able to find good and stable ground control points.

Although EGMS and GMG data are generated at a national/international scale, and the work was conducted at a local scale, it was possible to compare both results. Both EGMS and GMG are verified, validated, and standardized data sets and thus provide an interesting reference for comparison. The evaluations performed showed a reasonable agreement with the results obtained here. For implementing comparisons like this in an operational context, it might be particularly limiting to obtain updated EGMS and GMG data, that in this case were not available for 2022.

A monitoring approach was implemented, that incrementally added S-1 observations to the PS DinSAR process. The approach led to a reduced processing time, since new acquisitions were integrated into an existing stack, and the most intensive computing processes were thus easened. In fact, the results obtained for 2021 and 2022 exhibited a minimal variance, thereby preserving temporal consistency and obtaining highly accurate outcomes.

In a future context, the challenge of preserving temporal coherence between the initial image and subsequent acquisitions may give rise to less precise results, and this should be a matter of forthcoming research.

This study also implemented an approach to detect points where deformation trends were changing or accelerating. This approach was based on TI and AcI indicators proposed by DARES, which were implemented in a Python script. The results obtained were satisfactory. The TI index served as a reliable indicator for detecting sudden shifts in ground speed trends, with several points identified in our specific case, around the hotspot area surrounding the mine. On the contrary, AcI produced fewer data points, and further investigation and research are necessary to fully understand this result.

Additional analysis is needed to progress on the trend change and acceleration indicators approach, ideally leading to a methodology that can successfully identify potential collapse points and even forecast their failure date.

This work evaluated the utility of the approach implemented for monitoring elements of the civil infrastructure. Based on OSM cartography, the geographical distribution of PS data from 2021 and 2022 were assessed. Numerous data points were identified in various settings, including bridges, railway systems (comprising metallic electric train poles) and their surroundings, as well as within residential, industrial, and commercial

zones (indicating the presence of structures like buildings and houses). This ensures the feasibility of effectively monitoring these areas with the PS DinSAR approach.

However, in cases such as airports and highways, obtaining PS points situated directly on the road or airport runaway surfaces was challenging. Instead, points were discerned close to these transportation networks. Additionally, within mining areas, data points were predominantly located within machinery zones, with fewer points dispersed in the actual mine sediments or excavation areas.

6. References

Álvarez Mozos, J. (2023). Teaching material for the subject Radar and LiDAR Remote Sensing. *Public University of Navarre, Pamplona (Spain).*

Blewitt, G., Hammond, W. C., & Kreemer, C. (2018). Harnessing the GPS Data Explosion for Interdisciplinary Science. *Eos, 99. https://doi.org/10.1029/2018EO104623*

Bogena, H., Kunkel, R., Schöbel, T., Schrey, H. P., & Wendland, F. (2005). Distributed modeling of groundwater recharge at the macroscale. *Ecological Modelling*, *187*(1 SPEC. ISS.), 15–26. https://doi.org/10.1016/j.ecolmodel.2005.01.023

Calcaterra, D., Ramondini, M., Calo, F., Longobardi, V., Parise, M., & Galzerano, C. (2008). DInSAR techniques for monitoring slow-moving landslides. In *Landslides and Engineered Slopes. From the Past to the Future* (pp. 1095–1101). CRC Press. https://doi.org/10.1201/9780203885284-c144

Colesanti, C. , Ferretti, A. , P., & C. & Rocca, F. (2003). Monitoring landslides and tectonic motions with the Permanent Scatterers Technique. *Engineering Geology*, 3–14. https://doi.org/https://doi.org/10.1016/S0013-7952(02)00195-3

Colesanti, C., & Wasowski, J. (2006). Investigating landslides with space-borne Synthetic Aperture Radar (SAR) interferometry. *Engineering Geology*, *88*(3–4), 173–199. https://doi.org/10.1016/j.enggeo.2006.09.013

Copernicus. (2023). https://doi.org/https://sentinels.copernicus.eu/web/sentinel/user-guides/sentinel-1-sar/revisit-and-coverage

Copernicus DEM - Global and European Digital Elevation Model *(COP-DEM)*. (2022). https://doi.org/https://doi.org/10.1029/2018EO104623

Costantini, M., Minati, F., Trillo, F., Ferretti, A., Novali, F., Passera, E., Dehls, J., Larsen, Y., Marinkovic, P., Eineder, M., Brcic, R., Siegmund, R., Kotzerke, P., Probeck, M., Kenyeres, A., Proietti, S., Solari, L., & Andersen, H. S. (2021). European Ground Motion Service (EGMS). *International Geoscience and Remote Sensing Symposium (IGARSS)*, *2021-July*, 3293–3296. https://doi.org/10.1109/IGARSS47720.2021.9553562

DARES. (2022). https://doi.org/https://www.linkedin.com/pulse/advanced-insar-techniques-early-detection-precursor-displacements-

Dick, G. J., Eberhardt, E., Cabrejo-Liévano, A. G., Stead, D., & Rose, N. D. (2015). Development of an early-warning time-of-failure analysis methodology for open-pit mine slopes utilizing ground-based slope stability radar monitoring data. *Canadian Geotechnical Journal*, *52*(4), 515–529. https://doi.org/10.1139/cgj-2014-0028

Dickmann, F. (2011). Reclamation conditions of opencast mining in the Rhenish lignite-mining region (Germany). *Zeitschrift Fur Geomorphologie*, *55*, 15–24. https://doi.org/10.1127/0372-8854/2011/0055S1-0034

Escayo, J., Marzan, I., Martí, D., Tornos, F., Farci, A., Schimmel, M., Carbonell, R., & Fernández, J. (2022). Radar Interferometry as a Monitoring Tool for an Active Mining Area Using Sentinel-1 C-Band Data, Case Study of Riotinto Mine. *Remote Sensing*, *14*(13). https://doi.org/10.3390/rs14133061

European Geological Data Infrastructure *(EGDI)*. (2023). https://doi.org/https://www.europe-geology.eu/

European Ground Motion Service - Copernicus Land Monitoring Service. (2023). *EGMS-CLMS*. https://doi.org/https://land.copernicus.eu/pan-european/european-ground-motion-service

European Space Agency. (2023). *ESA*. https://doi.org/https://sentinels.copernicus.eu/web/sentinel/user-guides/sentinel-1-sar/acquisition-modes/interferometric-wide-swath

Farolfi, G. , Soldato, M. , D. , Bianchini, S. , Casagli, N. , Farolfi, G. , Soldato, M. D. , Bianchini, S., & Casagli, N. (2019). *Exploitation of GNSS for calibrating space-*

borne SAR for the study of land subsidence. https://www.researchgate.net/publication/334479759

Ferretti, A. , Prati, C. , & & Rocca, F. (2000). Nonlinear subsidence rate estimation using permanent scatterers in differential SAR interferometry. *IEEE Transactions on Geoscience and Remote Sensing, 38*(5), 2202–2212. https://doi.org/10.1109/36.868878

Ferretti, A., Prati, C., & Rocca, F. (2001a). Permanent scatterers in SAR interferometry. *IEEE Transactions on Geoscience and Remote Sensing*, *39*(1), 8–20. https://doi.org/10.1109/36.898661

Ferretti, A., Prati, C., & Rocca, F. (2001b). Permanent scatterers in SAR interferometry. *IEEE Transactions on Geoscience and Remote Sensing*, *39*(1), 8–20. https://doi.org/10.1109/36.898661

Ferretti et al. (2011). A new algorithm for processing interferometric data-stacks SqueeSAR. *SqueeSAR. IEEE Transactions on Geoscience and Remote Sensing*, 3460–3470.https://doi.org/10.1109/TGRS.2011.2124465

Fruneau, B., & Sarti, F. (2000). Detection of ground subsidence in the city of Paris using radar interferometry: Isolation of deformation from atmospheric artifacts using correlation. *Geophysical Research Letters*, *27*(24), 3981–3984. https://doi.org/10.1029/2000GL008489

Gerwin, W., Raab, T., Birkhofer, K., Hinz, C., Letmathe, P., Leuchner, M., Roß-Nickoll, M., Rüde, T., Trachte, K., Wätzold, F., & Lehmkuhl, F. (2023). Perspectives of lignite post-mining landscapes under changing environmental conditions: what can we learn from a comparison between the Rhenish and Lusatian region in Germany? *Environmental Sciences Europe*, *35*(1). https://doi.org/10.1186/s12302-023-00738-z

Geudtner, D. , Torres, R. , Snoeij, P. , Davidson, M., & Rommen, B. (2014). Sentinel-1 System capabilities and applications. *IEEE Geoscience and Remote Sensing Symposium*. https://doi.org/10.1109/IGARSS.2014.6946711

Gheorghe, M., & Armaş, I. (2016). Comparison of Multi-Temporal Differential Interferometry Techniques Applied to the Measurement of Bucharest City Subsidence. *Procedia Environmental Sciences*, *32*, 221–229. https://doi.org/10.1016/j.proenv.2016.03.027

Gojković, Z., Kilibarda, M., Brajović, L., Marjanović, M., Milutinović, A., & Ganić, A. (2023). Ground Surface Subsidence Monitoring Using Sentinel-1 in the “Kostolac” Open Pit Coal Mine. *Remote Sensing*, *15*(10). https://doi.org/10.3390/rs15102519

Grebby, S., Sowter, A., Gluyas, J., Toll, D., Gee, D., Athab, A., & Girindran, R. (2021). Advanced analysis of satellite data reveals ground deformation precursors to the Brumadinho Tailings Dam collapse. *Communications Earth and Environment*, *2*(1). https://doi.org/10.1038/s43247-020-00079-2

Hanssen, R. F. (2001). *Radar Interferometry* (Vol. 2). Springer Netherlands. https://doi.org/10.1007/0-306-47633-9

Hartwig, M. E., de Lima, L. R., & Perissin, D. (2021). Iw sentinel-1 satellite scenes for the investigation of mine slope stability: Experiences from the Riacho dos machados gold mine (brazil). *Earth Sciences Research Journal*, *25*(1), 93–99. https://doi.org/10.15446/esrj.v25n1.86563

Herrera, G., Tomás, R., Vicente, F., Lopez-Sanchez, J. M., Mallorquí, J. J., & Mulas, J. (2010). Mapping ground movements in open pit mining areas using differential SAR interferometry. *International Journal of Rock Mechanics and Mining Sciences*, *47*(7), 1114–1125. https://doi.org/10.1016/j.ijrmms.2010.07.006

Hongdong, F., Kazhong, D., Chengyu, J., Chuanguang, Z., & Jiqun, X. (2011). Land subsidence monitoring by D-InSAR technique. *Mining Science and Technology*, *21*(6), 869–872. https://doi.org/10.1016/j.mstc.2011.05.030

Janga, B. , Asamani, G. P., S. Z. , & & Cristea, N. (2023). A Review of Practical AI for Remote Sensing in Earth Sciences. *Remote Sens*, 4112.

Kotulak, N. , Mleczko, M. , Crosetto, M. , Palamà, R., & Mróz, M. (2022). Interferometric SAR deformation monitoring using passive reflectors and ascending and descending passes. *International Archives of the Photogrammetry, Remote Sensing and Spatial Information Sciences - ISPRS Archives*, *43*(B3-2022), 285–292. https://doi.org/10.5194/isprs-archives-XLIII-B3-2022-285-2022

Lazecký, M., Bakon, M., & Hlavácová, I. (2015). Effect of DEM inaccuracy on precision of satellite inSAR results. *Lecture Notes in Geoinformation and Cartography*, *211*, 165–171. https://doi.org/10.1007/978-3-319-18407-4_14

Li, S., Xu, W., & Li, Z. (2022). Review of the SBAS InSAR Time-series algorithms, applications, and challenges. *Geodesy and Geodynamics*, *13*(2), 114–126. https://doi.org/10.1016/j.geog.2021.09.007

Massonnet, D., & Feigl, K. L. (1998). Radar interferometry and its application to changes in the earth's surface. *Reviews of Geophysics*, *36*(4), 441–500. https://doi.org/10.1029/97RG03139

Massonnet, D., Rossi, M., Carmona, C., Adragna, F., Peltzer, G., Feigl, K., & Rabaute, T. (1993). The displacement field of the Landers earthquake mapped by radar interferometry. *Nature*, *364*(6433), 138–142. https://doi.org/10.1038/364138a0

Mirmazloumi, S. M., Wassie, Y., Navarro, J. A., Palamà, R., Krishnakumar, V., Barra, A., Cuevas-González, M., Crosetto, M., & Monserrat, O. (2022). Classification of ground deformation using sentinel-1 persistent scatterer interferometry time series. *GIScience and Remote Sensing*, *59*(1), 374–392. https://doi.org/10.1080/15481603.2022.2030535

Monti-Guarnieri, A., Giudici, D., & Recchia, A. (2017). Identification of C-band radio frequency interferences from Sentinel-1 data. *Remote Sensing*, *9*(11). https://doi.org/10.3390/rs9111183

Mora, O. , Lanari, R. , Mallorquí, J. J. , Berardino, P., & Sansosti, E. (2002). A New Algorithm for Monitoring Localized Deformation Phenomena Based on Small Baseline Differential SAR Interferograms. *IEEE International Geoscience and Remote Sensing Symposium*. https://doi.org/10.1109/IGARSS.2002.1025900

Murdaca, G., Rucci, A., & Prati, C. (2022). Deep Learning for InSAR Phase Filtering: An Optimized Framework for Phase Unwrapping. *Remote Sensing*, *14*(19). https://doi.org/10.3390/rs14194956

Ng, A. H.-M., Ge, L., Du, Z., Wang, S., & Ma, C. (2017). Satellite radar interferometry for monitoring subsidence induced by longwall mining activity using Radarsat-2, Sentinel-1 and ALOS-2 data. *International Journal of Applied Earth Observation and Geoinformation*, *61*, 92–103. https://doi.org/10.1016/j.jag.2017.05.009

Pawluszek-Filipiak, K., & Borkowski, A. (2020). Integration of DInSAR and SBAS techniques to determine mining-related deformations using Sentinel-1 data: The case study of Rydultowy mine in Poland. *Remote Sensing*, *12*(2). https://doi.org/10.3390/rs12020242

Perissin, D., & Ferretti, A. (2007). Urban-target recognition by means of repeated spaceborne SAR images. *IEEE Transactions on Geoscience and Remote Sensing*, *45*(12), 4043–4058. https://doi.org/10.1109/TGRS.2007.906092

Rosen, P. A., Hensley, S., Joughin, I. R., Li, F. K., Madsen, S. N., Rodríguez, E., & Goldstein, R. M. (2000). *Synthetic Aperture Radar Interferometry*. https://doi.org/10.1109/5.838084

Roy, P., Martha, T. R., Khanna, K., Jain, N., & Kumar, K. V. (2022). Time and path prediction of landslides using InSAR and flow model. *Remote Sensing of Environment*, *271*. https://doi.org/10.1016/j.rse.2022.112899

Shirani, K., & Pasandi, M. (2019). Detecting and monitoring of landslides using persistent scattering synthetic aperture radar interferometry. *Environmental Earth Sciences*, *78*(1). https://doi.org/10.1007/s12665-018-8042-x

Sousa, J. J., Ruiz, A. M., Hanssen, R. F., Bastos, L., Gil, A. J., Galindo-Zaldívar, J., & Sanz de Galdeano, C. (2010). PS-InSAR processing methodologies in the

detection of field surface deformation-Study of the Granada basin (Central Betic Cordilleras, southern Spain). *Journal of Geodynamics*, *49*(3–4), 181–189. https://doi.org/10.1016/j.jog.2009.12.002

Tang, W., Motagh, M., & Zhan, W. (2020). Monitoring active open-pit mine stability in the Rhenish coalfields of Germany using a coherence-based SBAS method. *International Journal of Applied Earth Observation and Geoinformation*, *93*. https://doi.org/10.1016/j.jag.2020.102217

Tong, X., & Schmidt, D. (2016). Active movement of the Cascade landslide complex in Washington from a coherence-based InSAR time series method. *Remote Sensing of Environment*, *186*, 405–415. https://doi.org/10.1016/j.rse.2016.09.008

Tzampoglou, P., & Loupasakis, C. (2023). Hydrogeological Hazards in Open Pit Coal Mines–Investigating Triggering Mechanisms by Validating the European Ground Motion Service Product with Ground Truth Data. *Water (Switzerland)*, *15*(8). https://doi.org/10.3390/w15081474

Wang, K., Xu, X., & Fialko, Y. (2017). Improving Burst Alignment in TOPS Interferometry with Bivariate Enhanced Spectral Diversity. *IEEE Geoscience and Remote Sensing Letters*, *14*(12), 2423–2427. https://doi.org/10.1109/LGRS.2017.2767575

Wassie, Y., Mirmazloumi, S. M., Crosetto, M., Palamà, R., Monserrat, O., & Crippa, B. (2022). Spatio-Temporal Quality Indicators for Differential Interferometric Synthetic Aperture Radar Data. *Remote Sensing*, *14*(3). https://doi.org/10.3390/rs14030798

Xue, F., Lv, X., Dou, F., & Yun, Y. (2020). A Review of Time-Series Interferometric SAR Techniques: A Tutorial for Surface Deformation Analysis. In *IEEE Geoscience and Remote Sensing Magazine* (Vol. 8, Issue 1, pp. 22–42). Institute of Electrical and Electronics Engineers Inc. https://doi.org/10.1109/MGRS.2019.2956165

Yague-Martinez, N., Prats-Iraola, P., Gonzalez, F. R., Brcic, R., Shau, R., Geudtner, D., Eineder, M., & Bamler, R. (2016). Interferometric Processing of Sentinel-1 TOPS Data. *IEEE Transactions on Geoscience and Remote Sensing*, *54*(4), 2220–2234. https://doi.org/10.1109/TGRS.2015.2497902

Yu, C., Li, Z., Penna, N. T., & Crippa, P. (2018). Generic Atmospheric Correction Model for Interferometric Synthetic Aperture Radar Observations. *Journal of Geophysical Research: Solid Earth*, *123*(10), 9202–9222. https://doi.org/10.1029/2017JB015305

Zhang, L. , & Lu, Z. (2022). Advances in InSAR Imaging and Data Processing—A Review. *Remote Sensing*, *14*(17). https://doi.org/10.3390/rs14174307

Zhang, W., You, H., Wang, C., Zhang, H., & Tang, Y. (2023). Parallel Optimization for Large Scale Interferometric Synthetic Aperture Radar Data Processing. *Remote Sensing*, *15*(7). https://doi.org/10.3390/rs15071850

Zhang, Z., Hu, C., Wu, Z., Zhang, Z., Yang, S., & Yang, W. (2023). Monitoring and analysis of ground subsidence in Shanghai based on PS-InSAR and SBAS-InSAR technologies. *Scientific Reports*, *13*(1). https://doi.org/10.1038/s41598-023-35152-1

7. Appendix

7.1. Appendix I: PS- DinSAR multi-stack process.

Table 1. List of the processed images from 2021 DESC

sentinel1_139_20210105_054148414_IW_D_VV_slc_list	sentinel1_139_20210628_054217105_IW_D_VV_slc_list
sentinel1_139_20210111_054213496_IW_D_VV_slc_list	sentinel1_139_20210710_054217758_IW_D_VV_slc_list
sentinel1_139_20210117_054147950_IW_D_VV_slc_list	sentinel1_139_20210716_054152799_IW_D_VV_slc_list
sentinel1_139_20210123_054212987_IW_D_VV_slc_list	sentinel1_139_20210728_054153619_IW_D_VV_slc_list
sentinel1_139_20210129_054147574_IW_D_VV_slc_list	sentinel1_139_20210803_054219262_IW_D_VV_slc_list
sentinel1_139_20210204_054212613_IW_D_VV_slc_list	sentinel1_139_20210809_054154207_IW_D_VV_slc_list
sentinel1_139_20210210_054147211_IW_D_VV_slc_list	sentinel1_139_20210815_054219817_IW_D_VV_slc_list
sentinel1_139_20210216_054212239_IW_D_VV_slc_list	sentinel1_139_20210821_054154834_IW_D_VV_slc_list
sentinel1_139_20210222_054146933_IW_D_VV_slc_list	sentinel1_139_20210827_054220477_IW_D_VV_slc_list
sentinel1_139_20210228_054212142_IW_D_VV_slc_list	sentinel1_139_20210902_054155356_IW_D_VV_slc_list
sentinel1_139_20210306_054146797_IW_D_VV_slc_list	sentinel1_139_20210908_054221069_IW_D_VV_slc_list
sentinel1_139_20210312_054212200_IW_D_VV_slc_list	sentinel1_139_20210914_054155910_IW_D_VV_slc_list
sentinel1_139_20210318_054146756_IW_D_VV_slc_list	sentinel1_139_20210920_054221474_IW_D_VV_slc_list
sentinel1_139_20210324_054212411_IW_D_VV_slc_list	sentinel1_139_20210926_054156330_IW_D_VV_slc_list
sentinel1_139_20210330_054147094_IW_D_VV_slc_list	sentinel1_139_20211002_054221816_IW_D_VV_slc_list
sentinel1_139_20210405_054212695_IW_D_VV_slc_list	sentinel1_139_20211008_054156444_IW_D_VV_slc_list
sentinel1_139_20210411_054147558_IW_D_VV_slc_list	sentinel1_139_20211014_054221855_IW_D_VV_slc_list
sentinel1_139_20210417_054213186_IW_D_VV_slc_list	sentinel1_139_20211020_054156755_IW_D_VV_slc_list
sentinel1_139_20210423_054148178_IW_D_VV_slc_list	sentinel1_139_20211026_054221922_IW_D_VV_slc_list
sentinel1_139_20210429_054213480_IW_D_VV_slc_list	sentinel1_139_20211101_054156548_IW_D_VV_slc_list
sentinel1_139_20210505_054148551_IW_D_VV_slc_list	sentinel1_139_20211107_054221647_IW_D_VV_slc_list
sentinel1_139_20210511_054214285_IW_D_VV_slc_list	sentinel1_139_20211113_054156312_IW_D_VV_slc_list
sentinel1_139_20210517_054149307_IW_D_VV_slc_list	sentinel1_139_20211119_054221539_IW_D_VV_slc_list
sentinel1_139_20210523_054214862_IW_D_VV_slc_list	sentinel1_139_20211125_054155918_IW_D_VV_slc_list
sentinel1_139_20210529_054149922_IW_D_VV_slc_list	sentinel1_139_20211201_054220948_IW_D_VV_slc_list
sentinel1_139_20210604_054215554_IW_D_VV_slc_list	sentinel1_139_20211207_054155419_IW_D_VV_slc_list
sentinel1_139_20210610_054150723_IW_D_VV_slc_list	sentinel1_139_20211213_054220529_IW_D_VV_slc_list
sentinel1_139_20210616_054216478_IW_D_VV_slc_list	sentinel1_139_20211219_054154887_IW_D_VV_slc_list
sentinel1_139_20210622_054151423_IW_D_VV_slc_list	**Master:** sentinel1_139_20210722_054218476_IW_D_VV_slc_list

Table 2. List of the processed imagery from 2022 DESC

sentinel1_139_20220106_054219209_IW_D_VV_slc_list	sentinel1_139_20220705_054223597_IW_D_VV_slc_list
sentinel1_139_20220118_054218705_IW_D_VV_slc_list	sentinel1_139_20220717_054224401_IW_D_VV_slc_list
sentinel1_139_20220130_054218235_IW_D_VV_slc_list	sentinel1_139_20220729_054225055_IW_D_VV_slc_list
sentinel1_139_20220211_054218064_IW_D_VV_slc_list	sentinel1_139_20220810_054225861_IW_D_VV_slc_list
sentinel1_139_20220223_054217959_IW_D_VV_slc_list	sentinel1_139_20220822_054226482_IW_D_VV_slc_list
sentinel1_139_20220307_054217754_IW_D_VV_slc_list	sentinel1_139_20220903_054227305_IW_D_VV_slc_list
sentinel1_139_20220319_054217889_IW_D_VV_slc_list	sentinel1_139_20220915_054227530_IW_D_VV_slc_list
sentinel1_139_20220331_054218032_IW_D_VV_slc_list	sentinel1_139_20220927_054227620_IW_D_VV_slc_list
sentinel1_139_20220412_054218352_IW_D_VV_slc_list	sentinel1_139_20221009_054227871_IW_D_VV_slc_list
sentinel1_139_20220424_054219174_IW_D_VV_slc_list	sentinel1_139_20221021_054227707_IW_D_VV_slc_list
sentinel1_139_20220506_054219300_IW_D_VV_slc_list	sentinel1_139_20221102_054227483_IW_D_VV_slc_list
sentinel1_139_20220518_054220094_IW_D_VV_slc_list	sentinel1_139_20221114_054227377_IW_D_VV_slc_list
sentinel1_139_20220530_054221323_IW_D_VV_slc_list	sentinel1_139_20221126_054227481_IW_D_VV_slc_list
sentinel1_139_20220611_054222275_IW_D_VV_slc_list	sentinel1_139_20221208_054226758_IW_D_VV_slc_list

sentinel1_139_20220623_054222969_IW_D_VV_slc_list	sentinel1_139_20221220_054225914_IW_D_VV_slc_list

Table 3. Processing time PS DinSAR multi-stack process
Process 2021

Stage of the process	Time (min)
Import imagery	75 min.
Connection Graph	60 min.
Interferometric Process	260 min.
First Step	377 min.
Second Step	150 min.
Geocoding	15 min.

Table 4. Monitoring 2022

Monitoring	Import images	Interferometric Process	First Step	Second Step	Geocoding	TOTAL min
M1	10	25	195	90	36	356
M2	10	35	205	90	16	356
M3	10	35	215	90	16	366
M4	10	30	240	90	16	386
M5	10	26	240	102	19	397
M6	30	24	270	120	21	465

Table 5. Interferometric Process

Principal Parameters	
Generate Dint Multilooked for Quick View	False
Rebuild All	False
Atmosphere External Sensors	GACOS
Coregistration with DEM	True
Other Parameters	
Range looks	4
Azimuth looks	1

Table 6. First Step

Principal Parameters	
Displacement Sampling (mm/year)	1
Min Displacement Velocity (mm/year)	-100
Max Displacement Velocity (mm/year)	100
Residual Height Sampling	2
Min Residual Height (m)	-70
Max Residual Height (m)	70

SubArea for Single Reference Point (sqkm)	25
SubArea Overlap (%)	30
Number of Candidates	300
Rebuild All	False
Other Parameters	
Coherence Threshold SubArea Merging	0.66
MuSigma Threshold for Ref Points (%)	60
MuSigma Mask	0

Table 7. Second step

Principal Parameters	
Atmosphere High Pass Size (days)	365
Atmosphere Low Pass Size (m)	1200
Rebuild All	False
Other Parameters	
Min Displacement Velocity (mm/year)	-100
Max Displacement Velocity (mm/year)	100
Residual Height Sampling	2
Min Residual Height (m)	-70
Max Residual Height (m)	70

Table 8. Geocoding

Principal Parameters	
Product Temporal Coherence Threshold	0.75
Generate KML	True
Make Geocoded Raster	True
Vertical Displacement	True
Other Parameters	
Geocode using MuSigma Threshold	True
MuSigma Threshold	3,2

All parameters applied in the 2021 process were reused for the 2022 monitoring, with the addition of utilizing the 'Edit Connection Graph' tool to incorporate the new images.

7.2. Appendix II: Calibration

PS points of 2021 dataset

([D_20210111] - [D_20210105]) + ([D_20210117] - [D_20210111]) + ([D_20210123] - [D_20210117]) + ([D_20210129] - [D_20210123]) + ([D_20210204] - [D_20210129]) + ([D_20210210] - [D_20210204]) + ([D_20210216] - [D_20210210]) + ([D_20210222] - [D_20210216]) + ([D_20210228] - [D_20210222]) + ([D_20210306] - [D_20210228]) + ([D_20210312] - [D_20210306]) + ([D_20210318] - [D_20210312]) + ([D_20210324] - [D_20210318]) + ([D_20210330] - [D_20210324]) + ([D_20210405] - [D_20210330]) + ([D_20210411] - [D_20210405]) + ([D_20210417] - [D_20210411]) + ([D_20210423] - [D_20210417]) + ([D_20210429] - [D_20210423]) + ([D_20210505] - [D_20210429]) + ([D_20210511] - [D_20210505]) + ([D_20210517] - [D_20210511]) + ([D_20210523] - [D_20210517]) + ([D_20210529] - [D_20210523]) + ([D_20210604] - [D_20210529]) + ([D_20210610] - [D_20210604]) + ([D_20210616] - [D_20210610]) + ([D_20210622] - [D_20210616]) + ([D_20210628] - [D_20210622]) + ([D_20210710] - [D_20210628]) + ([D_20210716] - [D_20210710]) + ([D_20210722] - [D_20210716]) + ([D_20210728] - [D_20210722]) + ([D_20210803] - [D_20210728]) + ([D_20210809] - [D_20210803]) + ([D_20210815] - [D_20210809]) + ([D_20210821] - [D_20210815]) + ([D_20210827] - [D_20210821]) + ([D_20210902] - [D_20210827]) + ([D_20210908] - [D_20210902]) + ([D_20210914] - [D_20210908]) + ([D_20210920] - [D_20210914]) + ([D_20210926] - [D_20210920]) + ([D_20211002] - [D_20210926]) + ([D_20211008] - [D_20211002]) + ([D_20211014] - [D_20211008]) + ([D_20211020] - [D_20211014]) + ([D_20211026] - [D_20211020]) + ([D_20211101] - [D_20211026]) + ([D_20211107] - [D_20211101]) + ([D_20211113] - [D_20211107]) + ([D_20211119] - [D_20211113]) + ([D_20211125] - [D_20211119]) + ([D_20211201] - [D_20211125]) + ([D_20211207] - [D_20211201]) + ([D_20211213] - [D_20211207]) + ([D_20211219] - [D_20211213])

This function is equal to [D_20211219]. This is the last field in the table of attributes of the PS 2021 dataset and it corresponds to December 19, 2021.
In order to calibrate the PS points for the dataset, first a linear regression has to be calculated between the GNSS stations and once the slope (m) and intercept (b) are obtained they are applied to the formula :

PS *calibrated velocity* = ([PS*vel*] * m) -b

Table1. Y represents the GNSS value in mm/year and X is the closest PS to the GNSS station, represented by the velocity in mm/year.

	Y GNSS mm/year	X PS(velocity/mm)
KERK	-4,971	3,3330
SEL2	-7,6790	-9,3220
TIT2	-6,2030	2,8770

Calibration PS points of 2021 year.

PS *calibrated* = ([PS*vel*] * 0.1709) -6.1071

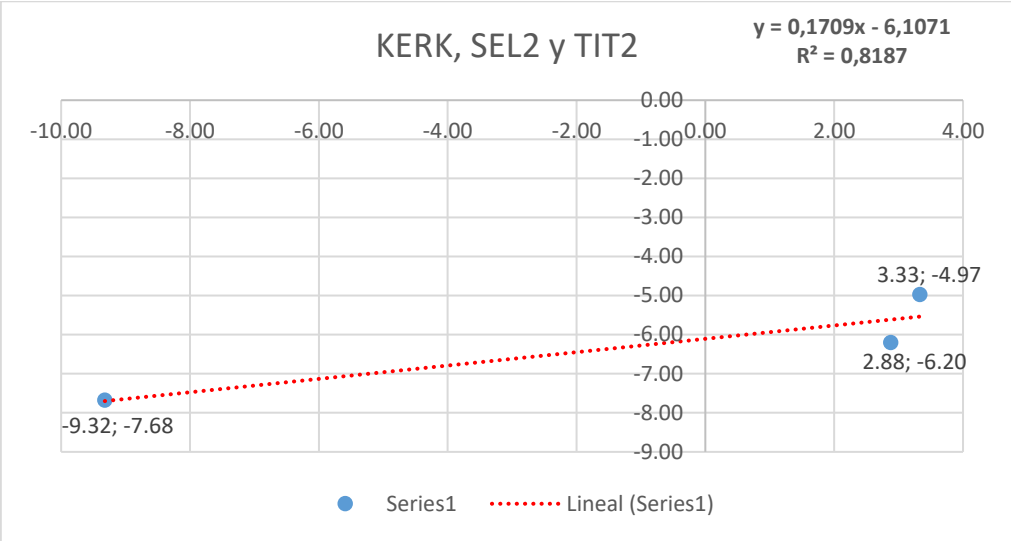

Fig.1.GNSS SEL2, KERK and TIT2

PS *calibrated* = ([PS*vel*] * 0.121) -6.5511

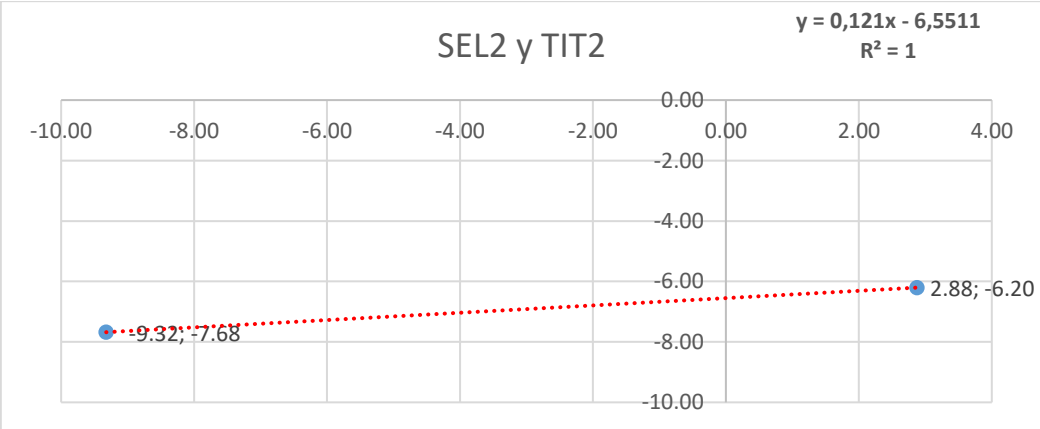

Fig.3 GNSS SEL2 and TIT2

PS *calibrated* = ([PS*vel*] * 0.214) -5.684

Fig. 3 GNSS KAL2, SEL2 and KERK

PS *calibrated* = ([PS*vel*] * 2.7018) -13.976

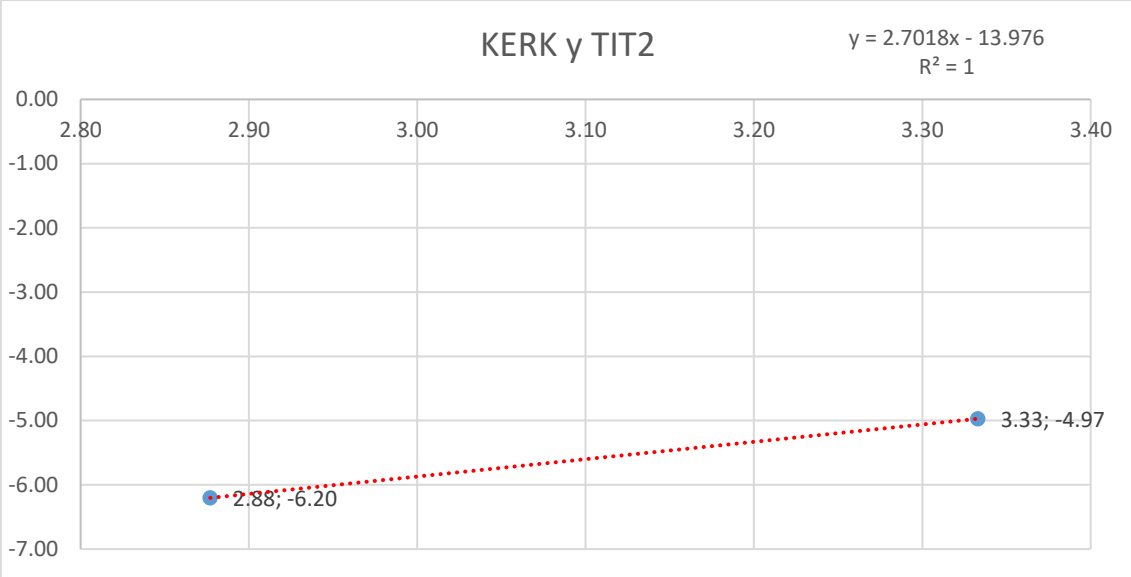

Fig. 4 GNSS KERK and TIT2

GNSS KAL1 and SEL2 (FIG.22 E)

-9,322 – (-7,679) = 1,642

In this case, no figure is presented as it is a singular GNSS and it was calculated using Table 1 and then the formula is applied.

PS *calibrated* = [PS*vel*] + 1.642

PS *calibrated* = ([PS*vel* velocity] * 0.439) -6.5635

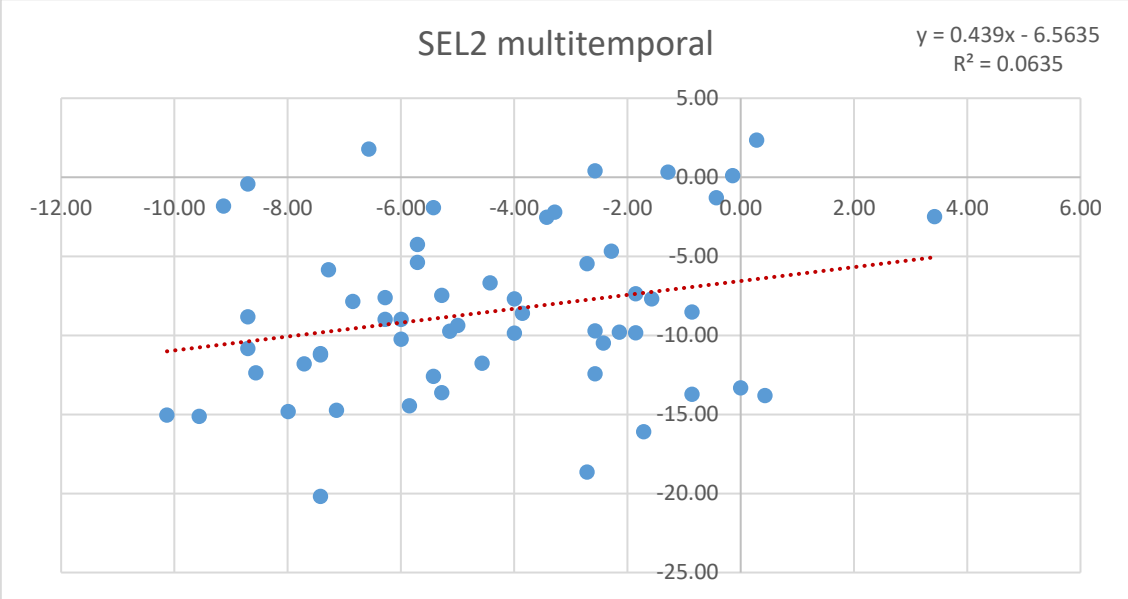

Fig.5 GNSS Multitemporal **(FIG. 22 F)**

7.3. Appendix III: Python Scripts

TI script written in Jupyter Notebook

In [1]:
```
import geopandas as gpd
import pandas as pd
import numpy as np
```

In [2]:
```
import geopandas as gpd

# Replace 'path_to_shapefile' with the actual path
shapefile_path = 'C:/Users/34617/Documents/MASTER/asignaturas/PRACTICA TRACASA +TFM/INDICES/SHAPE_FINAL_2021_2022/PS_75_VD_M6

# Read the shapefile using geopandas
data = gpd.read_file(shapefile_path)
```

In [5]:
```
# Get the number of rows and columns in the csv
rows = len(data.axes[0])
cols = len(data.axes[1])
# Print the number of rows and columns in the csv
print("Number of Rows: " + str(rows))
print("Number of Columns: " + str(cols))
```

```
Number of Rows: 239131
Number of Columns: 105
```

In [6]:
```
# Delete columns
columns_to_delete = ['velocity','coherence','MuSigma','Hprecision','Vprecision','range','azimuth', 'SubArea_ID', 'ALOS', 'ILO
data.drop(columns=columns_to_delete, inplace=True)
```

In [7]:
```
data.insert(0, 'FID', range(1, len(data) + 1))
# Set 'FID1' column as the index


#data=data.set_index('FID', inplace=True)
```

In [8]:
```
#set FID column as index for the dataframe
data['FID'] = pd.RangeIndex(len(data))
```

In [12]:
```
data.set_index('FID', inplace=True)  #prevents deleting vaues from the first and the last rows.!!!!
```

In [13]:
```
# Get all the column indices as a list
column_indices = data.columns.tolist()

# Print the column indices
print(column_indices)
```

```
['lon', 'lat', 'xpos', 'ypos', 'zpos', 'Z', 'D_20211201', 'D_20211207', 'D_20211213', 'D_20220106', 'D_20220118', 'D_20220130', 'D_20220211', 'D_20220223', 'D_20220307', 'D_20220319', 'D_20220331', 'D_20220412', 'D_20220424', 'D_20220506', 'D_20220518', 'D_20220530', 'D_20220611', 'D_20220623', 'D_20220705', 'D_20220717', 'D_20220729', 'D_20220810', 'D_20220822', 'D_20220903', 'D_20220915', 'D_20220927', 'D_20221009', 'D_20221021', 'D_20221102', 'D_20221114', 'D_20221126', 'D_20221208', 'D_20221220', 'geometry']
```

In [20]:
```
all_ranges = [(6, 9),(8,14),(13,19),(18,24),(23,29),(28,34),(33,39)]

# Create empty dictionaries to store the calculated values for each range
linear_regression_data = {}
custom_names = {
    (6,9): { 'slope': 'Slope_Dec21', 'R2': 'R2_Dec21'},
    (8,14): { 'slope': 'Slope_M1', 'R2': 'R2_M1'},
    (13,19): { 'slope': 'Slope_M2', 'R2': 'R2_M2'},
    (18,24): { 'slope': 'Slope_M3', 'R2': 'R2_M3'},
    (23,29): { 'slope': 'Slope_M4', 'R2': 'R2_M4'},
    (28,34): { 'slope': 'Slope_M5', 'R2': 'R2_M5'},
    (33,39): { 'slope': 'Slope_M6', 'R2': 'R2_M6'}
}

# Calculate the slope, R2, and abs angle for each range and each row
for start, end in all_ranges:
    columns_for_regression = data.iloc[:, start:end]
    slopes = []
    r2_values = []

    for _, row in columns_for_regression.iterrows():
        x = np.arange(len(row))
        coeffs = np.polyfit(x, row, 1)
        slope, intercept = coeffs
        # Calculate R2
        predicted_y = slope * x + intercept
        r2 = 1 - np.sum((row - predicted_y) ** 2) / np.sum((row - np.mean(row)) ** 2)
        r2 = 0 if np.isnan(r2) or np.isinf(r2) else r2
        # Round R2 to 4 decimals
        r2 = round(r2, 4)
        # Calculate the absolute angle
        abs_angle = np.abs(np.degrees(np.arctan(slope)))
        slopes.append(slope)
        r2_values.append(r2)

    # Store the calculated values in the dictionaries
    column_labels = custom_names[(start, end)]
    linear_regression_data[column_labels['slope']] = slopes
    linear_regression_data[column_labels['R2']] = r2_values

# Convert the dictionary to a DataFrame
linear_regression_df = pd.DataFrame(linear_regression_data)

# Reset index of the linear_regression_df DataFrame
#linear_regression_df.reset_index(drop=True, inplace=True)

# Concatenate the new DataFrame with the original DataFrame 'data'
data = pd.concat([data, linear_regression_df], axis=1)

# Create new columns and store 1 or 0 based on R2 condition
for start, end in custom_names.keys():
    r2_column_name = custom_names[(start, end)]['R2']
    new_column_name = f'Cond_{r2_column_name}'
    data[new_column_name] = data[r2_column_name].apply(lambda x: 1 if x > 0.8 else 0)
```

In [36]:
```
# Step 1: Perform the subtractions and create the new columns

data['SD_De21_M1'] = data['Slope_Dec21'] - data['Slope_M1']
data['SD_M1_M2'] = data['Slope_M1'] - data['Slope_M2']
data['SD_M2_M3'] = data['Slope_M2'] - data['Slope_M3']
data['SD_M3_M4'] = data['Slope_M3'] - data['Slope_M4']
data['SD_M4_M5'] = data['Slope_M4'] - data['Slope_M5']
data['SD_M5_M6'] = data['Slope_M5'] - data['Slope_M6']

# Step 2: Convert the new columns directly to degrees
data['SD_De21_M1_Degrees'] = np.degrees(data['SD_De21_M1'])
data['SD_M1_M2_Degrees'] = np.degrees(data['SD_M1_M2'])
data['SD_M2_M3_Degrees'] = np.degrees(data['SD_M2_M3'])
data['SD_M3_M4_Degrees'] = np.degrees(data['SD_M3_M4'])
data['SD_M4_M5_Degrees'] = np.degrees(data['SD_M4_M5'])
data['SD_M5_M6_Degrees'] = np.degrees(data['SD_M5_M6'])
```

In [38]:
```
# Step 3: Create conditions for the new columns in degrees
data['SD_De21_M1_Condition'] = data['SD_De21_M1_Degrees'].apply(lambda x: 1 if abs(x) > 15 else 0)
data['SD_M1_M2_Condition'] = data['SD_M1_M2_Degrees'].apply(lambda x: 1 if abs(x) > 15 else 0)
data['SD_M2_M3_Condition'] = data['SD_M2_M3_Degrees'].apply(lambda x: 1 if abs(x) > 15 else 0)
data['SD_M3_M4_Condition'] = data['SD_M3_M4_Degrees'].apply(lambda x: 1 if abs(x) > 15 else 0)
data['SD_M4_M5_Condition'] = data['SD_M4_M5_Degrees'].apply(lambda x: 1 if abs(x) > 15 else 0)
data['SD_M5_M6_Condition'] = data['SD_M5_M6_Degrees'].apply(lambda x: 1 if abs(x) > 15 else 0)
```

In [40]:
```
# Create a new column to represent the cases where both conditions are met

data['ProbCondM1'] = np.where(
    (data['Cond_R2_M1'] == 1) & (data['SD_De21_M1_Condition'] == 1),
    2,  # Value if both conditions are met
    0   # Value if conditions are not met
)

data['ProbCondM2'] = np.where(
    (data['Cond_R2_M2'] == 1) & (data['SD_M1_M2_Condition'] == 1),
    2,  # Value if both conditions are met
    0   # Value if conditions are not met
)

data['ProbCondM3'] = np.where(
    (data['Cond_R2_M3'] == 1) & (data['SD_M2_M3_Condition'] == 1),
    2,  # Value if both conditions are met
    0   # Value if conditions are not met
)

data['ProbCondM4'] = np.where(
    (data['Cond_R2_M4'] == 1) & (data['SD_M3_M4_Condition'] == 1),
    2,  # Value if both conditions are met
    0   # Value if conditions are not met
)

data['ProbCondM5'] = np.where(
    (data['Cond_R2_M5'] == 1) & (data['SD_M4_M5_Condition'] == 1),
    2,  # Value if both conditions are met
    0   # Value if conditions are not met
)

data['ProbCondM6'] = np.where(
    (data['Cond_R2_M6'] == 1) & (data['SD_M5_M6_Condition'] == 1),
    2,  # Value if both conditions are met
    0   # Value if conditions are not met
)
```

In [41]:
```
# List of columns to sum
columns_to_sum = ['ProbCondM1', 'ProbCondM2', 'ProbCondM3', 'ProbCondM4', 'ProbCondM5', 'ProbCondM6']

# Create a new column that sums the specified columns and divides the result by 2 (as integer)
data['Condition SUM problems'] = (data[columns_to_sum].sum(axis=1) // 2).astype(int)
```

In [1]:
```
#Saving the output supershape

output_path = "C:/Users/34617/Documents/MASTER/asignaturas/PRACTICA TRACASA +TFM/INDICES/SHAPE_FINAL_2021_2022/PS_75_VD_M6_20

# Save the modified GeoDataFrame as a new shapefile
data.to_file(output_path)
print("Modified shapefile saved successfully.")
```

AI was written in Jupyter Notebook

In [4]:
```
import numpy as np
import pandas as pd
```

In [5]:
```
# Load data from CSV into a DataFrame
df = pd.read_csv('Index_AI.csv', sep=';')
#df.set_index('FID', inplace=True)
```

In [6]:
```
df.head(3)
```

In [7]:
```
import numpy as np

ranges = [(10, 15), (15, 20), (20, 25), (25, 30), (30, 35), (35, 40)]
subsets = [df.iloc[:, range[0]:range[1]] for range in ranges]

for i, subset in enumerate(subsets, 1):
    r2_scores = []

    for row in range(subset.shape[0]):
        x = np.arange(ranges[i - 1][0], ranges[i - 1][1])
        y = subset.iloc[row, :].values

        coeffs = np.polyfit(x, y, deg=2)
        p = np.poly1d(coeffs)

        y_pred = p(x)
        ss_res = np.sum((y - y_pred) ** 2)
        ss_tot = np.sum((y - np.mean(y)) ** 2)
        r2 = 1 - (ss_res / ss_tot)
        r2_scores.append(r2)

    column_name = f"R2_M{i}"
    df[column_name] = r2_scores

    # Apply conditions on R2 values and create new columns
    column_name_cond = f"R2_Cond_M{i}"
    df[column_name_cond] = np.where(df[column_name] > 0.8, 1, 0)

    # Calculate acceleration coefficient for each range and row
    if i < len(ranges) - 1:
        acceleration_coeffs = np.abs(subset.iloc[:, -1].values - subsets[i + 1].iloc[:, 0].values) / 17
    elif i == len(ranges) - 1:
        acceleration_coeffs = np.abs(subset.iloc[:, -1].values - subsets[i].iloc[:, 0].values) / 18

    column_name_accel = f"Accel_M{i}"
    df[column_name_accel] = acceleration_coeffs

    # Apply conditions on acceleration coefficients and create new columns
    column_name_accel_cond = f"Accel_Cond_M{i}"
    df[column_name_accel_cond] = np.where(df[column_name_accel] >= 2, 1, 0)

# Create "Prob" column for each condition at the end of all columns
for i in range(1, len(ranges) + 1):
    column_name_cond = f"R2_Cond_M{i}"
    column_name_accel_cond = f"Accel_Cond_M{i}"
    df[f"Prob{i}"] = np.where((df[column_name_cond] == 1) & (df[column_name_accel_cond] == 1), 2, 0)

# List of columns to sum
columns_to_sum = [f"Prob{i}" for i in range(1, len(ranges) + 1)]

# Create a new column that sums the specified columns and divides the result by 2 (as integer)
df['Cond_SUM_Prob'] = (df[columns_to_sum].sum(axis=1) // 2).astype(int)
```

In [9]:
```
# Save the modified DataFrame to a new CSV file
new_csv_filename = "AI_BUENO.csv"
df.to_csv(new_csv_filename, sep=';')
print(f"Modified data saved to '{new_csv_filename}'")
```

```
Modified data saved to 'AI_BUENO.csv'
```

In [12]:
```
#CONVERT THE CSV FILE INTO SHP.
import pandas as pd
import geopandas as gpd
from shapely.geometry import Point

# Read the CSV file
df = pd.read_csv('AI_BUENO.csv', sep=';')

# Create a geometry column using the coordinates from the CSV
geometry = [Point(xy) for xy in zip(df['lon'], df['lat'])]

# Create a GeoDataFrame from the DataFrame and the geometry column
gdf = gpd.GeoDataFrame(df, geometry=geometry, crs='EPSG:4326')

# Save the GeoDataFrame as a Shapefile
gdf.to_file('AI_BUENO.shp', driver='ESRI Shapefile')
```